A COMPUTATIONAL FLUID DYNAMIC ANALYSIS OF THE AIRFLOW OVER THE KEYSTONE PLANT SPECIES, *AZORELLA SELAGO*, ON SUBANTARCTIC MARION ISLAND

Madeleine Lelon Combrinck

Thesis presented in partial fulfillment of the requirements for the degree of MScEng in Mechanical Engineering
Stellenbosch University

Thesis supervisor:
Professor T.M. Harms
Department of Mechanical and Mechatronic Engineering

Project initiator:
Professor M.A. McGeoch
Department of Conservation Ecology and Entomology

December 2008

Declaration

I, the undersigned, hereby declare that the work contained in this thesis is my own, original work and that I have not previously, in its entirety or in part, submitted it at any university for a degree.

Madeleine L. Combrinck *25 February 2009*

E.Phiri and M.L.Combrinck after a long day in the field on Marion Island

(Phiri,2008)

Abstract

Research conducted on Marion Island aims at predicting the consequence of climate change in the Subantarctic region, as well as for other terrestrial ecosystems. The island has the ideal ecosystem, due to its size, isolation and relative simplicity, to be studied as a prediction model for the consequence of climate change and the interaction between various climate related parameters.

The cushion plant, *Azorella selago*, is the focal point of this project due to the important functional roles it fulfils as well as its wide spread distribution over the island. *A. selago* grows in three different shapes; hemispherical, elliptical and crescent. The changes in airflow due to varying plant size are investigated as well as the exertion of force on the plant. The grass species *Agrostis magellanica* has the tendency to grow on top of *A. selago*. In addition it has been observed that the grass species grows more vibrantly on the leeward side of the cushion plant. In the light of this observation the particle deposition of grass seeds on *A. selago* is also investigated.

Computational fluid dynamic analyses are conducted for various sizes of each shape of the plant. These studies are augmented by wind tunnel and in situ measurements and observation and experimental determining of particle drag coefficients. Time independent, incompressible, turbulent flow is modelled by means of a high Reynolds number turbulence model with a modified Law-of-the-Wall to accommodate for the significant surface roughness.

Nine different dimensions over the various shapes were identified. Each shape is analysed and the patterns that emerged discussed. The windward pattern for all shapes display similar qualities. On the leeward side the shapes display distinctly different airflow patterns. The hemisphere shows two trailing lines typically associated with the horseshoe vortex phenomenon. The ellipse displays one distinctive trailing line. The most interesting flow patterns are found when analysing the crescent shape. Three trailing lines are observed, the side lines quickly dissipates with increasing height while the middle line remains distinctive. The complex recirculation patterns that emerge are further visualized by means of air particle tracks. The furthermost number of light particle deposition of *A. magellanica* seeds on *A. selago* are found at the windward location while physical evidence clearly indicates growth primarily on the leeward position. The leeward location on *A. selago* is protected from the harsh environmental conditions; wind speeds are minimal in this area. It will therefore be a more suitable site for the fostering of a vulnerable seedling that on the exposed windward side. A force analysis done on the plants reveals that the total force is two orders of magnitude higher that the shear force. Furthermore, the magnitude of the total force is directly proportional to the size of the plant. Three critical areas on the plant are common irrespective of shape or size: the stagnation point at the windward side, the apex region at the top and the leeward side of the plant.

Opsomming

Die doel van navorsings aktiwiteite op Marion Eiland is om die impak en gevolge van klimaatsverandering in die sub-Antarktiese gebied te voorspel asook vir ander ekostelsels in die algemeen. Die eiland het ‘n geskikte ekosisteem, vanweë die grootte, ligging en eenvoud, om bestudeer te word as ‘n model vir die gevolge van klimaatsverandering. Die interaksie tussen verskeie klimaat verwante parameters sal beter verstaan word in so ‘n klimaatstudie.

Die kussing plant, *A. selago*, is die fokus van die projek. Die plant vervul belangrike funksionele rolle en is wyd versprei oor die eiland. *A. selago* kom voor in drie verskillend geometriese vorms: half sferies, ellipties en ‘n boontjie vorm. Die veranderings in lugvloei te danke aan wisselende plant grootte is ondersoek asook die aanwending van krag op die plant. Die gras spesie, *Agrostis magellanica* toon die neiging om aan die wind stil kant van *A. selago* te groei. Hierdie tendens kan verklaar word aan die hand van ‘n partikel deponerings analise.

Berekenings vloeimeganika (BVM) analises is uitgevoer op verskillend groottes van elke vorm. Hierdie studies is versterk deur windtonnel toetse meetings en observasies en die eksperimentele bepaling van die partikel sleur koëffisiënt. Tyd onafhanklike, onsamedrukbare, turbulente vloei is gemodelleer deur die toepassing van die hoë Reynolds nommer turbulensie model met ‘n gemodifiseerde wet-van-die-wal om oppervlak grofheid in berekening te bring.

Nege verskillende plant geometrieë is geïdentifiseer en geanaliseer, die onderliggende patrone word in detail bespreek. Gemeenskaplike patrone in die vloeivelde loefwaarts van die relevante geometrieë is waargeneem terwyl benedewindse vloei patrone opmerklike verskille toon. Die sferiese geometrie huis ‘n werwel struktuur genaamd die hoefvormige vorteks wat gekenmerk word deur die dubbel sleep lyn. Anders as die sfere, toon die ellips slegs een sleep lyn en die boontjie geometrie drie sleep lyne. Komplekse hersirkulasie patrone is waargeneem. Visualisering deur middel van lug partikel paaie het hierdie waarneming vergemaklik. ‘n Hoë konsentrasie van gedeponeerde A. magellanica sade word op die loefsy van die plant aangetref. Fisiese bewyse toon dat die gras spesie hoofsaaklik benedewinds op die plant aangetref word. Die benedewindse sy van die plant is beter aangepas vir die kweek van die gras aangesien dit beskerming bied teen die omgewingsfaktore. Die krag analise wat op die plant uitgevoer is toon aan dat die totale krag twee ordegroottes verskil van die skuif krag. Die grootte van die krag is direk eweredig aan die grootte van die plant. Drie kritiese areas is geïdentifiseer en die bestaan daarvan is onafhanklik van die grootte of geometrie van die plant: die stagnasie punt aan die loefsy, die kruin bo-op die plant en die area benedewinds van die plant.

Dedicated to my visionary father for encouraging me to reach for the stars,
and to my practical mother for teaching me to never forget the flowers at my feet.

Acknowledgements

I would like to thank the following people and institutions for providing valuable assistance during the course of this MSc study:

- Professor Thomas M. Harms, as thesis supervisor, for his invaluable guidance and patience, for believing in my abilities and giving me this opportunity. He is truly my academic father.

- Professor Melodie A. McGeoch, Stellenbosch University, for providing me with this opportunity and making the arrangements for the Marion Island expedition.

- Mr. Hugo Zietsman and Lt. Cdr. Johanna Mars, South African Navy, Naval Engineering Section, for allowing me to do this project even though I was contractually bound to the SAN at the time.

- Mr. Andrew Gill, Stellenbosch University, for his advice, assistance and encouragement during the additional experimentation in the wind tunnel.

- Mr. Cobus J. Zietsman, Stellenbosch University, for his advice and assistance during experimental work and preparation for the expedition to Marion Island.

- The National Research Foundation and The South African Department of Environmental Affairs and Tourism, Subdirectorate Antarctica and Islands, for funding and logistical support.

- Dr. P.C. Le Roux, Centre of Invasion Biology, for his patience in answering a vast magnitude of questions regarding *A. selago* and *A. magellanica*.

- Mr. Johan Stander, Stellenbosch University, for challenging my thoughts and ideas on a daily basis.

- Mr Sewis van Zyl and Mr J.C. Ruppersberg, Stellenbosch University, for sitting many hours under our tree, discussing my project and giving me advice while drinking too much coffee.

- Ms Ethel Phiri and Ms Natalie Hausmann, for showing me the wonders of Marion Island while educating me on concepts regarding conservation ecology.

- My parents, sister, brother-in-law and friends, for their unconditional love and everlasting support.

Table of Contents

List of Figures

page

page

page

List of Tables

Nomenclature

A	Area	$[m^2]$
c	constant	[]
C_D	Drag coefficient	[]
C_{po}	Specific heat coefficient	[J/kgK]
C_μ	Specific heat coefficient	[J/kgK]
D	Diameter	[m]
F	Force	[N]
g	Gravitational acceleration	$[m/s^2]$
h	Height	[m]
k	Boltzmann constant	[J/K]
P	Pressure	[Pa]
p_o	Pressure at a stagnation point	[Pa]
p_∞	Pressure in the free stream	[Pa]
Re	Reynolds number	[]
s	Distance	[m]
V	Velocity	[m/s]
v	Potential difference	[V]
u	Velocity	[m/s]
u*	Friction velocity	[m/s]
u^+	Dimensional velocity	[]
t	Time	[s]
y^+	Dimensionless wall distance	[]
zo	Roughness length	[m]
κ	von Kármán constant	[]
μ	Dynamics viscosity	[kg/ms]
ρ	Density	$[kg/m^3]$
τ	Strain	[Pa]
ψ	Stability dependant function	[]

Abbreviations

AMG	Algebraic Multi Grid
BIOGEO	Biological and Geological
CD	Central Differencing
CFD	Computational Fluid Dynamics
CO_2	Carbon Dioxide
DAU	Data Acquisition Unit
DEAT	Department of Environmental Affairs and Tourism
HMS	Her Majesty's Ship
IPY	International Polar Year
NRF	National Research Foundation
PDE	Partial Differential Equation
PPM	Parts per million
RANS	Reynolds-Averaged Navier-Stokes
RE	Reynolds number
SANAP	South Africa National Antarctic Program
SIMPLE	Semi-Implicit Method for Pressure Linked Equations

Chapter 1 – Introduction

1.1 Background

1.1.1 *Azorella selago* as Possible Indicator of Global Warming

The study examines airflow patterns over the cushion plant (*Azorella selago*) on Marion Island as a possible indicator of local climate destabilization due to global warming. According to some scientists (Bate and Morris, 1995, Nordhaus and Boyer, 2003, Weart, 2004) global warming may be referred to as a modern day apocalypse which may end the world as we know it. An increase in the global average temperature will affect many levels of our society: political, ecological, meteorological and agricultural to name but a few.

The main cause of global warming seems to be the enhanced greenhouse effect due to an increase in greenhouse gasses, such as carbon dioxide (CO_2), in the atmosphere. Data derived from Antarctic ice cores indicated that in 1750 the CO_2 levels were 208 ppm (Neftel *et al*, 1985) while the current level is 384 parts per million (ppm) (Tans, 2008). This increase in CO_2 levels is apparently of anthropogenic nature, given that the period before 1750 can be classified as a pre-industrial era. The extent of industrial CO_2 pollution becomes evident when one compares the emissions of a relatively small charcoal fuelled power company such as Eskom to that of volcanic activities. While all volcanoes across the globe contribute a combined 130 to 230 million tons of CO_2 per annum, Eskom alone discharged an estimated 223.6 millions tons of CO_2 into the atmosphere in 2008 (Eskom Annual Report, 2008).

Also, researchers often neglect to take the effects of solar luminosity and orbital forcing into account when investigating the nature of temperature variability on earth. Solar luminosity is the power emitted by the sun in the form of photons. The sun is classified as a weak variable star and contributes minimally to the current temperature variation; the luminosity fluctuates only 0.1% over an eleven year solar cycle. Orbital forcing, also known as Milankovitch cycles, encompasses the collective effect of changes in the earth's movements relative to the sun. The orbital shape, axial tilt, precession and orbital inclination vary in distinct patterns. These changes resulted in 100 000 year ice age cycles during the current Quaternary glaciation period (Shackelton, 2000).

The main effect of global warming is destabilization of local climate systems, which will lead to:

- **A higher incidence of tropical disease vectors**. These are controlled by temperature variation between regions. Warmer weather will increase the spread of diseases such as malaria and yellow fever to higher latitudes than normal.
- **Glacier retreat**. Prevailing theory hypothesise that the Younger Dryas stadial was the result of deglaciation in North America (Broecker, 2006). Fresh water streamed into the North Atlantic Ocean and destabilized the deep ocean circulation patterns, subsequently plummeting the Northern Hemisphere into a 1 000 year cold period. Complete deglaciation will cause an increase in sea levels of up to 7 meters. This rise has the potential to cause wide spread devastation if not properly managed. Extinction of species, loss of coastal ecosystems, flooding of cities, displacement of coastal inhabitants and an increased vulnerability to storm surges is amongst the consequences of rising sea levels.
- **Agricultural activities**. Especially lower social-economic farming communities will be significantly affected by global warming. Quantity and quality of products, loss and gain of cultivated land, frequency and intensity of soil drainage and erosion, water use, reduction in diversity and bio-invasion are aspects of agriculture that will be influenced.

The importance of research on the causes and effects of global warming cannot be questioned. This type of research allows for timely action that can prevent the loss of human life, stress the importance of proper natural resource management and possibly inhibit the extinction of Arctic and Antarctic animal species.

The rate of climate change in the Subantarctic region is greater than the global average. The Prince Edward Islands have the ideal ecosystem, due to its size, isolation and relative simplicity, to be studied as a prediction model for the consequence of climate change and the interaction between various climate related parameters (Kennedy, 1995, Chown, 1997, Chown *et al*, 2000, Gaston *et al*, 2003). Quantifying these environmental effects has been identified as a research priority by the South African National Antarctic Program (SANAP). The objective is to identify variables in ecosystems that may be used in the prediction of the consequences of climate change in general, but more specifically in the Subantarctic region.

The mission of SANAP is to increase the understanding of the natural environment and life in the Antarctic and Southern Ocean through scientific research. This undertaking is realized through the various meteorological, biological and geological investigations that are conducted on Marion Island. Meteorological data gathering activities have been conducted on the island since 1948. This information plays an important role in weather forecasting for South Africa. Since the first biological and geological expedition in 1965, over 800 scientific publications have been produced from island related studies. The knowledge gained through research on Marion Island forms a key element in studies that investigate the effect of human activities on the global climate.

Marion Island (Fig. 1.1) forms part of the Prince Edward Island group. It stretches from 46°49'30"S 37°35'E to 46°58'30"S 37°54' E, approximately 1770 km southeast of Port Elizabeth. The island has a surface area of 290 km^2 and a circumference of 72 km.

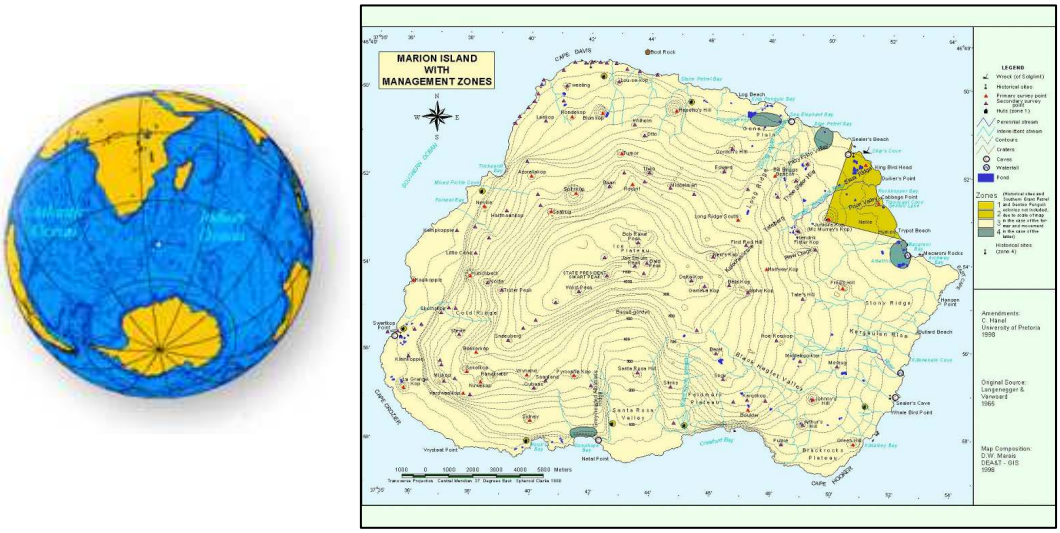

Figure 1.1: Marion Island with management zones (Marais, 1998)

The island was accidentally discovered in 1663 by the Dutch explorer Barent Barentszoon Ham. His vessel, the *Maerseveen*, was on route to the East Indies. The position of the island was wrongly recorded as 41° south and could subsequently not be found during a follow-up expedition. In 1772 the frigate, *Le Mascarin*, was sailing for Antarctica when it came across the islands. The captain, Marion du Fresne, died shortly after this second discovery. It was the explorer, James Cook that formally named Marion and Prince Edward Islands - after Marion du Fresne and the fourth son of King George the third respectively - on 12 December 1775. The first recorded landing took place when the *Catherine*, a British sealer vessel, visited the Island in December 1803. Her captain, John Fanning, noted that there were already signs of previous occupation at that time.

In 1947 *HMS Transvaal* sailed in secret during "Operation Snoektown" to occupy the island before its strategic position could be used against the Union of South Africa. On 29 December 1947 Marion Island was annexed by the Union of South Africa and subsequently the Prince Edward Island Act 43 of 1948 was passed. The Prince Edward Islands were declared special nature reserves in 1995. A special nature reserve is acknowledged to:

- protect highly sensitive, outstanding ecosystems, species (Fig. 1.2), geological or physiological features; and
- be made primarily available for scientific research or environmental monitoring.

Figure 1.2: King penguins at Ship's Cove on Marion Island (Combrinck, 2008)

The cushion plant, *A. selago* (Fig. 1.3), is the focal point of the current study due its wide distribution over the island, as well as the important functional roles it fulfils:

- It is an important nutrient source for micro-arthropod species in a nutrient poor habitat (Hugo *et al*, 2004).
- It is strongly associated with geomorphological processes (Boelhouwers *et al*, 2000). The extensive root system stabilizes slopes and influences the formation of lobes, sheets and terraces and subsequently influences the landscape structure and stability (Boelhouwers *et al*, 2003, Holness, 2003).

Figure 1.3: The keystone plant species, *Azorella selago* (Combrinck, 2008)

It is apparent that a significant change in climate conditions will affect *A. selago* and subsequently the entire ecosystem of the island. In order to accurately predict the impact of climate change on the ecosystem, it is important to understand the flow of air over individual plants. As extensive airflow analyses do not fall within the expertise of ecologist, the task was outsourced to a computational fluid dynamic (CFD) analyst, creating this interdisciplinary opportunity.

1.1.2 Importance of Interdisciplinary Research

Interdisciplinary research is inspired by the drive to provide effective solutions to intricate questions that cannot be addressed adequately by a single discipline. Working across disciplines requires depth of knowledge and a holistic understanding of complex systems. Important discoveries can occur at the intersection between fields. However, mainstream research favours narrowly focused research with clearly defined boundaries between specialities.

The complexity of the overall study necessitated collaboration between various scientific disciplines. This study forms part of the BioGeo project headed by Professor M.A. McGeoch from the Centre of Invasion Biology in Stellenbosch. The BioGeo project aims at exploring the interaction between vegetation, climate, soil and landform processes on Marion Island. It is an ongoing project that will quantify the mentioned interactions as a basis for predicting the effect of current climate change on the terrestrial ecosystem. The component of computational fluid dynamics (CFD) was added to deepen the understanding of airflow on the plant. Subsequently aerodynamics had to be incorporated into the project as it constitutes the basis upon which the relevant CFD simulations are founded. The interdisciplinary approach of the project is depicted in Figure 1.4

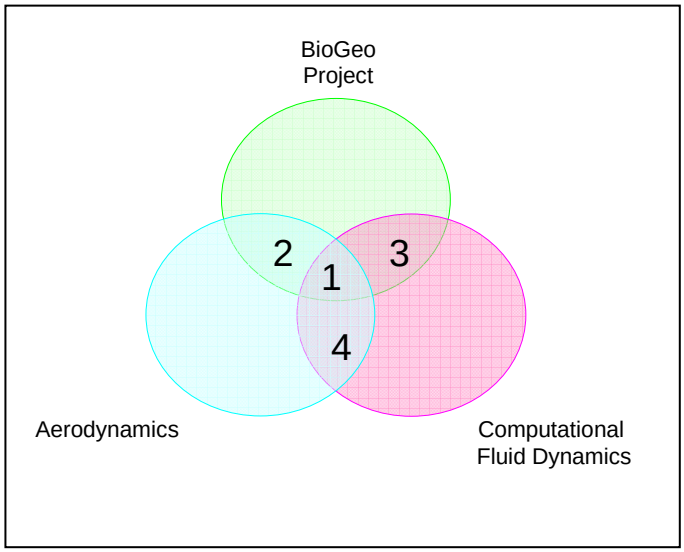

Figure 1.4: Zen diagram depicting the inter-disciplinary nature of the project

Section one of Figure 1.4 denotes the point of interaction between the various elements. Sections two, three and four are possible expansions to the project that can be explored in a subsequent research, possible in a doctoral dissertation. Should a further research be conducted on the overall project, section two will focus on aspects of acquiring more accurate airflow data and environmental readings in order to describe the system more accurately. Section three will deepen the understanding of the influence of airflow on the geomorphology of the island. The correlation between the wind and the spread of invasive species can also be investigated. Section four will aim at acquiring a correlation between measured and simulated results that is of acceptable accuracy.

In order to meet the future requirements of sustaining ongoing development, scientists are required to build networks with other disciplines to establish interdisciplinary communication and collaboration. These alliances push the traditional boundaries of disciplines and subsequently ensure the growth and vitality of academia that may lead to the development of innovative fields. A multi-dimensional approach to the project will benefit humanity by improving the prediction of climate and natural hazards. Ultimately it will provide science-based solutions that support human well-being and the sustained use of natural resources while confronting the threat of global warming.

1.1.3 Computational Fluid Dynamics as Analytical Tool

Computational fluid dynamics (CFD) is a highly interdisciplinary research area. It interfaces physics, applied mathematics and computer programming to form sophisticated analysis techniques. Fluid flow is governed by the three laws of conservation for mass, momentum and energy. The fundamental flow problem can be described mathematically by applying these laws to derive a system of partial differential equations (PDE). Through discretisation the partial differential equations are transformed into algebraic equations. The latter are then solved utilizing iterative computation. CFD obtains a quantitive solution by means of mathematical modelling and numerical methods in appropriate software.

Traditionally, extensive experimentation was required to describe flow patterns. Experiments investigate one quality at a fixed number of points using a limited range of operating condition. Scaling of the model is often required. Computer simulation allows for the prediction of the flow pattern with a high resolution of space and time. All desired quantities can be forecasted in the actual flow domain under any realistic operating conditions. Utilizing CFD as a method of analysis, while not aspiring to replace all important experimental work, significantly reduces the experimentation time and overall project cost.

Experimentation is not made obsolete by the implementation of CFD programs. Results obtained from the latter are merely predictions of the possible flow patterns. The accuracy thereof depends on the soundness of the input data, the

appropriateness of the mathematical model and the available computing power. In this project the solutions will be verified by the convergence of the residuals, the level of grid independence (numerical accuracy) and comparison with the experimental data (model accuracy). The insight gained by conducting an airflow analysis on *A. selago* will be used by the involved ecologists to predict the impact of current climate change trends on *A. selago* and subsequently the involved environment.

1.2 Objectives

Understanding the environmental effects of climate change in polar regions has been identified as a research priority by SANAP and the International Polar Year 2007-2008. This may partially be achieved by quantifying the means in which species interact with the climate and the abiotic environment as even slight changes in temperature and wind direction on Marion Island have the potential to significantly alter the biotic and abiotic patterns and processes.

The keystone plant species *A. selago* is adapted specifically for the sub-Antarctic conditions. The compact, streamlined morphology protects the plant from the adverse wind conditions (Huntley, 1971, Le Roux and McGeoch, 2004) and the restricted vertical growth allows the plant to retain dead leaves within, thus providing a nutrient-rich organic layer (Huntley, 1971) in a nutrient poor environment. It is foreseeable that *A. selago* will be affected by the rapid change in climate. The combination of lower rainfall and high temperature will cause an acceleration of plant senescence and higher stem mortality (Le Roux *et al*, 2005). An increase in temperature will facilitate the colonization of other species such as *A. magellanica*. These species can potentially out-compete *A. selago* for space, light, water and nutrients due to its slow growth and low recruitment (Le Roux and McGeoch, 2004). These cushion plants contribute considerably to the primary production and biodiversity. The plant also interacts with landform processes that structure the landscape. The probable extinction of this species due to climate change will have significant implications for the structure and functioning of the fellfield system.

The effects of changes in airflow on *A. selago* (due to global warming) will have significant implications for the future of the terrestrial ecosystem on Marion Island. The main objective of this study is to quantify the interactions between the airflow and *A. selago* utilizing CFD as an analytical tool. To that effect the following research questions were posed:

- How does airflow over individual cushion plants?
- How is the airflow affected by differences in plant shape and plant size?
- How will the above affect light particle deposition of the grass species, *A. magellanica*, on *A. selago*?
- What physical force does the airflow exert on the cushion structure?

The objectives of the project can be summarised as follows:

- To conduct an airflow analysis on the most basic shape of the *A. selago* and quantify the results.
- To investigate the influence of shape and size on the flow of air over that plant.
- To conduct a particle tracking analysis to determine the location of seed deposition on *A. selago*.
- To conduct a CFD analysis to quantify the total force and shear force exerted on the plant.

1.3 Layout of Thesis

This thesis consists out of seven distinct chapters:

Chapter 1 – Introduction

Chapter 2 – The Nature of Airflow over an Individual Cushion Plant

Chapter 3 – The Effect of Plant Shape and Size on Airflow

Chapter 4 – Light Particle Deposition of *A. magellanica* on Cushion Plants

Chapter 5 – The Exertion of Physical Force on the Cushion Structure

Chapter 6 – Conclusion

Chapter 2 – The Nature of Airflow over an Individual Cushion Plant

2.1 Introduction

Various sources in the literature (Bakić, 2004, Constantinescu and Squires, 2004, Raithby and Eckert, 1986) present the idea that although the sphere is of simplistic geometry, the flow field is extremely complex. Flow structures, such as the large scale vortex shedding in the turbulent wake and transition from laminar to turbulent flow, is difficult to accurately capture in numerical models. The modelling of flow in the near wall turbulent region has the reputation of being the "Achilles heel" of computational fluid dynamics (CFD). Constantinescu and Squires, (2004) noted that: "…wall-layer modelling remains a topic of considerable fundamental interest for which new modelling strategies are being actively pursued…". It is apparent that although a certain degree of accuracy can be expected, turbulence modelling is far from perfect (Spalart, 2000).

Every problem is unique. It is imperative that experimental work be conducted in order to determine whether the CFD methodology and turbulent models incorporated are appropriate and correctly applied. In the hands of the ignorant user, CFD is yet another method of displaying inaccurate results in an aesthetically pleasing manner.

This chapter reports on an experiment that was conducted in a wind tunnel and the subsequent computational analysis thereof. The overall aim of the chapter is to investigate the nature of airflow over an individual cushion plant. The objective of the experiment was to obtain a static pressure profile over a hemisphere at various free stream velocities. Turbulence was generated artificially in the test section of the wind tunnel through the installation of a metal grid. The resulting turbulence intensity and velocity profiles were measured using hotwire anemometry. A computational fluid dynamic analysis was done to describe the independent and dependent variables in a comprehensible and visual manner. Results obtained from the experiment were compared to data attained during the CFD analysis. This comparison assesses the accuracy of the computational process.

A distinct evolution of shape was identified for *A. selago.* Initially the plant is in the shape of a small hemisphere. As the plant matures, this shape develops in one of three larger forms: hemispherical, hemi-ellipsoidal or crescent. The focal point of this chapter is the airflow over the most elementary structure of the plant: a hemisphere with a diameter of 0.15 m and height of 0.075 m.

2.2 Flow over a Sphere in the Literature

This section provides a brief overview of the most important findings in the literature regarding flow over spheres. Although many articles were consulted on this matter, the results of only three are pointed out. The cited articles aided in the understanding of the fundamental concepts of fluid flow over a sphere.

2.2.1 Experimental Investigation by Bakić (2004)

Bakić's (2004) experimental investigation of flow around a sphere reveals four different flow regimes of which the fourth is divided into four turbulent wake regions. Each regime is identified by unique characteristics of separation, vortex shedding and wake stability. Each regime is distinguished by its Reynolds number (Re):

- Re < 20. No separation or vortex shedding is observed in this regime. The wake is laminar.
- 24 < Re < 210. Separation occurs and results in an axis symmetric, laminar wake. No vortex shedding is observed.
- 270 < Re < 800. The laminar wake becomes unstable. The onset of vortex shedding is observed.
- Re > 800. Onset of the turbulent wake and rapid diffusion of vortex loops. This regime is divided into four regions:
    - Subcritical Region. $800 < Re < 3.3*10^5$
    - Critical Region. $Re \approx 3.3*10^5$
    - Supercritical Region. $3.3*10^5 < Re < 2*10^7$
    - Transcritical Region. $Re > 2*10^7$

Bakić's study comprises out of three different experimental configurations:

- flow around a smooth sphere,
- flow around a sphere with a trip wire and
- flow around a sphere in a flow with high free-stream turbulence.

The experiments show that the flow and turbulent characteristics in these cases are significantly different, and that an increase in turbulence intensity in the free stream results in:

- the position of the separation point on the sphere moving further downstream,
- later separation of the boundary layer,
- an increase in mixing processes and entrainment,
- a decrease in the recirculation zone and subsequently the reattachment point and
- an increase in the Reynolds stresses in the fluid.

The work of Bakić (2004) is further supported by both Raithby and Eckert (1986) and Constantinescu and Squires (2004). There are, however, disputes over the exact value of the critical region. According to Bakić (2004) the critical Reynolds number is located at $3.3*10^5$, while Constantinescu and Squires (2004) state that it is located at $3.7*10^5$.

2.2.2 Numerical Investigation by Constantinescu and Squires

The numerical investigations of flow over a sphere in the subcritical and supercritical regimes (Constantinescu and Squires, 2004) convey four very important concepts:

- the spiral instability mode
- the axisymmetric instability mode
- the drag crises
- the lateral force instability mode

The spiral instability mode is associated with large scale vortex shedding in the laminar and subcritical regimes for a Re above 270. It is present in the flow field due to the coherent rotation of the recirculation zone and manifests as a progressive wave motion with alternate fluctuations produced by the shear layer. In this context the periphery between the recirculation zone and the exterior fluid is referred to as the shear layer. The alternate fluctuations cause the periodic shedding of vortices to form a completely laminar wake. Constantinescu and Squires (2004) refer to the spiral instability as the "hairpin" vortex, but it is more commonly known as the "horseshoe" vortex.

The axisymmetric shedding of vortex tubes, due to pulsations in the separated shear layer, becomes noticeable at a Re higher than 800. It is associated with the small scale Kevin-Helmholtz instability in the shear layer. This vortex shedding mode is responsible for distortion of the large scale vortex structures, shedding of vortices in a quasi-coherent fashion and the transition of the detached shear layer to fully turbulent. The axisymmetric instability and the axisymmetric instability co-exist in the subcritical region.

The flow regime over a sphere is known for its drag crises: the reflection of the significant difference between the separation of the laminar and the turbulent boundary layers. The value of the drag coefficient instantly decreases from approximately 0.4 to approximately 0.07 as transition occurs. In the light of this the numeric treatment of the boundary is of utmost importance as simplistic treatment of the attached boundary layer will lead to inaccurate results. It is furthermore noted that the separation point of the sphere moves further downstream when the flow is in the supercritical regime. The separation point is located at 81° and 120° respectively for the subcritical and supercritical regime. A more compact recirculation zone develops when transition occurs which result in a unique wake structure and vortex shedding. The change in wake structure

induces a lateral force on the sphere that tilts the wake relative to the streamwise axis. The experimental work of Achenbach (1972) and Taneda (1978) confirms the existence of this lateral force.

2.2.3 Visualization Investigation by Bakić and Perić (2005)

Bakić and Perić (2005) use visualization techniques to illustrate that the main characteristic of flow around a sphere is the presence of a turbulent wake with recirculation. The extent of the region depends on the shape, orientation and size of the body. The velocity and viscosity of the fluid also plays a major role as it influences the vorticity and instabilities in the flow.

It was determined that for a Re lower than 20 all regions of the flow are laminar. The onset of separation occurs at Re ≈ 24. Separation results in the generation of a stable axisymmetric vortex ring that is visible up to a Re of 400. In the range $210 < Re < 270$, transition in the wake results in the single vortex thread becoming twin threaded. These two threads are stable up to a value of 270 when vortex loops begin to shed from the sphere forming a completely laminar wake. The wake flow becomes turbulent at Re ≈ 800, at this point the vortex loops diffuse very rapidly. For Reynolds numbers higher than 2000 these patterns in the flow become well established in the form of horseshoe vortices

Bakić and Perić (2005) documents two Strouhal numbers, a high mode and a low mode that are associated with the small scale instability of the separated shear layer and with the large scale instability of the wake. It is noted that earlier transition of the boundary layer, from laminar to turbulent, results in later separation and a reduction in drag. In the subcritical regime separation occurs at 81° and in the supercritical regime only at 102°. The Re associated with transition varied between 250 000 and 350 000 from experiment to experiment. Bakić and Perić (2005) concludes that the wake structure and vortex configuration of a sphere is more complex than the simple single or double threaded vortex arrangement reported in previous articles. There exists a sub-harmonic frequency component within the natural instability that is associated with the Strouhal high mode.

2.2.4 Alignment of Current Research Topic with Literature

There are disagreements in literature about the exact value of the Re where transition occurs. This is because the transitional Re is extremely sensitive to free stream disturbances. These disturbances can be due to:

- grid generated turbulence
- acoustic noise
- excited standing waves
- excited travelling waves

The numerical investigation conducted by Constantinescu and Squires (2004) indicates that a transitional Re of 370 000 is associated with 0 % free stream turbulence. Furthermore, Bakić (2004) finds values between 300 000 and 330 000 associated with a turbulence intensity of 7.8 %. The deduction can therefore be made that the value of the transitional Re decreases when the value of the free stream disturbances increase.

In the current case study the plant and its immediate surroundings are represented by a hemisphere resting on a flat plate in fully turbulent airflow. Atmospheric airflow is inherently turbulent due to the distance travelled by the fluid and the surface roughness on ground level. Conducting an atmospheric airflow analysis in the laminar regime would be a futile exercise. In the light of this, all simulations are conducted in the turbulent regime. Turbulence is artificially generated in the wind tunnel by means of a square, welded grid. The flow regime is not allowed to naturally progress from laminar to turbulent, but is forced through bypass transition into the turbulent regime. The transitional Re for a flat plate can subsequently be determined by an equation such as Equation 2.1 (White, 2006). In this equation T represents the turbulence intensity and is taken as a fraction and not a percentage.

$$\mathrm{Re}_{x,tr} = \frac{-1+\sqrt{1+132500T^2}}{39.2T^2} \tag{2.1}$$

It should be noted that flow over a spherical object is so sensitive to eddies and vortices in the flow field that a turbulence sphere can be used to measure turbulence intensity. This sensitivity can be attributed to the occurrence of vortex shedding from the sphere at Reynolds numbers as low as 270. The presence of eddies and vortices in the flow relate directly to the regime - laminar or turbulent - of the fluid. The instabilities enhance the inertial forces in the flow that in turn cause a decrease in the transitional Re. Earlier transition leads to steeper velocity gradients that result in prolonged attachment of the flow to the hemisphere. The flow will not separate from the hemisphere in the absence of an adverse pressure gradient, which causes a decrease in the velocity gradient along the surface of the hemisphere. The velocity gradient normal to the wall will continue decreasing until it reaches zero, then the wall shear stress will also reach zero. At this point, the flow will separate from the hemisphere because the shear stress responsible for keeping it attached has disappeared. Various articles in the literature (Bakić, 2004, Constantinescu and Squires, 2004, Raithby and Eckert, 1986) clearly state that the elevation angle associated with the separation point is an indication of the flow regime. In the laminar regime the separation point is expected at 81º, while in the turbulent regime it can be found between 102º and 120º. The experimentally determined separation point in the present work is determined at approximately 120º, with a Reynolds number based on a full sphere in the order of 100000 to 300000.

2.3 Experimental Analysis

2.3.1 Initial Considerations

It was explained in Chapter 1 (Section 1.1.4) that results obtained from CFD simulations must be verified using appropriate methods. Comparison between CFD results and experimental data is therefore a very important part of the verification process. This experiment replicates the airflow over the most basic form of the cushion plant. A static pressure profile will be obtained and will serve as basis for comparison.

Airflow in the field is of an irregular and turbulent nature, therefore it would be extremely difficult to replicate the exact environmental conditions in a simulation. In order to authenticate the numerical methods that were employed, the simulation conditions are required to be as close as possible to those of the experiment. Experimentation in a wind tunnel allows for the effective control of independent variables, in this case the free stream velocity and turbulence intensity, thus creating more reliable dependent variables (static pressure). The velocity is controlled in the tunnel through the hydraulic gates and turbulence is artificially generated by means of a squared, welded grid place at the test section inlet.

Direct experimentation on *A. selago* will result in destructive testing. Using a generalized shape portraying *A. selago* in the laboratory is a more environmentally friendly technique. The plant is extremely dense to such an extent that it can be assumed that the porosity is negligible. To simplify the experiment the surface roughness is not brought into calculation. The velocity profile and turbulence intensity profiles are measured at a distance 0.09 m in front of the plant. This data is used to generate the inlet velocity profile of the CFD model and subsequently to calculate the experimental turbulence kinetic energy and dissipation profiles. Heat transfer is not taken into account due to the micro-scale thereof. Dimensional analysis is not required in this case, as no scaling factors are incorporated in the test model.

2.3.2 Experimental Setup

Equipment

Table 2.1 lists the equipment that was used in the wind tunnel experiments. The subsonic wind tunnel that was used in the experiments is managed by die Department of Mechanical and Mechatronic Engineering. A layout of the tunnel is shown in Appendix A. This open circuit tunnel consists of:

- an electric power suction fan

- the electrical-hydraulic control gates (Fig. 2.1)
- diffuser and chimney
- two interchangeable test sections (Fig. 2.2)
- the intake nozzle
- the turbulence screens
- the guiding fins and
- the intake section (Fig. 2.3)

Table 2.1: Equipment used in wind tunnel experiments

Item	Model	Serial number	Manufacturer
Transducer	750D-215	1527711	Auto Tran Inc.
Transducer	750D-215	1527732	Auto Tran Inc.
Transducer	860-0.00/2.50-K-18-2-P	B043308	Auto Tran Inc.
Transducer	860-0.00/2.50-K-18-2-P	B043310	Auto Tran Inc.
Transducer	860-0.00/2.50-K-18-2-P	B043312	Auto Tran Inc.
Transducer	860-0.00/2.50-K-18-2-P	B043313	Auto Tran Inc.
Transducer	860-0.00/2.50-K-18-2-P	B043314	Auto Tran Inc.
Transducer	860-0.00/2.50-K-18-2-P	B043315	Auto Tran Inc.
Transducer	860-0.00/2.50-K-18-2-P	B043316	Auto Tran Inc.
Hot wire probe	-	-	-
Hot wire probe support	-	-	-
Intelligent Flow Analyser (IFA)	IFA 100 - 158	275B	TSI Inc.
Datalogger	USB-6218	E61523	National Instruments
Betz Manometer	-	164402	-
Pitot-Static Tube	-	-	-
Mercury Barometer	-	-	-
Subsonic Wind Tunnel	-	47507	-
Meaurements and Automation	VI Logger	-	National Instruments

Figure 2.1: The suction fan and control gates

Figure 2.2: Interchangeable test section with plant model


Figure 2.3: Wind tunnel intake section without additional turbulence grid

Configuration

The inlet velocity profile in the test section of the wind tunnel was previously measured (Stander, 2004) after the installation of a vehicle test ramp upstream of the removable test section. Analysis of the measurements indicated that the horizontal velocity profile is constant below 60 m/s. Data from Stander's study also indicates that the vertical velocity profile is constant and fully developed. The boundary layer in the test section is less than 0.2 m from the floor at very high velocities. Measurements indicate that the free stream turbulence intensity in the wind tunnel is approximately 0.8 % in absence of a turbulence grid.

For the current study, the hemisphere model was secured 0.345 m from the floor of the test section on top of a mild steel plate (Fig. 2.4). Nine pressure points are drilled into the model to form the profile over the hemisphere. Plastic tubes were connected to each of these points, connecting it to the various pressure

transducers. The transducers are connected to the USB-6218 data logger. The velocity and turbulence intensity profiles in the tunnel were determined by using a two-channel hotwire anemometer. The probe is held in place with a probe support that in turn rests on a frame previously constructed for this purpose. The support is connected to the data logger via the intelligent flow analyser, IFA 100. A pitot-static tube is used to determine the free stream velocity during profile measurements and is connected to the data logger via the pressure transducers. The data logger is connected to the computer via the USB port. All data obtained from the data logger was captured utilizing an appropriate measurements program, *VI logger*. Turbulence is generated artificially by means of an additional turbulent grid at the inlet of the test section; this grid was placed on top of the mild steel plate (Fig. 2.5). The diameter of the grid wire is 5 mm and the distance between the centrelines of the wires are 50 mm.

Figure 2.4: Configuration of the model in the wind tunnel

Figure 2.5: Wind tunnel inlet section with additional turbulence grid

Calibration

The following equations are a result of the calibration of the transducer using the Betz manometer:

B043316: Pa = 227.625*v - 305.115 (2.2)
B043314: Pa = 280.392*v - 301.919 (2.3)
B043310: Pa = 275.429*v - 278.032 (2.4)
B043308: Pa = 278.076*v - 249.807 (2.5)
B043312: Pa = 280.426*v - 303.979 (2.6)
B043315: Pa = 279.456*v - 294.309 (2.7)
B043313: Pa = 279.029*v - 294.771 (2.8)
1527711: Pa = 221.300*v - 221.62 (2.9)
1527732: Pa = 222.310*v - 221.09 (2.10)

The hotwire anemometer is calibrated using the instructions in the IFA-100 operator's manual.

2.3.3 Experimental Procedures

Experiments in the wind tunnel must be conducted with due care to ensure safety whilst not compromising the accuracy of the test results. The mouth of the inlet section is not situated outside of the building, but opens into a courtyard adjacent to an industrial retractable door. This door must be fully opened during experimentation to ensure that sufficient flow is available in the wind tunnel and that the velocity profile is constant over the entire test section. Before experiments are conducted, a thorough inspection of the facility and its parts must be conducted. Leaves, sand and other contaminants accumulate at the entrance of the tunnel and will damage equipment if it is allowed to travel through the system. The fan of the tunnel is exposed to the elements, therefore it is not uncommon for water to accumulate at the base of the fan housing. The water must be cleared away as the presence thereof during operations can compromise the structural integrity of the fan blades. The hydraulic doors of the tunnel must be fully closed before activation of the fan. Ear protectors must be worn at all times because the noise level during operation is well above the safety level for the unprotected ear.

For this study, four sets of measurements are taken during the experimentation:

- The first set contains static pressure profiles over the contour of the hemisphere at three different velocities. This data will characterise the static pressure properties of the hemisphere and will be utilized as reference data during the verification process of the CFD generated result.

- The second set contains horizontal turbulence intensity measurements that will quantify the dissipation of turbulent kinetic energy down wind of the additional turbulence grid.
- The third set contains vertical velocity and turbulence intensity data. This data will be used to generate the inlet velocity and turbulence profiles that will be used in the CFD analysis.
- The fourth set contains data from the pitot static tubes from which the stagnation, static and dynamic pressures in the free stream will be derived. This will be incorporated into the CFD simulations at reference data.

The sampling rate of the first and fourth sets taken using pressure transducers with atmospheric pressure as reference is 1000 Hz for 5 seconds. The sampling rate of the second and third set, acquired through the use of the hotwire probe, is 100 000 Hz for 1 second.

There are various types of errors that can occur during experimentation, the most common are random and systematic errors. The random errors in this case are taken as the variation in readings due to the fluctuation of the flow field. These errors are represented in Appendix B Table B.1 by the standard deviation as a percentage of the average value. Zero readings are for each of the transducers and hotwire channels before and after the conduction of the experiments. The systematic errors are represented by the drift in the averages of the pre- and post experimental zero readings. Further deviation can occur due to non-systematic errors such as the change in environmental conditions during experiments, human errors, reading errors and probe calibration techniques.

2.3.4 Results from Experiments

The conventional approximation of isotropic turbulence in a wind tunnel is achieved by the placement of a square, welded grid at the inlet of the test section. It has been found that the turbulence is isotropic downstream of the grid (Liu *et al*, 2003). The ratio of the streamwise turbulence over the cross-streamwise turbulence approaches one, therefore Equation 2.11 applies. This will simplify the calculation of the turbulence intensity (Eq. 2.12) and turbulent kinetic energy (Eq. 2.13).

$$u' \approx v' \approx w' \tag{2.11}$$

$$I = \frac{\left(\frac{1}{3}(u'^2 + v'^2 + w'^2)\right)^{0.5}}{U} \tag{2.12}$$

$$\therefore I = \frac{u'}{U}$$

$$k = \frac{1}{2}(u'^2 + v'^2 + w'^2)$$

$$k = \frac{3}{2}(u'^2) \qquad (2.13)$$

$$k = \frac{3}{2}(UI)^2$$

The dissipation rate of turbulent kinetic energy is determined using Equation 2.14 (White, 2006). In this equation, C_μ is 0.09 and ℓ is the diameter of the wire in the grid. The equilibrium profile equation for epsilon (Eq. 2.15) is not used because it is more appropriate for use in a very large domain and after a grid free stream equilibrium can not be assumed. Neither k nor ε will approach zero directly behind the grid. Turbulence is decaying downstream (towards the free stream condition, but nowhere near yet), and hence there is turbulence dissipation after the grid proportional to the length scale (size of eddy shed behind the wire). Equation 2.15 will let it go to zero (atmosphere free stream) as y increase.

$$\varepsilon = C_\mu{}^{0.75} k^{1.5} / \ell \qquad (2.14)$$

$$\varepsilon = C_\mu{}^{0.75} k^{1.5} / \kappa y \qquad (2.15)$$

Decay of turbulence behind a grid can be described by Equation 2.16 (Lui *et al*, 2004). In this equation *A* is a universal constant, *x* is the distance downstream of the grid, *D* is the distance between the centrelines of the grid wires and x_0 is the virtual origin. The value parameter *n* varies for different studies.

$$\left(\frac{u'}{U}\right)^2 = A\left(\frac{x}{D} - \frac{x_0}{D}\right)^{-n} \qquad (2.16)$$

Figure 2.6 displays the decay of turbulence in the wind tunnel for various free stream velocities. Equation 2.16 is superimposed on the turbulence data to produce Equations 2.17, 2.18 and 2.19 which described the decay for 10 m/s, 20 m/s and 30 m/s respectively.

$$\frac{u'}{U} = 36.85\left(\frac{x}{0.05}\right)^{-0.6804} \qquad (2.17)$$

$$\frac{u'}{U} = 30.19\left(\frac{x}{0.05}\right)^{-0.7064} \qquad (2.18)$$

$$\frac{u'}{U} = 28.26\left(\frac{x}{0.05}\right)^{-0.7369} \tag{2.19}$$

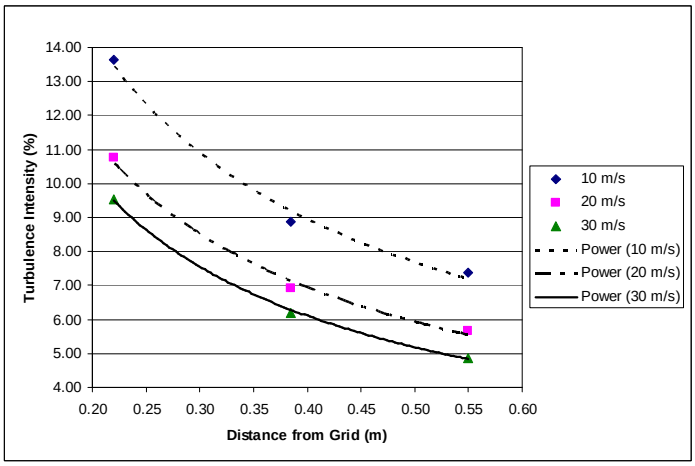

Figure 2.6: Decay of turbulence in the wind tunnel

Vertical velocity and turbulence intensity profiles are taken at positions 0.385 m and 0.55 m from the turbulence grid. The data at the position 0.385 m from the grid will be used to determine the inlet properties of the CFD model. It can be seen in Figure 2.7 that the flow is fully developed and turbulent. This is indicated by the constant velocity in the area outside of the boundary layer. The deviation in the free stream values from point to point can be attributed to experimental error. The turbulent boundary layer is made visible by the decreased value of the first three nodes. In the CFD model the velocity distribution within the turbulent boundary layer can be approximated with the Law-of-the-Wall in a high Reynolds turbulent mode. The wall functions for the viscous sublayer and the logarithmic distribution layer apply within the turbulent boundary layer. The velocity reading at the surface of the plate is taken as zero due to the non-slip nature of the flow and the stationary wall.

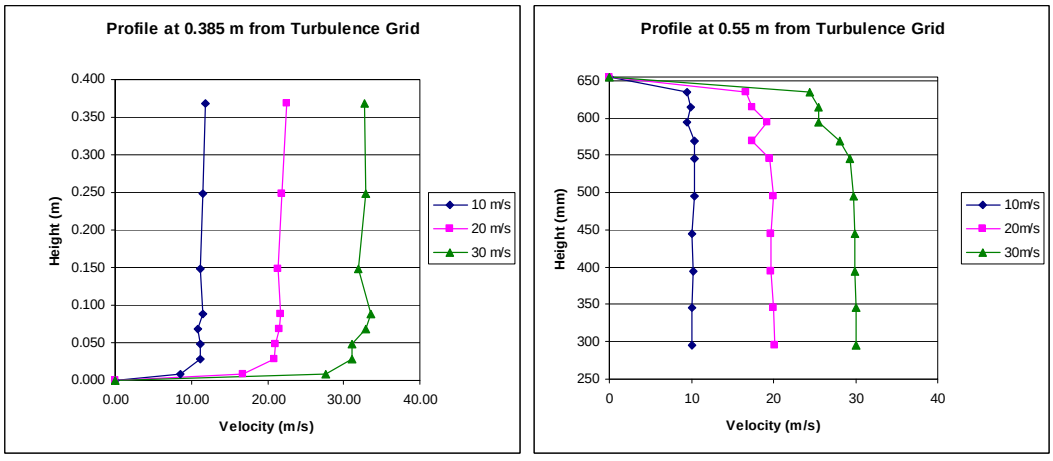

Figure 2.7: Velocity profiles in the wind tunnel

The profile of the turbulence intensity was anticipated. Firstly it should be noted from Figure 2.8 the turbulence intensity increases as the free stream velocity decreases. This is due to the constant vortex size shed from the wire grid being superimposed on decreasing average velocities. Secondly it should be noted that for a given free stream velocity, the turbulence intensity increases as the nodes approaches the wall. This can be explained by Equation 2.12 where turbulence intensity is a function u' and a decreasing U. In the boundary layer the velocity decreases as it is measured closer to the wall, faster than e.g. turbulent eddy sizes. This results in an increase in turbulence intensity near the wall. Furthermore using Equation 2.1 and the data from Figure 2.6 it can be shown that the upstream flat plate boundary layer is immediately turbulent.

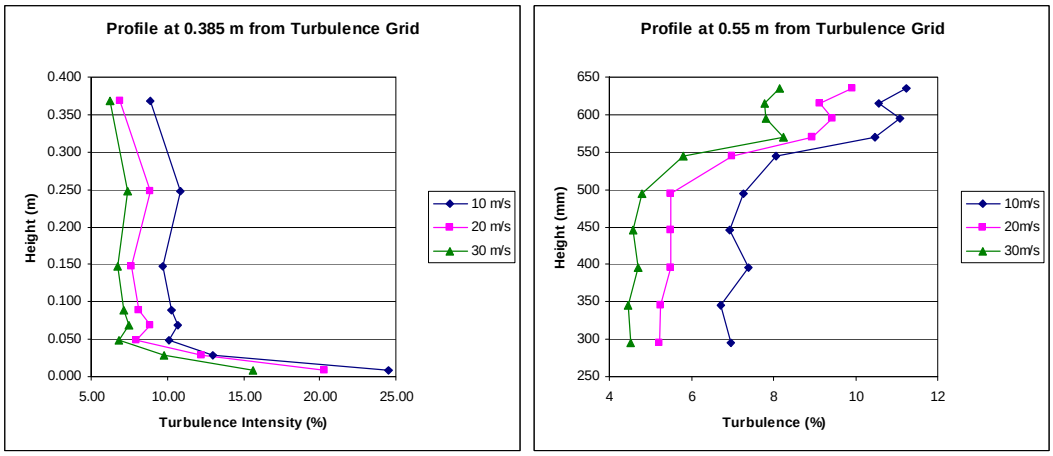

Figure 2.8: Turbulence intensity in the wind tunnel

Figure 2.9 displays the profiles of the turbulent kinetic energy and the dissipation thereof. These graphs are calculated by using Equation 2.13 and Equation 2.14 respectively. These profiles will be implemented into the CFD model to specify the properties of the inlet boundary. Note that neither of the graphs approaches zero in the free stream as previously discussed.

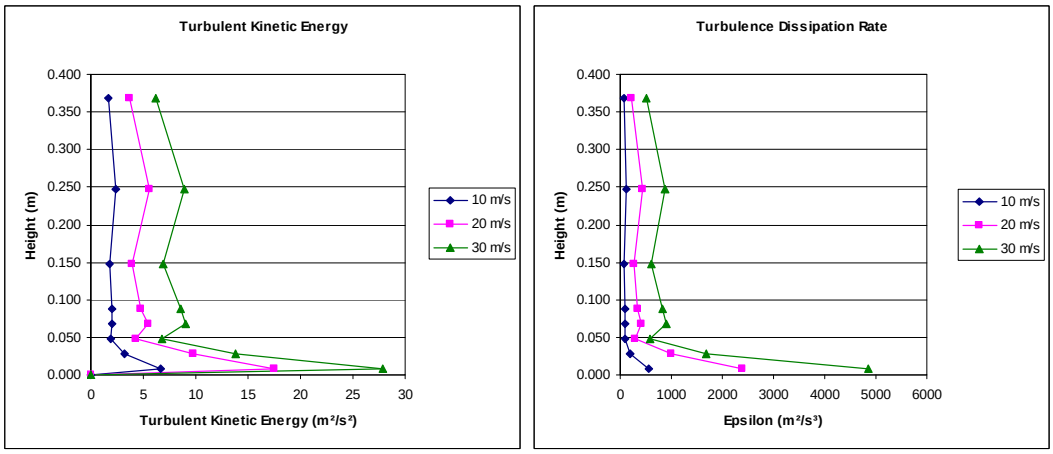

Figure 2.9: Turbulent kinetic energy profiles at a position 0.385 m from the grid

The static pressure profiles are derived from data obtained at the pressure points. The data, obtained as voltage values, is converted to gauge pressure readings using the calibrations graphs. The pressure coefficients are calculated using the static pressure data in the free stream obtained with the pitot-static tube and the gauge pressure readings (Fig. 2.10). The atmospheric pressure is determined using a mercury barometer and the absolute pressure was subsequently obtained for each point. The values of the stagnation pressure in the free stream are obtained in a similar manner and will be used as reference values in the CFD simulations. A sample calculation is available in Appendix B.

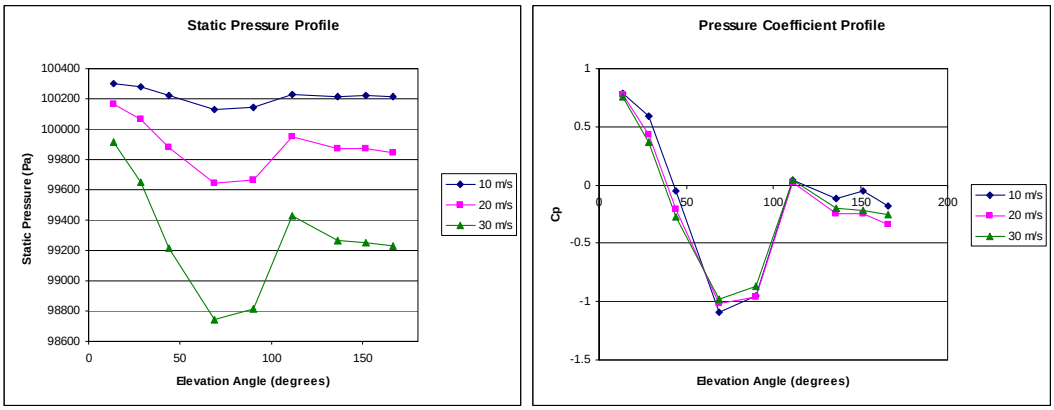

Figure 2.10: Pressure profiles over the contour of the hemisphere

The pressure coefficient profile obtained from the experiment is compared to a profile contained in the work of Constantinescu and Squires (2004), and obvious similarities in the profiles were found. The dissimilarities can be attributed to the geometric differences between the hemisphere on a plate (further referred to as the case study) and a standard sphere (further referred to as the baseline) in fluid flow. The baseline (Fig. 2.11) indicated a definite stagnation point at an elevation angle of zero. The pressure at the same location on the case study was not measured, but it is unlikely that it will reach stagnation due to the geometric differences. Directly in front of the hemisphere the flow will already be forced in an upward direction and thus maintain a velocity gradient. At an elevation angle of 14º, the pressure coefficient of the case study is significantly lower than in the baseline. The onset of the adverse pressure gradient in both cases occurs before the apex of the objects. The delay in flow detachment due to the turbulence causes a very low pressure coefficient at the adverse pressure gradient. The value at this point compares well with the value of the case study. Separation of the boundary layer occurs at 120º in both cases. This is confirmed by visualisation experiments using oil and powder paint (Fig. 2.12). This is inline with the literature discussed earlier in this chapter; in the supercritical regime the separation point on a sphere will occur between 102º and 120º.

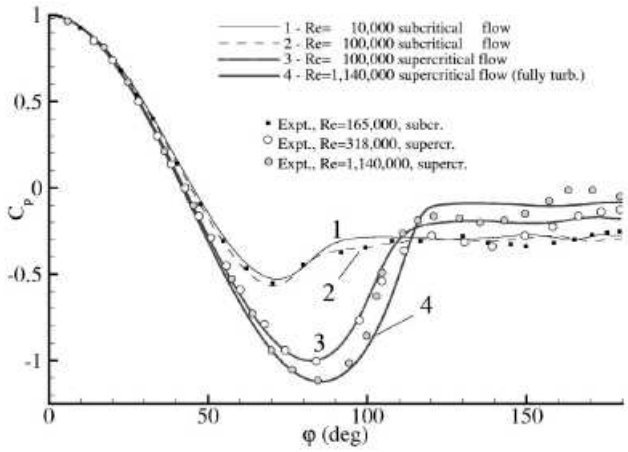

Figure 2.11: Cp from the literature (Constantinescu and Squires, 2004)

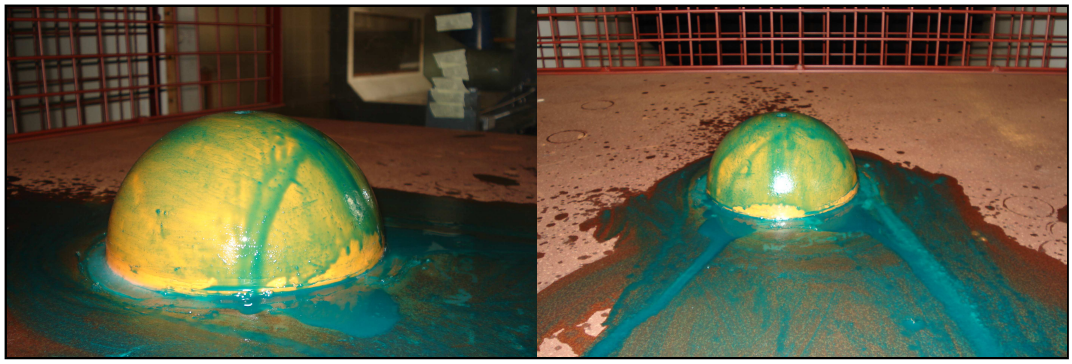

Figure 2.12: Visualization experiments in the wind tunnel

2.4 Computational Fluid Dynamic Analysis

In the previous section the results of a wind tunnel experiment was documented in detail. This section reports on the subsequent CFD analysis of that experiment. The methodology and theory implemented to construct the CFD model and programming the relevant parameters is discussed in Section 2.4.1. The conditions under which such a simulation is considered to be solved, is examined in Section 2.4.2, while the results of the simulations under various turbulence modelling conditions are discussed in Section 2.4.3.

2.4.1 Pre-processing

The control volume of the model is constructed to adhere to the dimensions of the wind tunnel test section. The dimensions are taken as 2.5 x 1.42 x 0.655 m where

0.655 m is the distance from the upper flat plate to the roof of the test section. The diameter of the hemisphere is 0.15 m with a height of 0.075 m. All surfaces are defined as wall boundaries except for the inlet boundary (Fig. 2.13, red area) and the outlet boundary (Fig. 2.13, green area). The velocity and turbulence intensity profiles are measured at a distance 0.09 m upstream of the hemisphere. The inlet section of the model is therefore 0.09 m from the hemisphere since the inlet parameters can be defined according to the experimental data. The generation of the mesh is influenced by the selected turbulence model, as a low Re model will call for more cells in the near wall region allowing for appropriate y^+ (dimensionless wall distance) values and solving of the boundary layer.

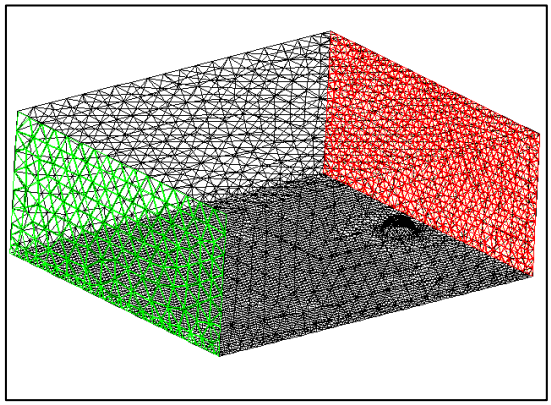

Figure 2.13: Control volume and plant model with inlet en outlet boundaries

At this point it may be expedient to briefly revisit the Law-of-the-Wall theory to clarify the difference between the low Re turbulence model approach and the high Re turbulence model approach. In the wind tunnel experiment a turbulent boundary layer is present almost directly behind the turbulence grid, which was calculated Equation 2.1. It can also be seen in the velocity and turbulence profiles measured at 0.385 m from the turbulence grid. Three sections can be identified in a turbulent boundary layer:

- the viscous sublayer
- the logarithmic velocity distribution layer
- the buffer zone that divides the two layers

Equation 2.20 and Equation 2.21 displays the correlations of the viscous sublayer and logarithmic layer respectively. The Law-of-the-Wall does not bring the buffer zone into calculation, but extends the viscous sublayer and the logarithmic velocity distribution layer to the point of intersection where y^+ is approximately 11.84. The y^+ values (Eq. 2.22) are of special significance when generating the cell in the near wall regions of the grid because it influences the accuracy of the turbulence model employed. A low Reynolds turbulence model would require a y^+ value at the wall in the order of 1. The first node must be in the viscous sublayer because the turbulence kinetic energy and the dissipation thereof are solved analytically throughout the boundary layer. This approach also requires at

least 10 prism layers within the boundary layer, making it computationally very expensive. An alternative method that is less expensive is the high Reynolds turbulence model approach. The y^+ value at the wall must be chosen to allow the first node to be situated in the logarithmic velocity distribution layer. The logarithmic velocity profile is valid for y^+ values between 30 and 500, but it is common practise to only allow for numbers between 30 and 300. In this chapter both the high- and low Re turbulence models are used and compared to the experimental data. Figure 2.14 shows the velocity distribution in a turbulent boundary layer in terms of dimensionless wall distance (u^+) and dimensionless velocity (y^+).

$$u^+ = \frac{u}{u*} = \frac{u*y}{\upsilon} \tag{2.20}$$

$$u^+ = \frac{u}{u*} = 5.75\log(\frac{u*y}{\upsilon}) + 5.56 \tag{2.21}$$

$$y^+ = \frac{u*y}{\upsilon} \tag{2.22}$$

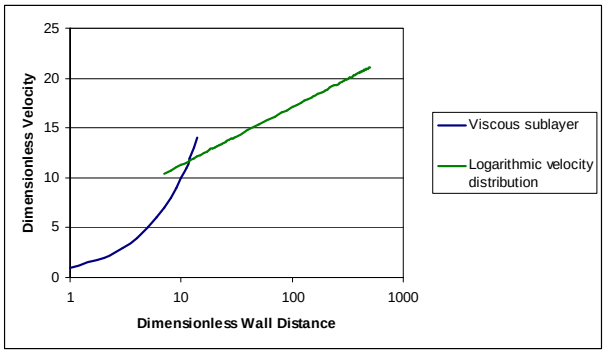

Figure 2.14: Velocity distribution in a turbulent boundary layer

Twelve meshes are generated to solve the CFD model for three free stream velocities, namely 10 m/s, 20 m/s and 30 m/s. Each free stream velocity has four distinct meshes. The first three of each velocity is constructed to determine grid independence for a high Re turbulence model application. The fourth is specifically generated for a low Re turbulence model application. The complete grid information is shown in Appendix B, Table B.2. It is standard practise that at least three meshes is required for a mesh to be proved grid independent, each refined to double the cell amount of the preceding. The grid independence of the model is further discussed in the Section 2.4.2.

The models are created using tetrahedral cells with a layered mesh structure at the boundaries. Although the polyhedral cell is the most effective and accurate it is not available in StarCD 3.24. Therefore, tetrahedral cells were selected because it

is most efficient for the treatment of boundary layers, since it can be constructed with a high aspect ratio without the hazard of creating acute angles. This type of cell is capable of following the geometric feature of a model with utmost precision. In the book *Grid generation methods*, Liseikin (1999) states that the tetrahedral cell is the simplest three dimensional volume and it is superior in its "…applicability to virtually any type of domain configuration." The drawback of using this type of cell is that it is computationally very expensive but geometric precision took preference over computational expense in this case.

The inlet profile is configured according to the experimental data. The FORTRAN programs that governed the velocity, turbulent kinetic energy and dissipation equations are displayed in Appendix B. The velocity profiles are derived from Equation 2.20 for the viscous sublayer, and Equation 2.21 for the logarithmic profiles. The parameters for these equations are displayed in Table 2.2, where the Re applies to the flat plate at the 0.385 m from the turbulence grid. Turbulent kinetic energy and dissipation are determined using Equation 2.13 and Equation 2.14.

Table 2.2: Velocity inlet parameters

Velocity	u*	u	τ	Re	δ	δ' (Law of the Wall)
10 m/s	0.448005	8.61	0.24085	254966.9	0.010985	0.000399067
20 m/s	0.811943	16.81	0.791102	509933.8	0.009563	0.000220193
30 m/s	1.267448	27.65	1.927708	764900.7	0.008818	0.000141058

The following turbulence models are implemented independently:

- k-ε high Re turbulence model
- k-ε RNG Re turbulence model
- k-ω SST high Re turbulence model
- k-ω SST low Re turbulence model

2.4.2 Solving

The algebraic multi grid (AMG) solution method combined with the Semi-Implicit Method for Pressure Linked Equations (SIMPLE) solution algorithm is used to obtain numeric convergence of the solution. Central differencing with a blending factor of 0.9 is employed to govern the transportiveness of results from one iteration to the next. The SIMPLE algorithm is susceptible to divergence unless under-relaxation factors are implemented. These factors control the rate of convergence and are unique to each case study. If chosen too high, the solution will diverge and too low, convergence will be slow and computationally expensive. The challenge is to estimate the most effective values.

Appendix B, Table B.3 displays the information relevant to the solving of each grid. The amount of iterations and the y^+ values is also indicated in this table.

The y^+ values of all the simulations were within acceptable parameters. Furthermore, the simulations all reached the convergence criteria. Convergence was determined based on residual reduction, the convergence of the three velocity components and the local pressure at the monitoring cell (Fig. 2.15).

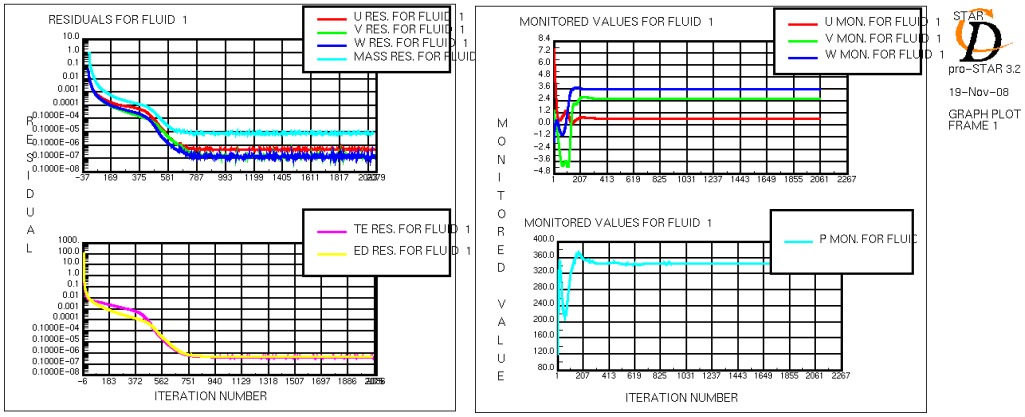

Figure 2.15: Convergence graphs

Grid independence speaks towards the optimum number of cells that is required to obtain accurate results. The amount of cells is constrained by the computational capability of the available equipment. It was determined that less that 1.3 million cells should be used in the final grid. This allows for reasonable accuracy and grid independence whilst not over-extending the computational expense of the simulation. Grid independence is determined by comparing the static pressure profiles of the various meshes as well as the resolution of the turbulent wake. Velocity distribution profiles are extracted from the post-processing data at three different locations:

- at the apex
- directly behind
- 0.15 m (one diameter) behind the hemisphere

The data clearly shows the resolution of the turbulent wake in each case. The grid independence graphs are displayed in Appendix B.

2.4.3 Post Processing

Comparison of Results from Different Turbulence Models

The most important output of the simulation is the static pressure. A comparison of static pressure between the CFD results and the experimental data will give an indication of the accuracy of the computational model. Furthermore, the resolution of the turbulent wake through the use of different turbulence models is investigated. The aim of this section is to discuss the results obtained from the implementation of different turbulence models, convey the turbulent kinetic

properties of the flow simulation and the underlying velocity patterns that emerged as a result.

Static pressure and velocity distribution profiles are obtained from all the simulations for each of the turbulence models implemented. The results are displayed in Figures 2.16-2.19. It should be noted that the relative static pressure is displayed in the profile, the reference pressures will be brought into account in the comparative analysis between the experimental en CFD results.

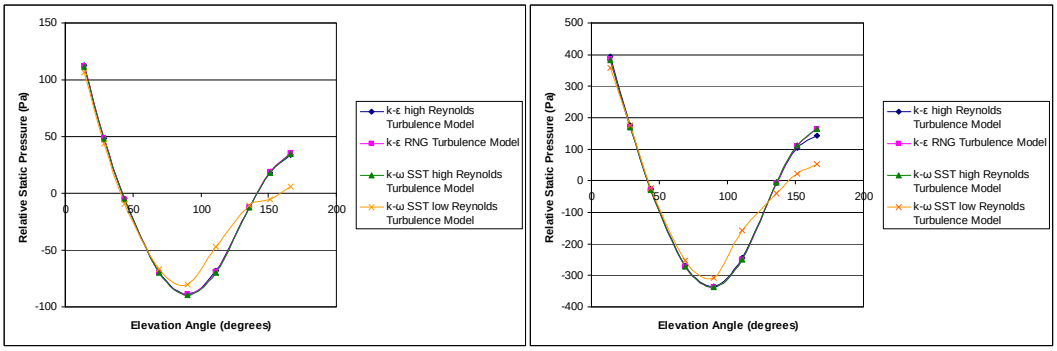

Figure 2.16: Pressure profiles in 10 m/s and 20m/s free stream velocity

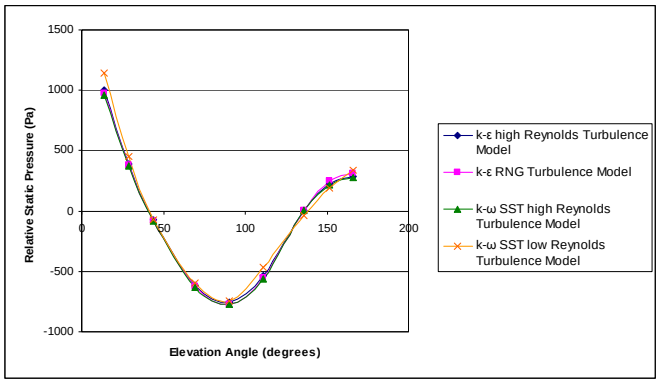

Figure 2.17: Pressure profiles in 30 m/s free stream velocity

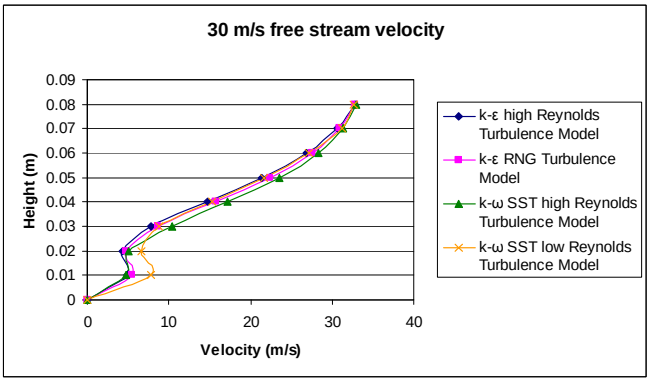

Figure 2.18: Velocity distribution directly behind hemisphere

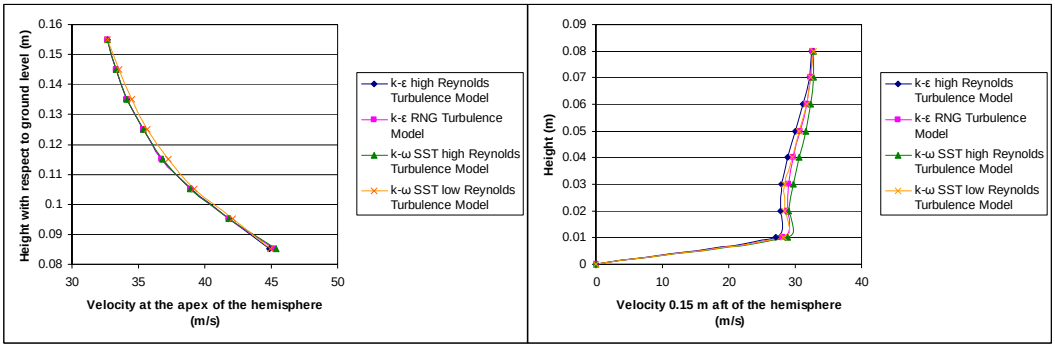

Figure 2.19: Velocity distributions with 30 m/s free stream velocity

There were no discernable differences between the results from the k-ε high Re, k-ε RNG and k-ω SST high Re turbulence models. This is anticipated as it is commonly found in literature that various high Reynolds models give similar results for a specific application. Stamou and Katsiris (2005, 2006) deals specifically with complex airflow and it was noted that "...all three tested turbulent models predict satisfactorily the main qualitative features of the flow…". Yang (2004) examines a naturally ventilated full-scale building and explicitly uses k-ε high Re and k-ε RNG turbulence models. The results of both models prove to be similar and acceptable. These studies dealt mostly with internal flow, yet the wind tunnel experiment is a combination of internal and external flow. Chang and Merony (2001, 2003) investigates the modelling over bluff bodies with specific reference to urban street canyons. Their investigation shows that the variance in results from k-ε high Re and k-ε RNG turbulence models are negligible. It should also be noted that their work only made use of a tetrahedral cells configuration. Anthony and Flynn (2005) models the bluff body effects in the human torso using only the k-ε high Re turbulence model, which provided a reasonable flow field. Their CFD mesh was also generated using tetrahedral cells.

In the current study the results of the k-ω SST low Re turbulence model is compared to the results from the high Reynolds turbulence models. In the cases of 10 m/s and 20 m/s free stream velocity, differences in values behind the apex is observed. This is due to the tendency of high Reynolds models to produce a bit too high turbulence levels in regions with large normal strain. Where the free stream velocity is 30 m/s, smaller differences between the high and low Re turbulence models are apparent. Further implementation of a low Re turbulence model would not be a viable option in this study. This chapter serves as a verification case and the characteristics of the model used in Chapter 3 must be brought into account. Surface roughness is omitted from the equation in order to simplify the experiment. However, the surface roughness of the plant will have a definite effect on the airflow in the field and must be considered. Implementing a low Re turbulence model in conjunction with surface roughness will lead to discontinuities in the model. It is not computationally possible to accommodate a low Re turbulence model wall boundary layer treatment when significant high

amplitude surface roughness exists. The results from the low Re turbulence model are discussed to point out how it differs from the other models and to compare it with the experimental results.

Velocity Patterns

Pressure and velocity are interlinked by the Bernoulli's principle as indicated in Equation 2.23.

$$\frac{V^2}{2} + gh + \frac{P}{\rho} = c \tag{2.23}$$

In order to understand the velocity patterns, pressure must also be investigated. Similar velocity and pressure patterns emerge during the post-processing of the three cases. The magnitudes in each case vary, but the general pattern is comparable with the literature.

An object, in this case the hemisphere, in the path of the flow is an obstruction and causes the flow to decelerate as it reaches the vicinity in front of the object. Mass, momentum and energy must be conserved; therefore the air is directed upwards and slightly sidewards to flow over the object. This causes an increase in velocity in the area of the apex and extends to the sides of the hemisphere. According to Bernoulli's equation an increase in velocity will result in a decrease in pressure. This can clearly be observed in Figure 2.20 and Figure 2.21: the pressure at the near- stagnation point is significantly higher than the pressure at the apex.

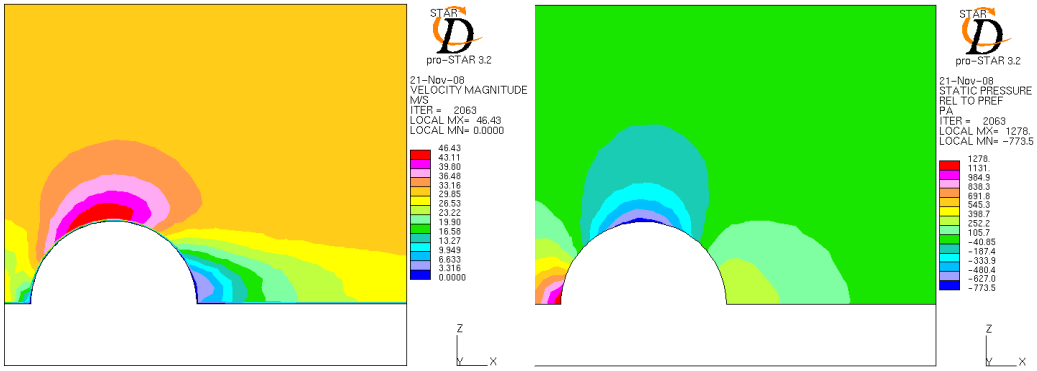

Figure 2.20: Velocity magnitude and static pressure distributions (side view)

It is unlikely that a hemisphere situated on a flat plate will have a definite stagnation point. Directly in front of the hemisphere the flow will already be forced in an upward direction and thus maintain a velocity gradient. The velocity decelerates after the apex, resulting in a steady increase in pressure, thus resulting in an adverse pressure gradient. Velocity vectors (Fig. 2.22) indicate that behind the hemisphere, there is a definite backwards flow. This is observed visually in the wind tunnel (Fig. 2.12) and is an indication of separation. Closer investigation

and the air particle analysis reveal the separation point and the accompanying backwards flow (Fig. 2.23). The separation point appears to be approximately at 110º, which is aligned with the predicted values in the literature. The difference between the predicted separation point for the low and high Reynolds turbulence models will be discussed in Section 2.5.

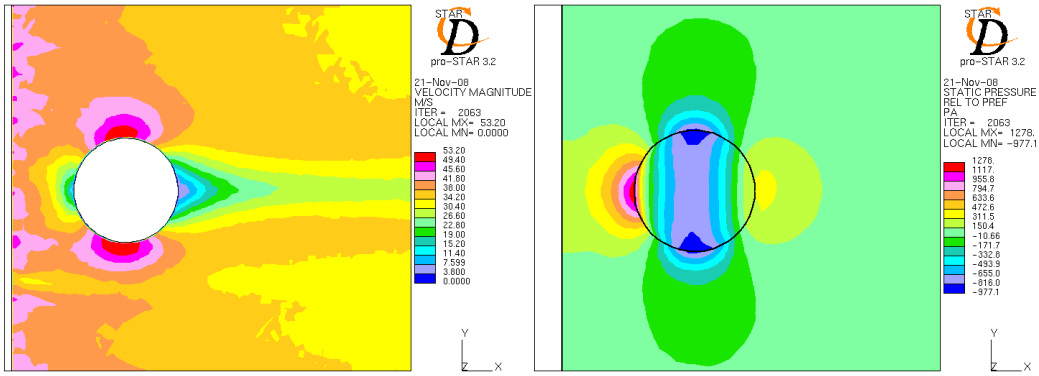

Figure 2.21: Velocity magnitude and static pressure distributions (top view)

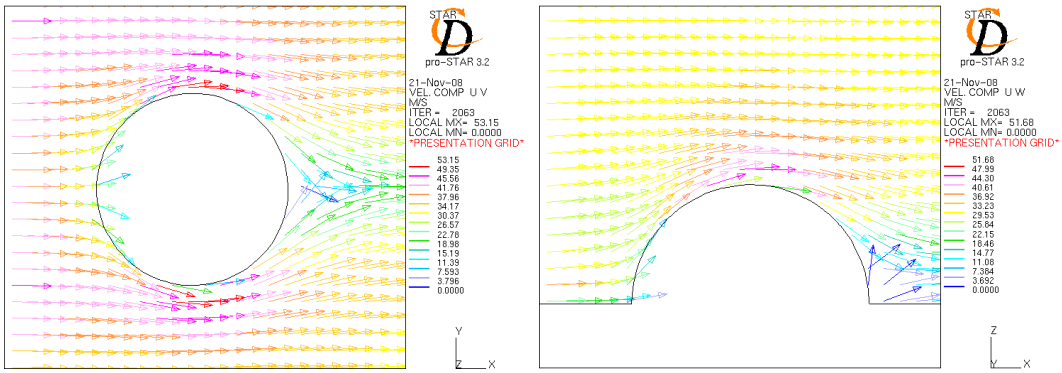

Figure 2.22: Velocity vectors of flow over the hemisphere

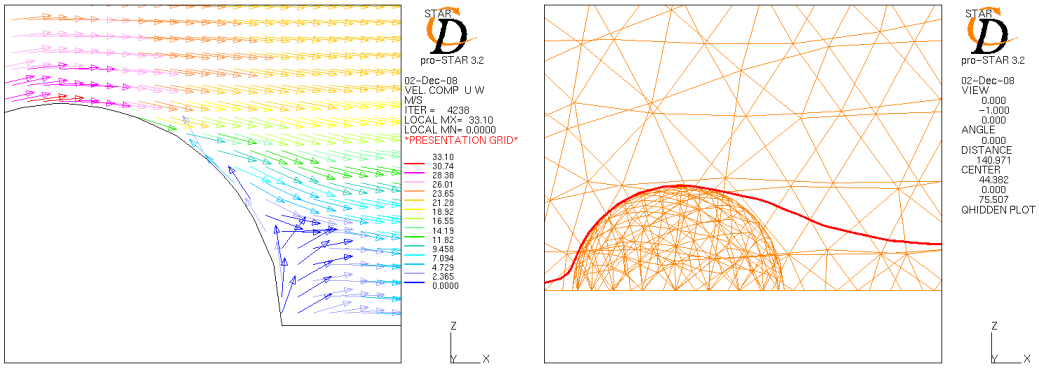

Figure 2.23: Visualization of the separation point

Figure 2.24 shows that flow is obstructed by the presence of the hemisphere, causing lower velocities directly behind the hemisphere. The lower region behind

the object is therefore sheltered from the wind. This phenomenon is used in a Chapter 4 to explain the vibrant growth of *A. magellanica* downwind of the *A.selago* plant. The conservation laws of mass, momentum and energy ensure that the free stream velocity is yet again established as the profile leaves the vicinity of the hemisphere. Figure 2.25 illustrates the previously mentioned increase in velocity as the flow is directed over the apex. As the points progress away from the apex, it is apparent that free stream velocity is restored to the profile.

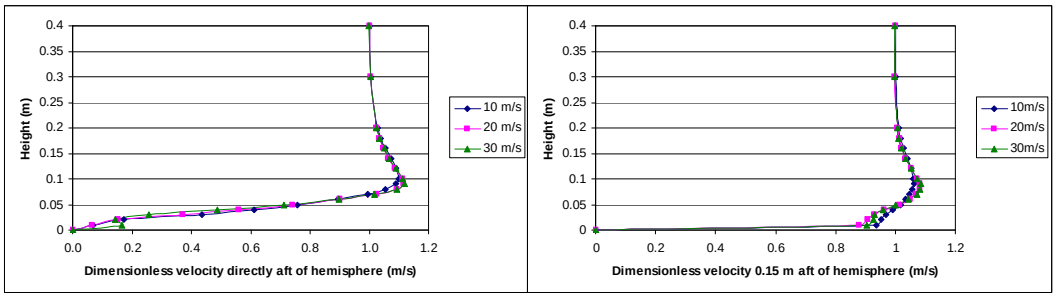

Figure 2.24: Velocity distribution graphs

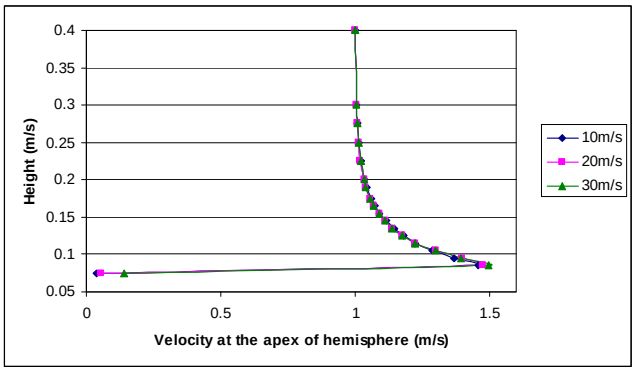

Figure 2.25: Velocity distribution at the apex of the hemisphere

2.5 Comparison between the Experimental and CFD Results

The purpose of this chapter is to investigate the nature of airflow over the hemisphere, as well as to examine the appropriateness of the turbulence model employed and the accuracy of the simulated results. This comparison between experimental and computational results is the benchmark against which the accuracy of subsequent CFD analyses will be measured. The limitations of the numerically obtained results will become apparent in this section.

All the turbulence models implemented in this analysis was two equation models. This was used because the two extra transport equations that represent the

turbulent properties of flow allow account for residual effects such as convection and diffusion of turbulent energy. Every turbulence model calculates these turbulent properties in a different manner. In this lies the strength and weakness of turbulence modelling: the inability for a single model to be applicable to all problems. Every problem is unique and therefore requires a unique turbulence model. The only turbulence model that is truly generally applicable makes use of LES (Large Eddy Simulation). This model is able to accurately simulate the Kolmogorov energy cascade between large and small eddies as well as the independent scaling of these eddies in flow with high turbulence intensity. LES modelling is computationally extremely expensive. The computational requirement of a simulation that implements LES is above the current capacity of the equipment available to the student. Therefore conventional methods will have to suffice.

It is not computationally possible to accommodate a low Re turbulence model wall boundary layer treatment when significant high amplitude surface roughness exists. Therefore a suitable high Re turbulence model had to be selected. Figures 2.16-2.19 and the additional figures in Appendix B clearly indicate that there are no discernable differences between different high turbulence models with applied wall functions. This was the case with the k-ε high Re, k-ε RNG and k-ω SST high Re turbulence models as it is also indicated in the literature (Chang and Merony, 2001, Chang and Merony, 2003, Anthony and Flynn, 2005, Stamou and Katsiris, 2005, Stamou and Katsiris, 2006, Rouaud and Havet, 2002, Yang, 2004). There are a multitude of variations on each on the mentioned turbulence models, but variations are generated for a specific application. The most popular high Reynolds model remains the k-ε high Re model as it is widely used in the industry by the research groups of CSIR, PBMR and Eskom. This is because this model offers a good compromise between generality and economy of use for a wide variety of engineering problems. Turbulence modelling has been called the "Achilles heel" of computational fluid mechanics, as there exists no such thing as a perfect turbulence model. Every model has its advantages and disadvantages. Turbulence modelling will always be a trade-off between accuracy and the availability of computational power.

The numerically and experimentally determined static pressure and pressure coefficient profiles are displayed in Figures 2.26, 2.27 and 2.28. There is an offset error in the static pressure profile between the numerical and experimental data. This is an effect of the reference pressure that was utilized in the simulations and a possible reading error of the mercury level in the barometer. The scaling of the graphs is not a good indicator of the size of the error. This is better depicted in Figure 2.29 where the offset is determined with Equation 2.24. The offset error is less than 0.25%, 0.75% and 1.5% for the 10 m/s, 20 m/s and 30 m/s cases respectively, which is from a blind numerical perspective within acceptable parameters.

$$Offset = \frac{\left| P_{experimental} - P_{numerical} \right|}{P_{experimental}} * 100 \qquad (2.24)$$

The non-dimensional form of the graphs should also be considered – a blind numerical perspective alone will not suffice. It is known that some numerical models over-estimate the turbulence level in regions with large normal strain. This is evident in the lowest value on the graphs where the pronounced velocity gradient results in a too low pressure region, forcing the pressure coefficient to almost -1.5. The experimentally determined value for this is approximately -1. This effect is further evident in the near stagnation region where the pressure coefficients of the numerical data surpass the experimental data. The onset of the adverse pressure gradient is at an elevation angle of 90º for the numerical case, while the experimental data en graphs from the literature indicates that it should occur earlier. This could lead to a delay in separation, of which the extent is shown in Figure 2.30. The separation point in the low Re turbulence model case is at approximately 110º and the particle is immediately deflected away from the hemisphere. The high Re turbulence model places this point at approximately 130º and it can be seen that the particle lingers in the vicinity of the hemisphere curvature.

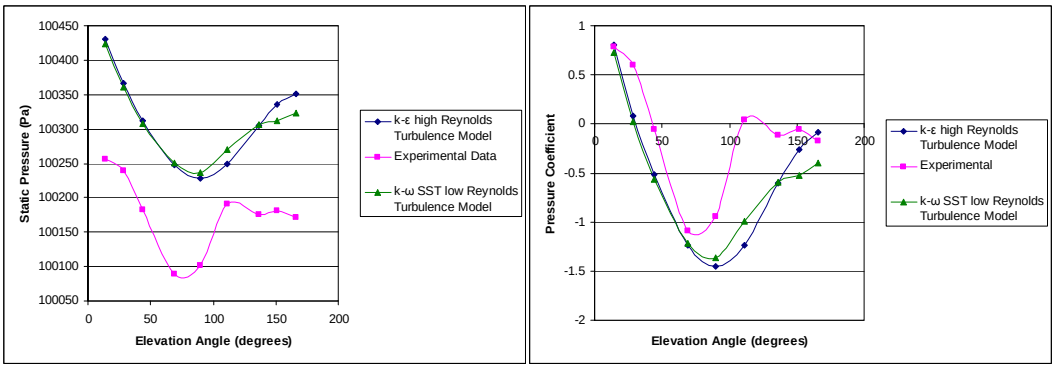

Figure 2.26: Pressure profiles for 10 m/s free stream velocity

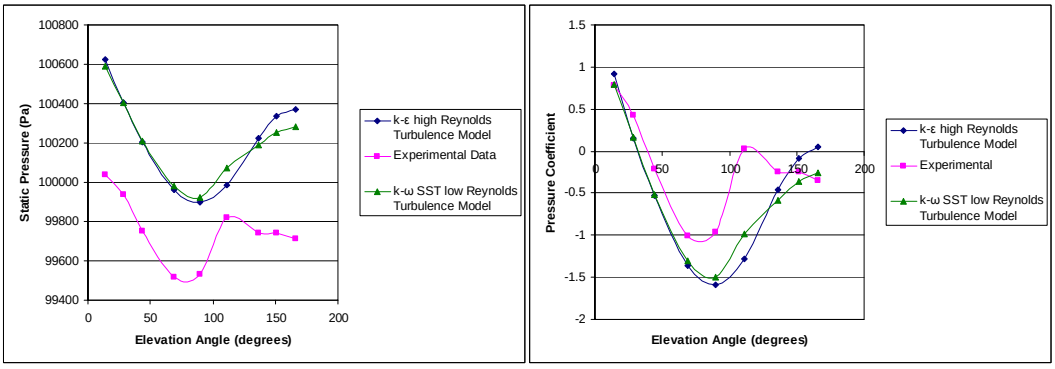

Figure 2.27: Pressure profiles for 20 m/s free stream velocity

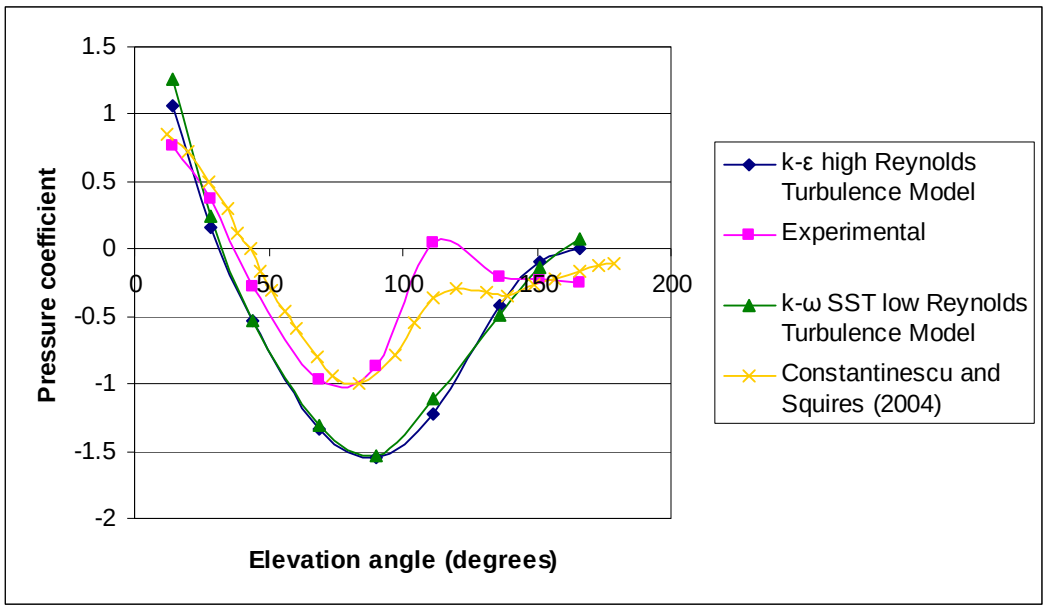

Figure 2.28: Pressure profiles for 30 m/s free stream velocity

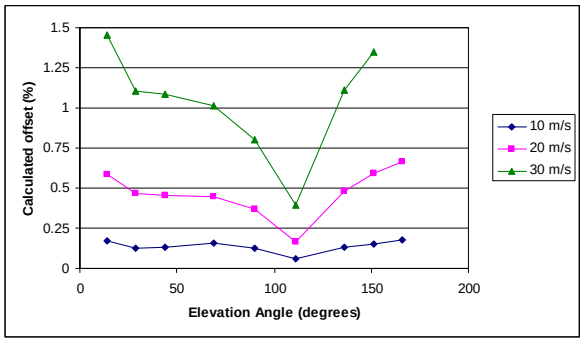

Figure 2.29: Offset error between the numerical and experimental data

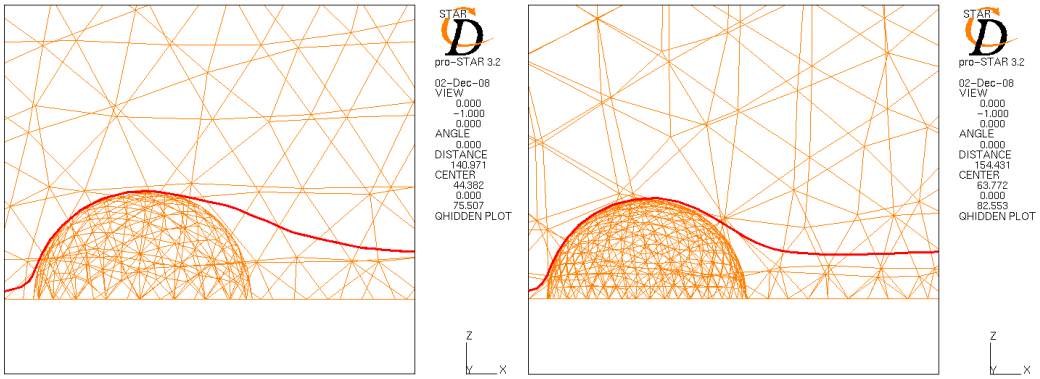

Figure 2.30: Separation points for the low and high turbulence models respectively

2.6 Summary

In Chapter 2 four main themes were discussed:

- Literature on turbulent flow over spheres
- A wind tunnel experiment concerning the basic flow over a hemisphere
- The numerical analysis of the wind tunnel experiment
- A comparison between the experimental and numerical data

The aim of the literature study was to gain knowledge on a topic of considerable complexity. Perić is considered one of the leading CFD researchers in Germany. Through his research the various regimes of flow over a sphere came to light. The work of Constantinescu and Squires (2004) proved to be very insightful.

The results from the wind tunnel experiments compared well with what was expected after the literary study. The onset of the adverse pressure gradient occurred before 90º, which further correlates with the literature. Additional experiments using oil and power paint was extremely useful in determining the separation point and visualizing the backwards flow at the leeward section of the hemisphere. The sixth point (at approximately 111º) had displayed a slightly too high value and the relevant pressure coefficient for that point was above 0. This was however within acceptable error parameters. A comparison of Figures 2.11 and 2.26 to 2.28 suggests that the regimes tested are indeed supercritical, since the pressure coefficient characteristically reached values less than -1.

The numerical study was conducted utilizing four independent turbulence models: k-ε high Re, k-ε RNG, k-ω SST high Re turbulence models and the k-ω SST low Re turbulence. There were negligible differences between the results of the various high Re turbulence models. This was indicated through comparison of static pressure and velocity distribution profiles. The inappropriateness of the further implementation of a low Reynolds turbulence models was discussed. The work of Constantinescu and Squires (2004) suggests that a detached eddy simulation (DES) would improve the accuracy of the pressure coefficient prediction. However, the implementation of such a model through the StarCD V. 3.24 code used would have exceeded the computational resources available to the project. It was therefore decided that the k-ε high Re turbulence model will be used as a compromise between generality and economy of use. While not quantitatively accurate, it is suggested that this turbulence modelling approach will nevertheless yield useful insight into the flow regime around the *Azorella selago* plant.

Chapter 3 – The Effect of Plant Shape and Size on Airflow

3.1 Introduction

It was previously established that the shape of *A. selago* follows a natural evolution as it reaches maturity; the plant is most commonly hemispheroidal, but may be hemi-ellipsoidal, or in rare cases be crescent shaped (lunate). Nine plants of different dimensions and varying shapes were specified by the ecologists involved in the BioGeo project. The analysis in Chapter 2 was limited to the most basic shape of the plant, while in Chapter 3 the effect of different shapes and sizes on the flow of air is examined. Comparison between the simulations and experimental data indicates that the methodology used to conduct the analysis is accurate to an acceptable degree in the context of the k-ε high Re turbulence model. Shortcomings of the method were identified before further implementing it. Chapter 3 is therefore an expansion of the work conducted in Chapter 2.

In the previous analysis the velocity inlet profile was derived from experimental data. The subsequent analyses utilises a logarithmic inlet velocity profile to the computational domain. The appropriateness of this profile was tested during an expedition to the island. In Chapter 2 the surface roughness of the surroundings and the plant were not considered in the simulation. In order to make the analysis in Chapter 3 as realistic as possible, texture of the plant and its surroundings is quantified. The different cases are analysed by visualization of the velocity flow field around the plant. Distinct patterns emerge because of variation in the shape and dimensions of the plant. Air particle tracks are displayed for each shape. This method is a superb tool that aids in the visualisation of the flow field. The pressure fields will be considered in Chapter 5 in conjunction with the force analyses.

3.2 Wind Velocity Profile on Marion Island

3.2.1 Theory

The simulations in Chapter 2 were done with an experimentally determined inlet velocity profile. In the literature the atmospheric airflow profile is estimated to be of a logarithmic nature. The power law approximation (Petersen et al, 1998) can be used but it was not considered for this study due to the variability of the power value (Eq. 3.1). This value varies with height, surface roughness and stability of

the velocity profile. A more appropriate equation is the logarithmic velocity wind profile (Eq. 3.2).

$$\frac{u(z_1)}{u(z_2)} = \left(\frac{z_1}{z_2}\right)^p \tag{3.1}$$

$$u(z) = \frac{u^*}{\kappa}[\ln\left(\frac{z}{z_o}\right) - \psi] \tag{3.2}$$

In this equation u^* is the friction velocity, κ is the von Kármán constant and z_0 the roughness length. The symbol ψ represents a stability dependant function that is positive in unstable conditions, negative in stable conditions and zero for neutral stability (Petersen *et al*, 1998, Weber, 1999, Kim and Baik, 2003, Yang *et al*, 2008). This equation is derived from turbulent boundary layer theory and thus relates strong to the logarithmic velocity distribution layer (Eq. 2.21). In order to derive the u^* and z_o of Equation 3.2 experimentally, assume neutral stability. The equation can then be linearised in the following manner:

$$\begin{aligned} z &= b\,m^u \\ \ln z &= \ln(b\,m^u) \\ \ln z &= u \ln m + \ln b \end{aligned} \tag{3.3}$$

This form can be recognised as a straight line by substituting $\ln z$ with y, u with x, $\ln m$ with n and $\ln b$ with c.

$$y = n\,x + c \tag{3.4}$$

Ideally three or more experimental points are required to obtain accurate results. This method is employed in Section 3.2.2 to investigate the appropriateness of the logarithmic profile in atmospheric airflow. A question arises concerning the viscous sublayer in the atmospheric boundary layer: Why do most atmospheric boundary layer studies not include the viscous sublayer in the velocity distribution profile? The viscous sublayer makes up less than 1% of the turbulent boundary layer; it is so small that logarithmic scaling is required to make the results visible on a graph and is therefore considered negligible in studies relating atmospheric airflow. In this study the thickness of the viscous sublayer will be determined through experimentation to decide whether it is negligible.

3.2.2 Measured Profiles

The yearly take-over expedition to Marion Island takes place during the fall. In April 2008 the student was granted the opportunity to join the excursion. During

this time low-level velocity profiles were measured at various locations on the island. The equipment used included a 1.5 m mast, three WSD100 anemometers and a XR5SE data logger. The specialist apparatus was obtained from *Pace Scientific Dataloggers and Sensors*. The WSD100 can measure velocities from 0 to 78 m/s with ±5 % accuracy and direction from 0 to 360° with ±7 % accuracy. The XR5SE data logger has an accuracy of ±0.25 % full scale on all velocity inputs. Figure 3.1 shows the equipment positioned behind Marion Base during initial stages of wind profiling on the island.

Figure 3.1: Wind profiling near the base on Marion Island

Profiles were taken at four different locations: Base, Skua-Ridge, Tafelberg and Mixed Pickle. Only the data obtained from Skua-Ridge and Tafelberg were used because *A. selago* are more commonly found in these areas. The plant is found in the mires near Base and Mixed Pickle, but not in abundance or good physical condition. Three vertical positions were simultaneously measured; ideally more positions should be monitored. However, financial constraints did not allow it. Three datasets were collected at each location on different days and under dissimilar environmental conditions. The average at each vertical position for a specific dataset was used to obtain the experimental profiles. The data is displayed in Table D.1.

The averaged data in Table D.1 was used in the linearised form of Equation 3.2 to obtain the u^* and z_o values. The regression coefficient (R^2) in each case is an indication of how well the data conforms to the logarithmic profile. The lowest value was found in Skua-Ridge dataset 3 and the best fitting was Skua-Ridge dataset 2. Ideally R^2 should have a value of 1; Figure 3.2 depicts the profiles with the highest and lowest R^2 values. Table D.2 reports the linearization data for the velocity measurements. It can clearly be seen that assuming a logarithmic inlet

velocity profile is appropriate. The regression coefficients are all acceptable and the thickness of the viscous sublayer (δ') is negligible.

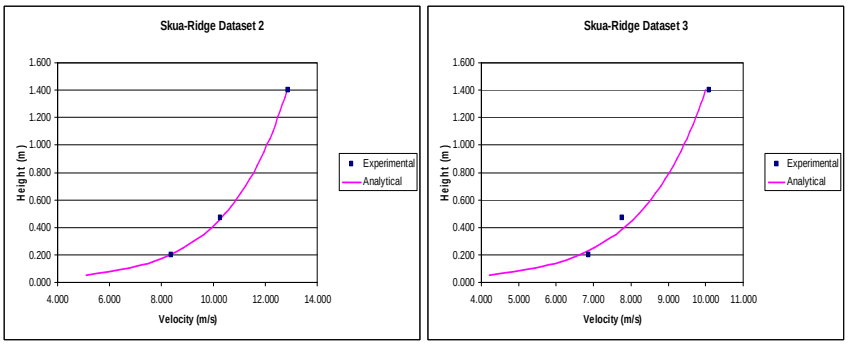

Figure 3.2: Skua-Ridge logarithmic velocity profiles

3.2.3 Surface Roughness

The default model for surface roughness in the commercial computational fluid dynamics program StarCD version 3.24 is based on the sand grain experiments of Nikuradse (Schlichting, 1968). The following modified Law-of-the-Wall equation is used when dealing with fully rough walls at high Reynolds numbers:

$$u^+ = A + \frac{1}{\kappa}\ln\left[\frac{y^+ - D^+}{B + C\,R^+}\right]$$

where

$$D^+ = \rho C_\mu^{\,0.25} k^{0.5} \frac{D}{\mu} \qquad (3.5)$$

$$R^+ = \rho C_\mu^{\,0.25} k^{0.5} \frac{y_o}{\mu}$$

Nikuradse's work indicated that generic values for A, B, C and D are 8.5, 0, 1 and 0 respectively. The value y_o represents the roughness height. Determining an appropriate value for the ground surface roughness proved to be a difficult task. Both Skua-Ridge and Tafelberg are grey lava areas where smooth basalt rocks can be found in various shapes and sizes. Figure 3.3 shows A. selago and its surroundings on Skua-Ridge.

The sediment size in the immediate surface area around the plant also displays a high degree of variation; this can clearly be seen in Figure 3.4. In the one case there is a distinct difference in sediment size between the north and south side of the plant (note that the arrow points to true north). The northern side sediment is significantly smaller than the pebbles on the southern side. In the other case there is no obvious change in sediment size. A sediment size analysis done by the

Department of Ecology and Entomology at the Stellenbosch University indicated that the sizes vary from 2 mm to 313.24 mm. The average of the analysis, 5.7 mm, was used in the simulation as the y_o value representing the ground surface roughness. The surface roughness of the plant was taken as 1.5 mm. Default values for A, B, C, and D were used.

Figure 3.3: *Azorella selago* and surroundings on Skua-Ridge

Figure 3.4: Rock distribution and rock size around *Azorella selago*

3.2.4 Simulated Profile

It was determined in section 3.2.2 that using a logarithmic profile is appropriate when simulating atmospheric airflow. According to data from the meteorology station on Marion Island the mean annual wind speed fluctuates around 8 m/s (Fig. 3.5). A profile was therefore chosen that slowly approaches a reference velocity of 8 m/s (Fig. 3.6). Equation 3.6 was used in all subsequent simulations.

$$u(z) = \frac{0.138}{0.4}[\ln(\frac{z}{0.0057}) - (-18)] \qquad (3.6)$$

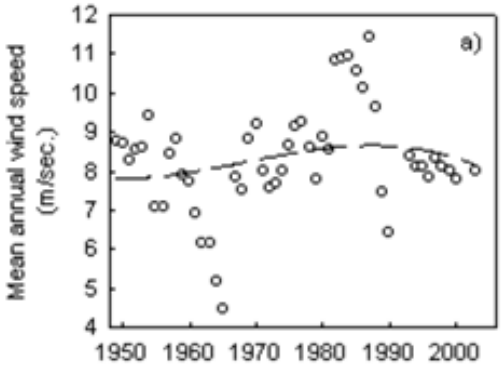

Figure 3.5: Mean annual wind speed for Marion Island
(Le Roux and McGeoch, 2007)

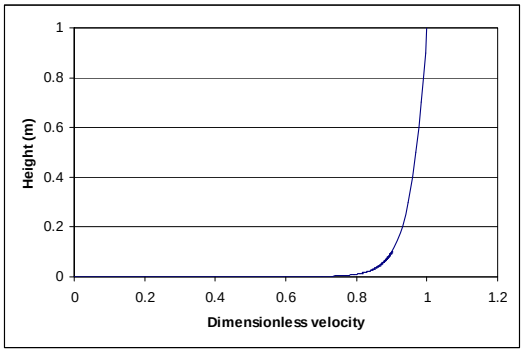

Figure 3.6: Simulated dimensionless velocity profile (reference 8 m/s)

3.3 Pre-Processing

Nine plant sizes have been identified; four sizes hemispheroidal, three sizes ellipsoidal and two sizes crescent shape (lunate). Table D.3 reports the dimensions of the nine plants, the control volumes and the position of the plant centre point in the control volume. Comprehensive grid generation data is contained in Appendix D. Three models of increasing number of cells are generated for each of the nine sizes, therefore a total of twenty-seven grids are created to answer research question two. Tetrahedral cells are implemented in all the grids.

Seven boundaries are created for each grid; an inlet, an outlet, three symmetry planes, and two wall boundaries. The first wall boundary is the surface of the plant and the other is the ground surrounding the plant. The default model for surface roughness is used with roughness heights of 1.5 mm and 5.7 mm for the plant and the surroundings respectively. The left, right and upper boundaries of the control volume are defined as symmetry planes. The remaining two sides are defined as the inlet and the outlet of the model.

Standard molecular properties for air are utilized. The micro-climate surrounding the plant is not under investigation in this project, therefore no thermal model is employed. A numerical monitoring cell is selected behind the plant where the most change in parameters occurs. The reference cell is placed at a height of 1 m in the middle of the control volume at the inlet boundary. A reference pressure of 100 000 Pa and a temperature of 6.5 °C (Fig. 3.7) is assumed. Take note that the monitoring cell and the reference cell are not the same. The purpose of the monitoring cell is to determine whether convergence of the residuals have been achieved locally. The purpose of the reference cell is to provide a known temperature and pressure at a specific point in the mesh as a reference for the relative pressure field emerging from the Navier-Stokes equation.

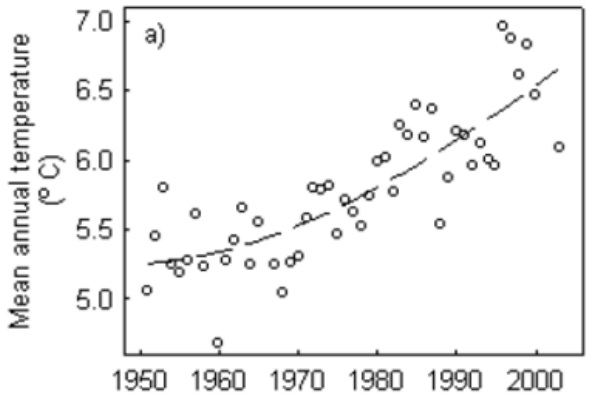

Figure 3.7: Mean temperatures for Marion Island (Le Roux and McGeoch, 2007)

In accordance with the research discussed in Chapter 2, the k-ε high Re turbulence model is used in all the models. Since no actual measurements regarding the turbulence properties of the airflow on Marion Island were taken during the expedition, it was decided that arbitrary values will be chosen to represent the turbulence intensity.

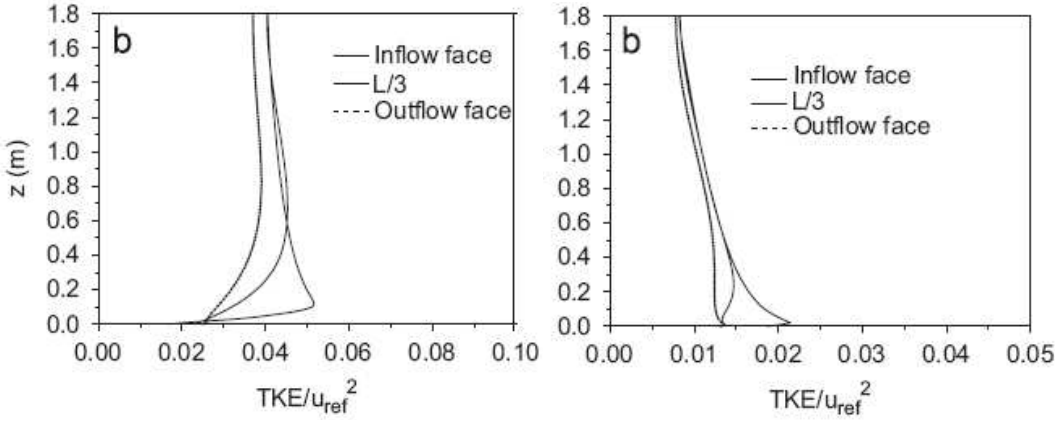

Figure 3.8: Dimensionless turbulent kinetic energy profiles (Yang *et al*, 2008)

Yang *et al.* (2008) investigated the influences of the equilibrium atmosphere boundary layer and turbulence parameters (Fig. 3.8) on wind loads of low-rise buildings and serves as a reference study for these unknown properties. Turbulence kinetic energy graphs reveal relatively constant profiles. Furthermore, a turbulence factor that is significantly smaller than the factor for low-rise buildings can be expected on the island, since it is not an urban environment. Subsequently an inlet free stream turbulence of 4 % is specified and the mixing length is identified as the height of the plant for each model.

3.3 Solving

The simulations are solved in the steady state domain with single precision. The flow is defined to be incompressible. The AMG solution method is employed in conjunction with the SIMPLE solution algorithm. Central differencing with a blending factor of 0.9 is implemented. Satisfactory convergence is reached for all 27 simulations. Appendix D reports the relaxation factors for momentum, pressure, turbulent viscosity and viscosity as well as the number of iterations and y^+ values. Grid independent solutions are obtained and the results are displayed in Appendix E.

It will be noted in appendix D that the y^+ values for the crescent shape are not in between 30 and 300 as is required by the k-ε high Re turbulence model. Figure 3.9 shows the y^+ values for the large crescent shape. It can be observed that the areas that are not within specification are very small. These areas of discrepancy are due to the geometrical parameters of the crescent shape. Further enlargements of the boundary layer cells will result in severe breaching of the upper limit y^+ values. However, since the area of difference is so small, it will not result in significant error.

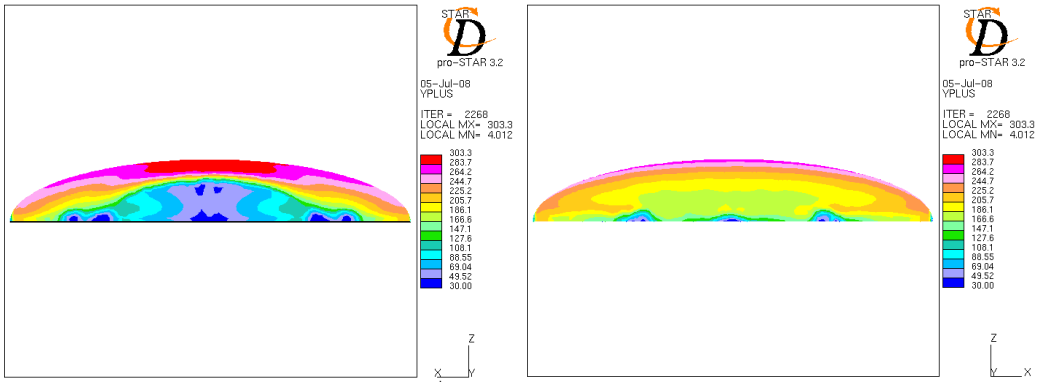

Figure 3.9: Large crescent y^+ values for the leeward and windward sides

3.5 Post-Processing

3.5.1 Shape Differentials

Medium Hemisphere Shape

Investigation of the velocity magnitude reveals a leeward pattern that is different from the basic case in Chapter 2. The windward patterns remain similar. Figure 3.10 and Figure 3.11 display the velocity magnitude plots at various levels with relation to the ground level. All plots indicate a symmetrical pattern; this was expected due to the symmetrical shape of the plant.

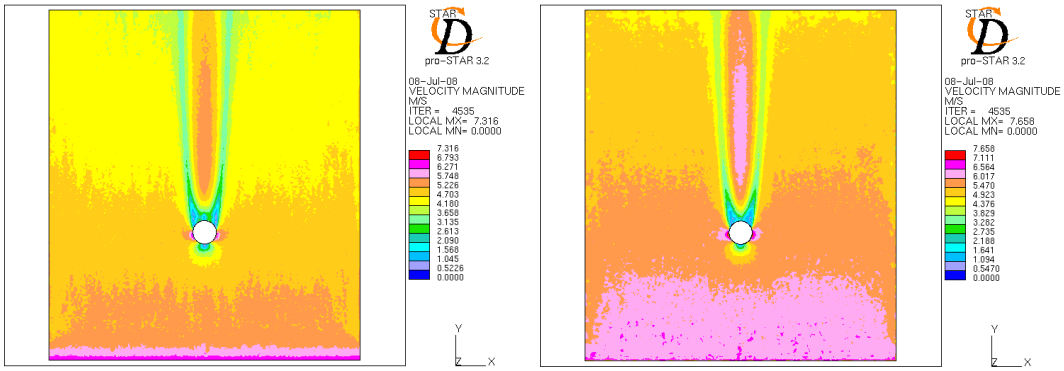

Figure 3.10: Velocity magnitude at planes 7.5 mm and 24 mm from ground level

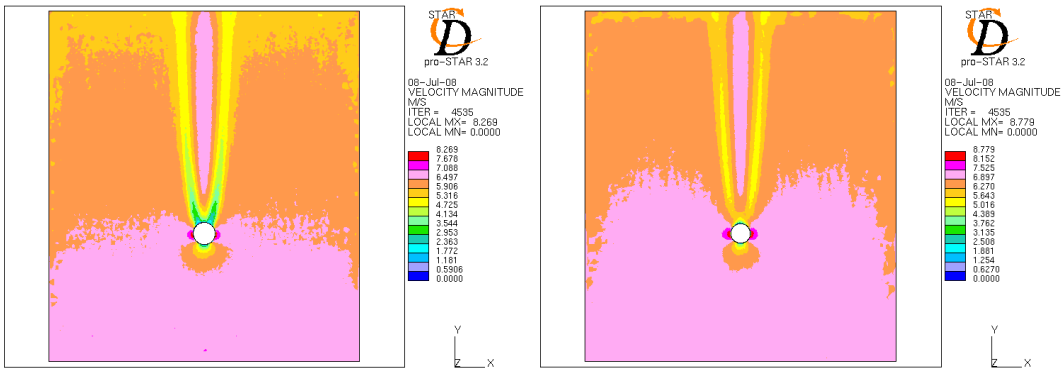

Figure 3.11: Velocity magnitude at 49.5 mm and 82.5 mm from ground level

In front of the hemisphere the flow slows down. The object downstream is an obstruction to the flow; it prohibits the air particles from maintaining current speed and direction. The air is forced around the sides and over the top of the hemisphere, resulting in an increase in velocity. At the leeward side the flow forms two trailing lines of decreased speed with a line of higher speed in between. It must be noted that the general velocity around the plant increases logarithmically with height. This is due to the logarithmic inlet velocity.

A comparison between different side planes in Figure 3.12 reveals a distinct difference in velocity magnitude behind the plant. There is a large area of low velocity behind the plant at the 108 mm plane which is not present at the midplane. Since the laws of conservation for mass, momentum and energy apply, this low velocity area is an indication of the presence of circulation vortices. In this case the pattern that emerges is known as the *horseshoe vortex*. The two trailing lines behind the hemisphere is an indication of the extent of this vortex pattern. Figures 3.13 - 3.16 are vector plots that present the nature of this pattern.

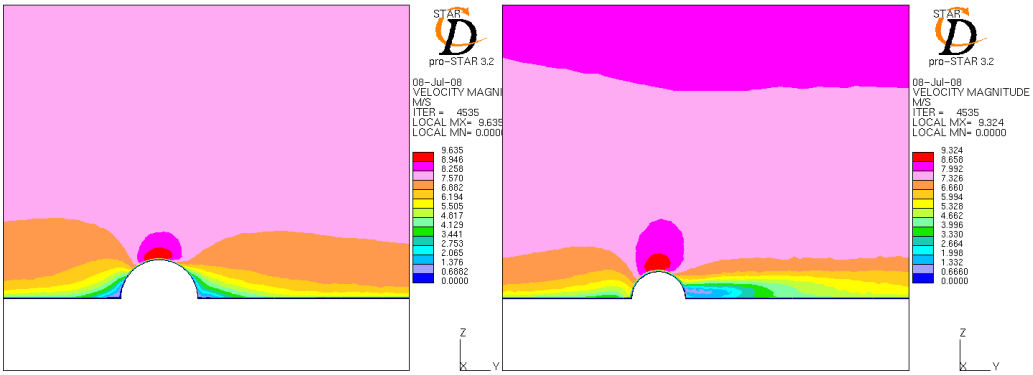

Figure 3.12: Velocity magnitude at the mid section and 108 mm from mid section

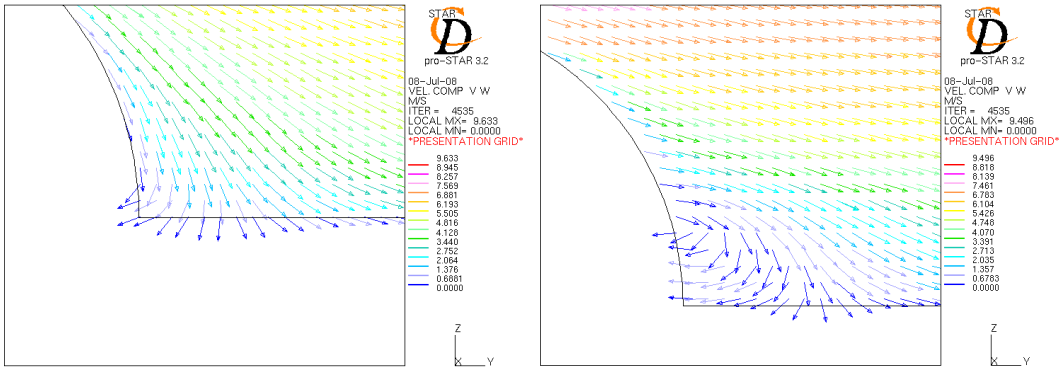

Figure 3.13: Velocity vectors at mid section and 64 mm from mid section

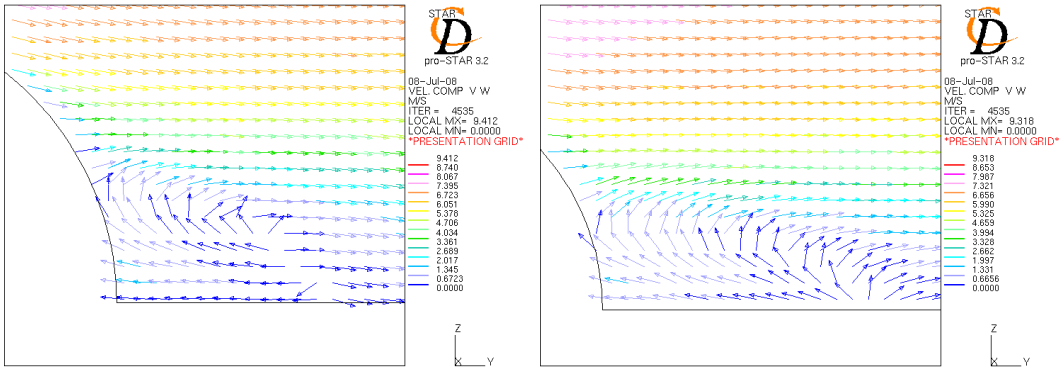

Figure 3.14: Velocity vectors planes at 88 mm and 108 mm from mid section

Recirculation at the midplane is minor to the point of non-existence, since reattachment of the flow is very close to the object. The 64 mm plane shows a more pronounced pattern of recirculation and the point of reattachment is further away form the hemisphere. The recirculation areas of the 88 mm and 108 mm planes are ever more prominent with the reattachment points progressively further away from the object. The horizontal plane plots shows how the pattern is well-defined closer to the ground and diminishes progressively with height.

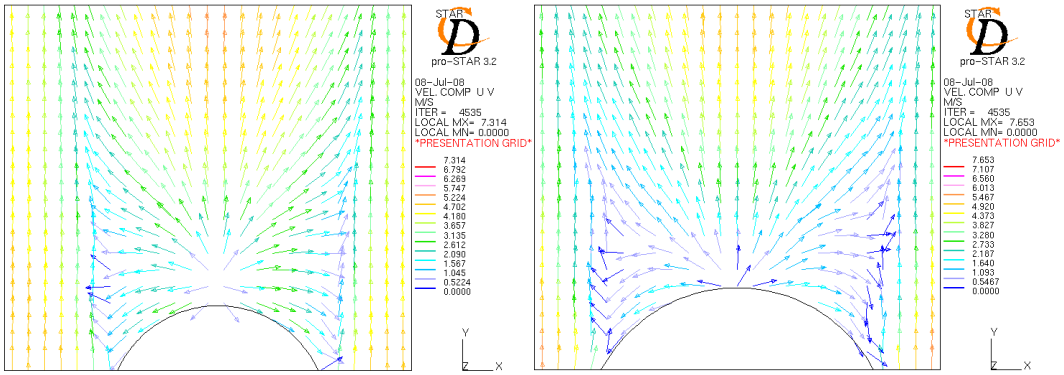

Figure 3.15: Velocity vectors at planes 7.5 mm and 24 mm from ground level

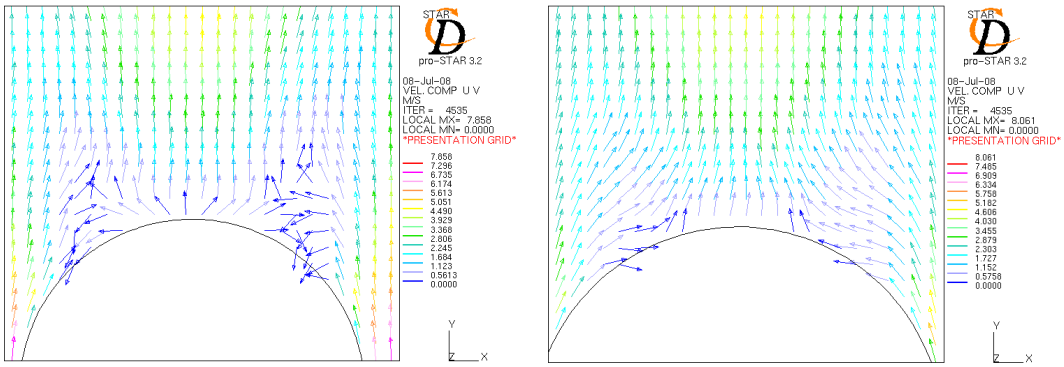

Figure 3.16: Velocity vectors at planes 33 mm and 40.5 mm from ground level

Large Ellipsoidal Shape

The velocity magnitude pattern for the ellipse is similar to the hemisphere pattern on the windward side, but distinctly different on the leeward side. In front of the object the flow decreases in speed; the ellipse prevents the air particles from maintaining speed and current direction. The particles are forced to deflect over the top and along the sides of the ellipse, resulting in an increase in speed. Unlike the hemisphere the ellipse does not form two trailing lines downwind. Only one low velocity tail forms. This can be seen in Figures 3.17-3.18. The pattern is symmetrical due to the symmetrical nature of the plant shape. It is again observed that the general velocity increases logarithmically with height. The midplane side view is distinctly different from the 264 mm plane; a large low velocity region is

observed in the midplane (Fig. 3.19). The recirculation will be more distinct in the low velocity region of the midplane than in the 246 mm plane.

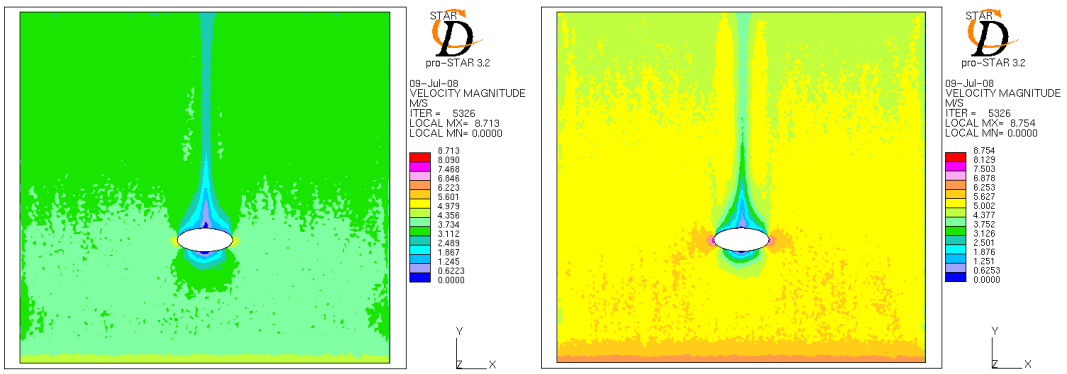

Figure 3.17: Velocity magnitude at planes 5 mm and 11 mm from ground level

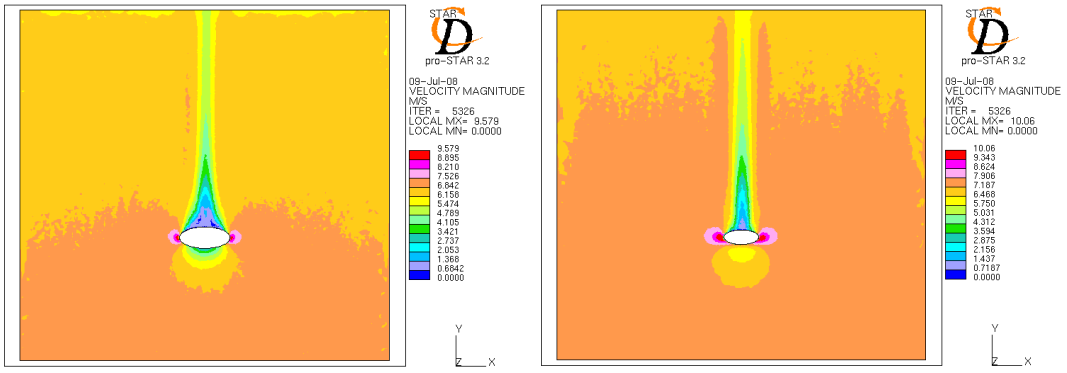

Figure 3.18: Velocity magnitude at planes 77 mm and 148 mm from ground level

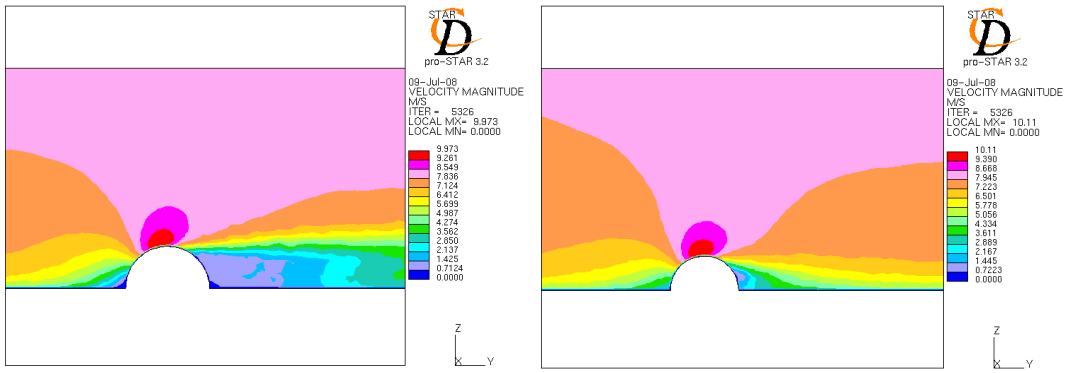

Figure 3.19: Velocity magnitude at mid section and 264 mm from mid section

The recirculation patterns downstream of the ellipse are different from the patterns observed behind the hemisphere. The point of reattachment of the hemisphere moved further away from the object as the plane distance from the midplane increased. The opposite occurs with the ellipse. Figure 3.21 and Figure 3.23

shows that the point of reattachment is far from the object at the midplane, this distance decreases as the plane distance increases. The reason for this becomes clear in Figure 3.20 as the triangular pattern at the horizontal plane is observed.

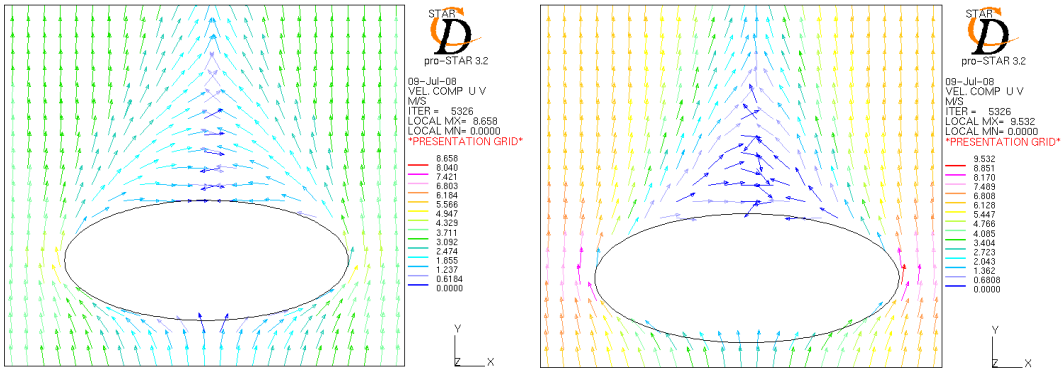

Figure 3.20: Velocity vectors at planes 5 mm and 66 mm from ground level

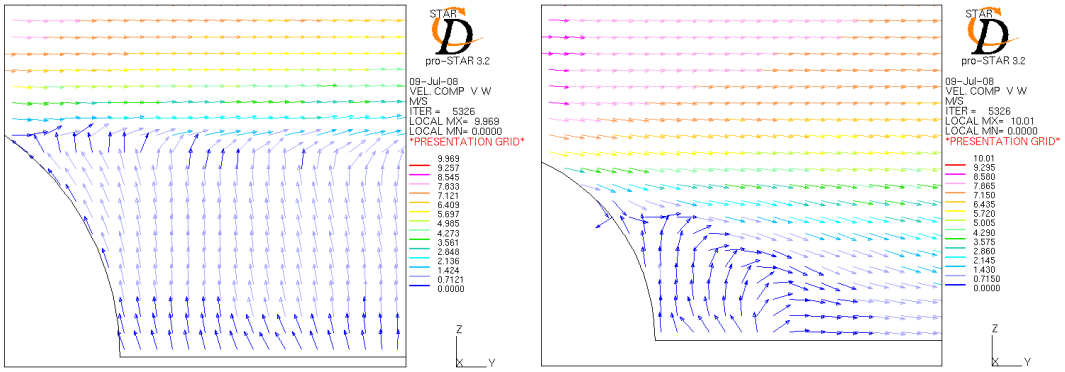

Figure 3.21: Velocity vectors at mid section and 96 mm from mid section

Recirculation is more pronounced at the midplane and become less distinctive as the planes are removed further from the midplane. Velocity vectors in Figure 3.22 indicate how this pattern is diminished by the drive of the free stream with both height and distance.

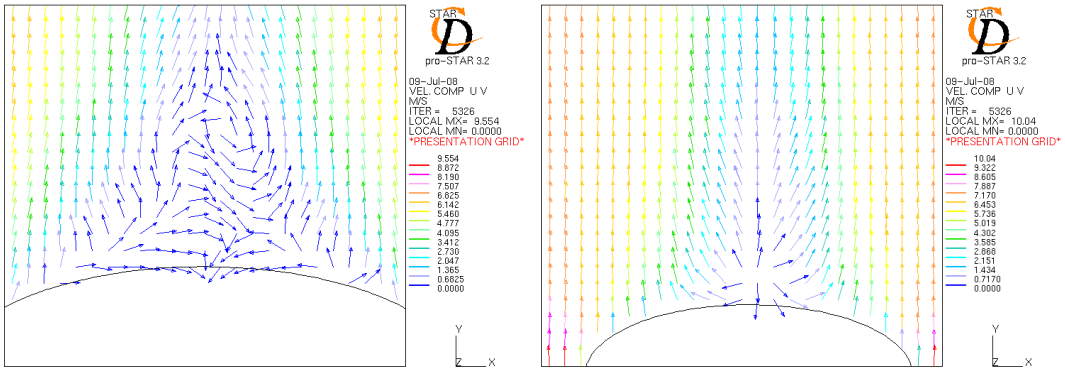

Figure 3.22: Velocity vectors at planes 77 mm and 148 mm from ground level

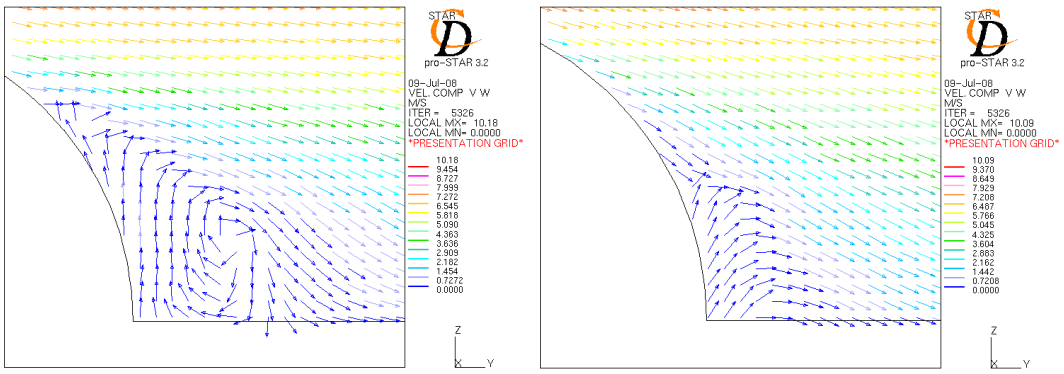

Figure 3.23: Velocity vectors at planes 162 mm and 264 mm from mid section

Large Crescent Shape

Figures 3.24-3.26 displays the velocity magnitude surrounding the plant.

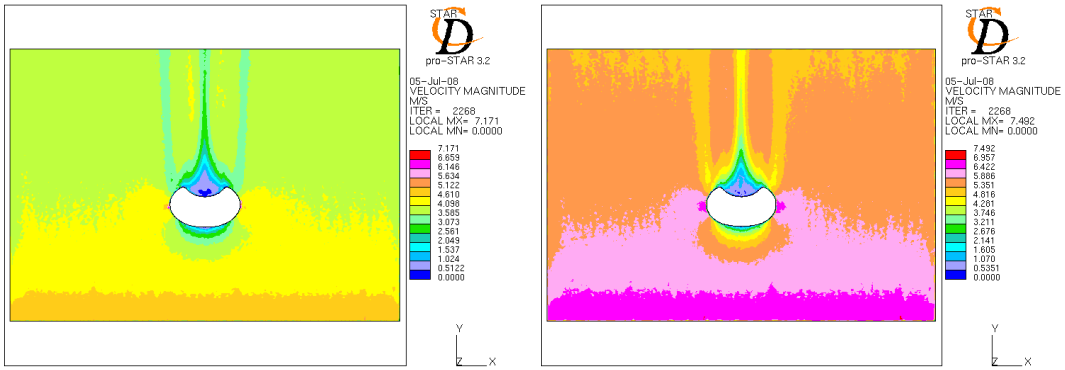

Figure 3.24: Velocity magnitude at planes 11 mm and 16 mm from ground level

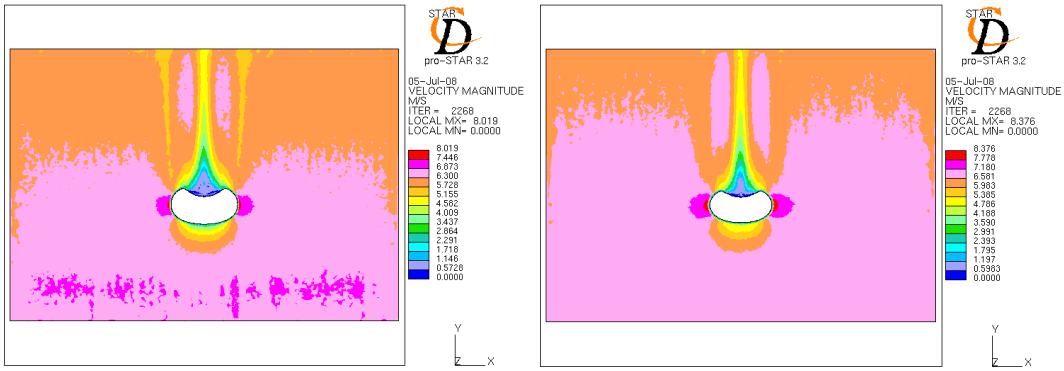

Figure 3.25: Velocity magnitude at planes 33 mm and 55 mm from ground level

Similar to the hemisphere and elliptical shapes, the windward side of the crescent shape displays typical velocity magnitude patterns. Directly in front of the object the velocity slows down due to the obstruction of the flow. On the side and on top

of the object the flow speeds up to satisfy conservation of mass, momentum and energy laws. On the leeward side the flow shows three trailing lines, with the middle one more pronounced. The two outer trailing lines diminish as the height of the plane relative to the ground increases, while the mid-trailing line remains distinctive. The low velocity area directly behind the plant decreases as the height of the plane increases. This is due to the effect of the free stream velocity that drives the flow over the plant. The general velocity increases with height, this is due to the logarithmic velocity inlet profile.

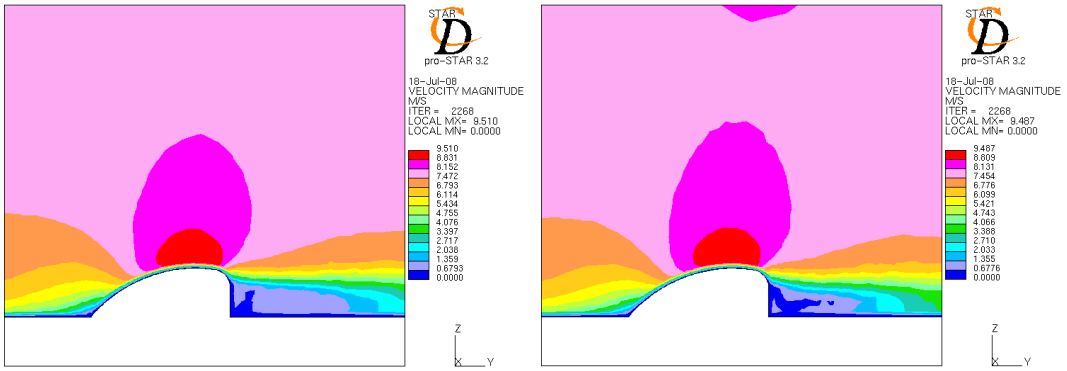

Figure 3.26: Velocity magnitude plots at mid section and 55 mm from section

The crescent shape displayed by far the most interesting velocity vector patterns. The plane 11 mm from the ground level (Fig. 3.27) shows a triangular pattern on the leeward side. This is clarified by Figure 3.29 and Figure 3.30 where it can be seen that the position of the reattachment point moves closer to the object as the plane moves away from the midplane. This is further supported by Figure 3.26 showing that the region of low velocity decreases as the plane distance from the midplane increases.

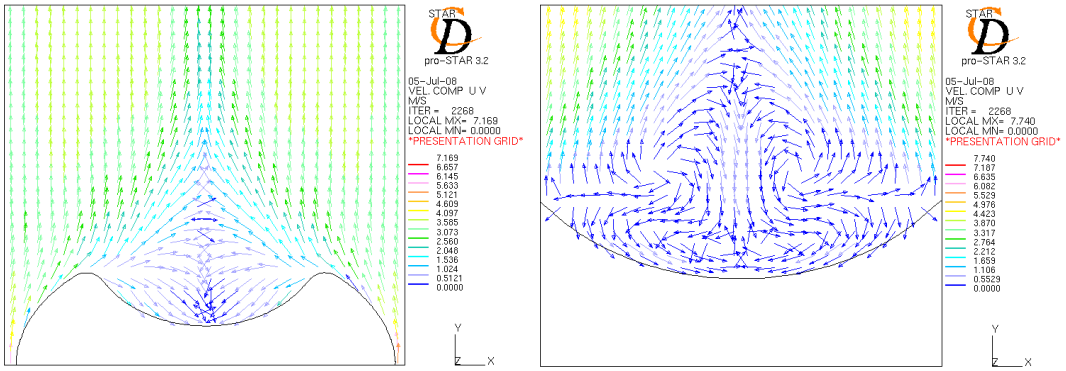

Figure 3.27: Velocity vectors at planes 11 mm and 22 mm from ground level

In Figures 3.27-3.30 the nature of the complex recirculation patterns is investigated. At ground level the flow is directed around the crescent and pulled into the recirculation zone. From there it is directed upwards, the path of the air

particle depends on its position in the flow field. It is observed that in all instances the emerging patterns are symmetrical. This is again due to the symmetrical nature of the plant. The complex vortices that form behind the plant reiterate that these are three-dimensional problems and can not be accurately simulated by utilizing a two-dimensional approach.

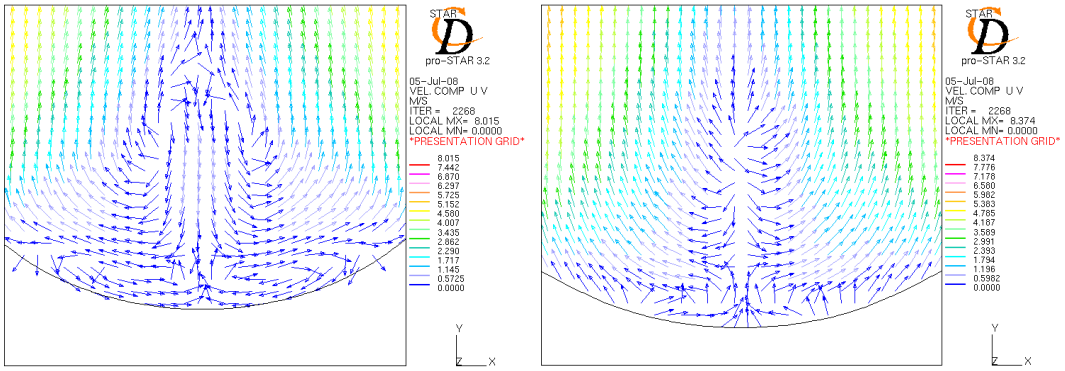

Figure 3.28: Velocity vectors at planes 33 mm and 55 mm from ground level

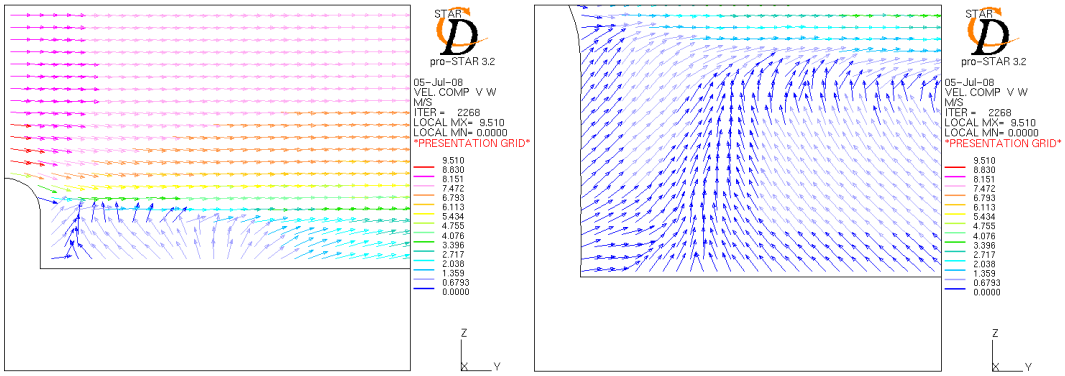

Figure 3.29: Velocity vectors at the crescent mid section

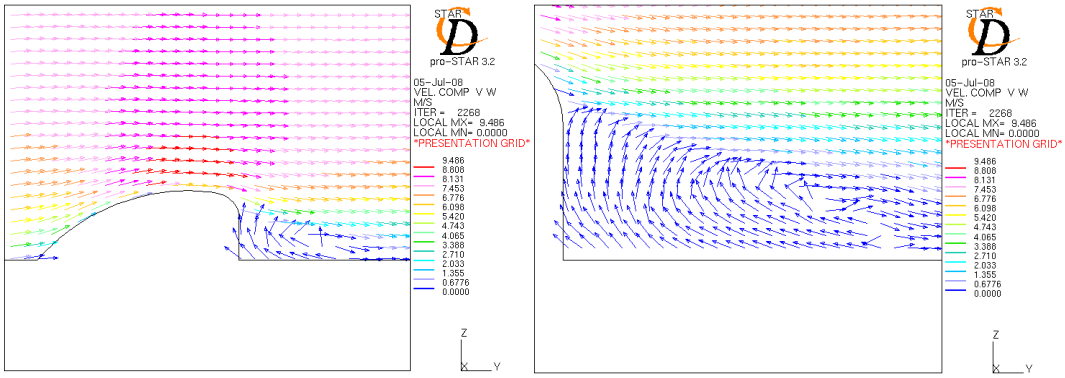

Figure 3.30: Velocity magnitude at plane 55 mm from mid section

Visualization of Differences in Flow Patterns

The sections above investigated the nature of airflow over each of the three shapes. Differences between the emerging patterns can clearly be seen. It remains a difficult undertaking to visualize the paths of a single air particle in three dimensions. Air particle tracks were therefore generated to aid in the envisaging of these pathways. Figures 3.31-3.36 shows the trails that particles will follow if they arrive at a certain height on the plant.

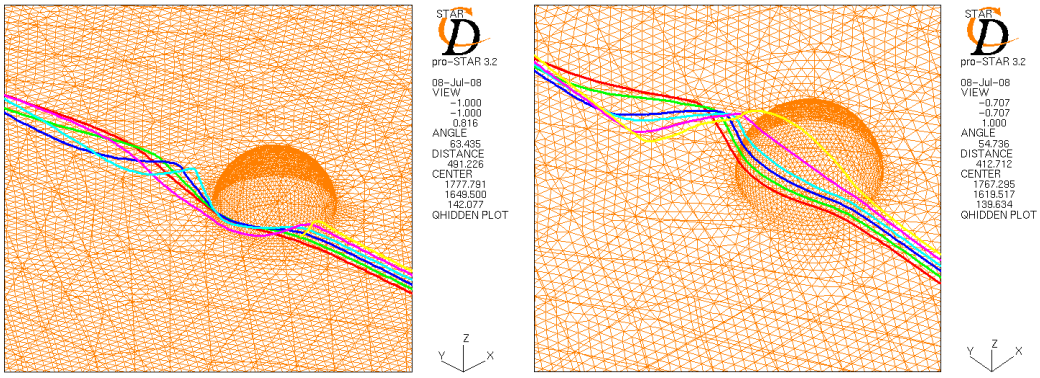

Figure 3.31: Particles arriving at the sphere 10 mm and 30 mm from ground level

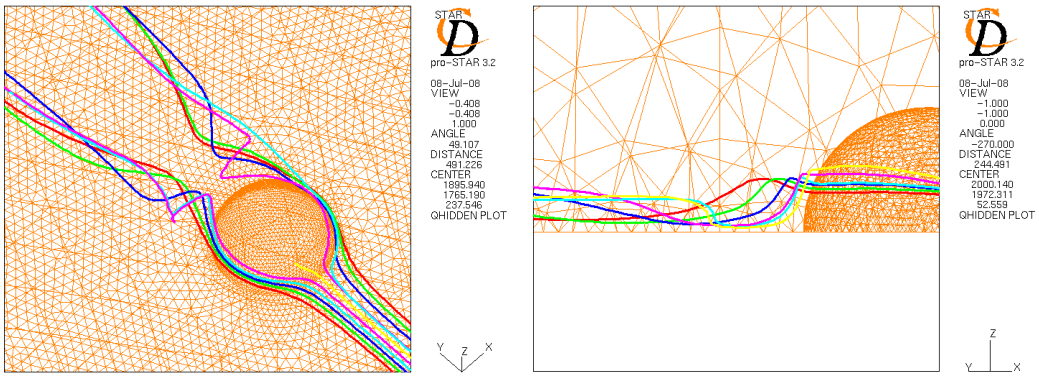

Figure 3.32: Air particle arriving at the sphere 20 mm from ground level

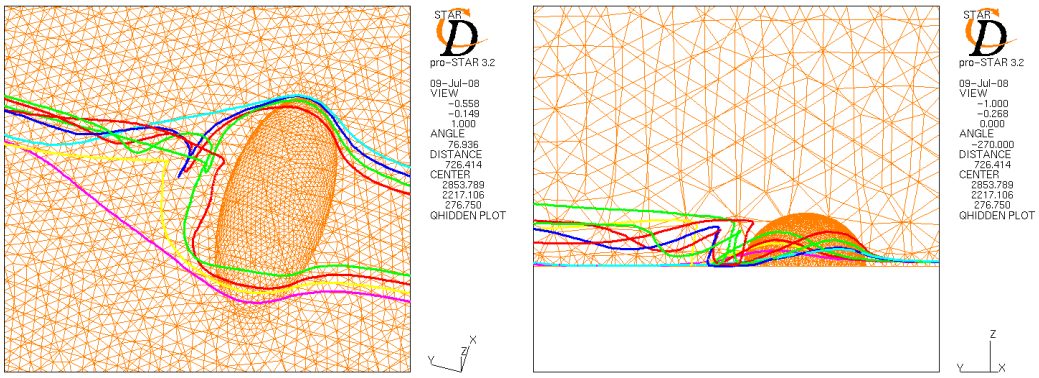

Figure 3.33: Air particle arriving at the ellipse 5 mm from ground level

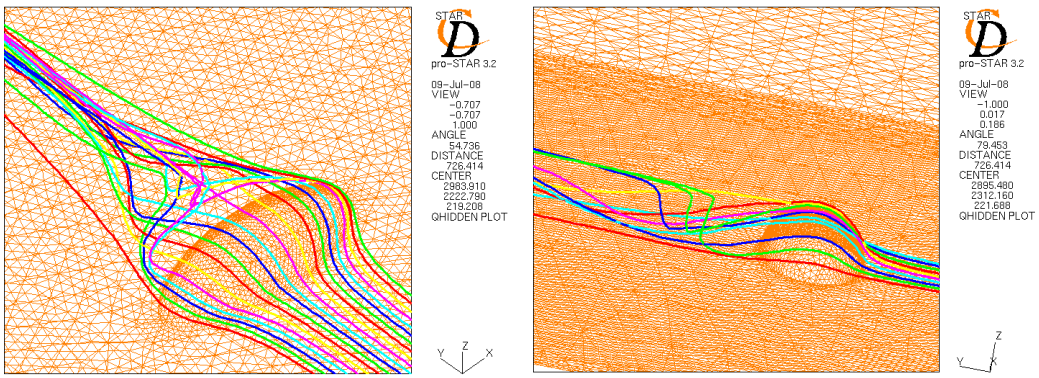

Figure 3.34: Air particle arriving at the ellipse 10 mm from ground level

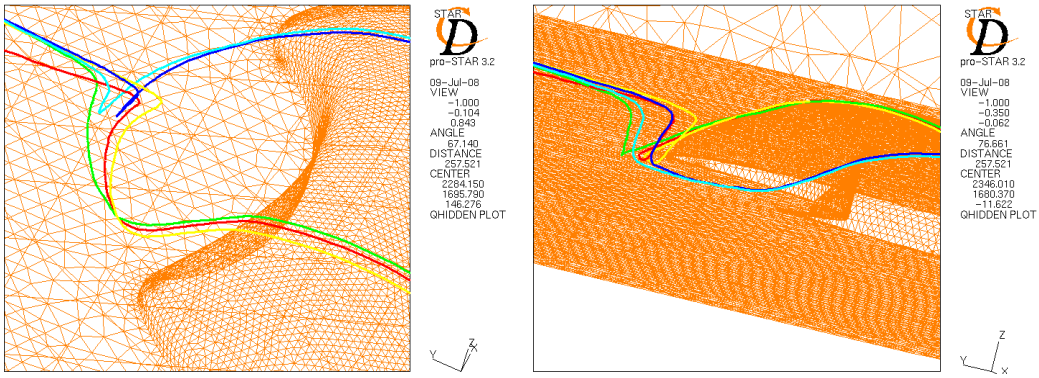

Figure 3.35: Air particle arriving at the crescent 2 mm from ground level

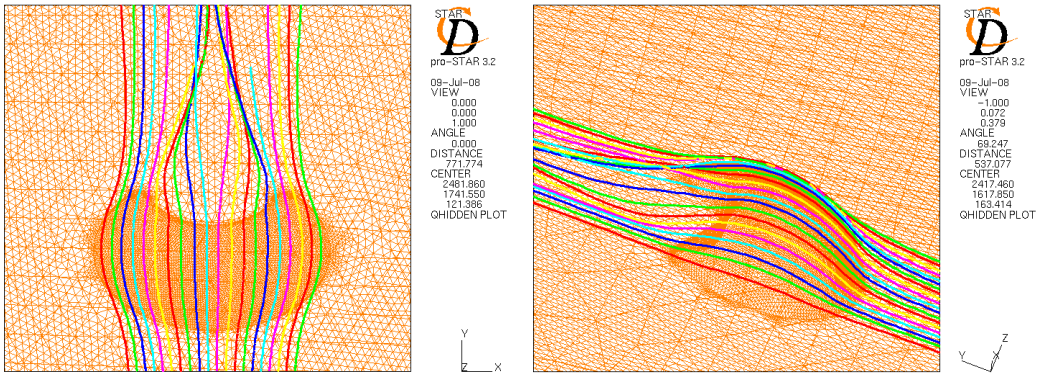

Figure 3.36: Air particle arriving at the crescent 15 mm from ground level

3.5.2 Analysis of Hemisphere Shape Size Effects

The static pressure profiles over the middle section of the plant are extrapolated from data points obtained from the simulations. A profile is extracted for each of the four cases; similar patterns emerged from the extrapolated data. At 0° all the profiles shows a positive pressure gradient. The first turning points for individual

graphs vary as indicated in Figure 3.37. The lowest static pressures is recorded at 90°, comparison indicated that the medium profile displays the lowest pressure and the extra large profile the highest. An unusual observation is made between the first turning point and the point of lowest pressure on the large and extra large graphs; the pressure does not maintain a negative gradient between afore mentioned point. It briefly obtains a positive pressure gradient resulting in two turning points not present in the small and medium profiles. This is due to the geometrical differences of the models. The graphs appear to intersect at approximately 122°.

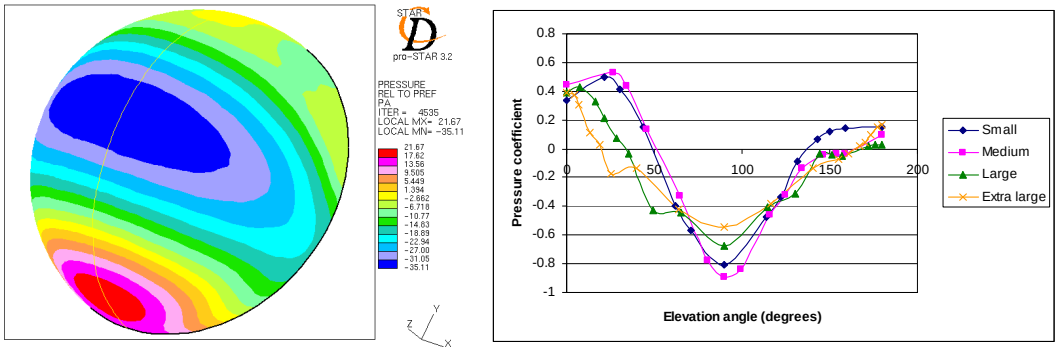

Figure 3.37: Pressure profile over different sizes of the hemisphere

A further method used to compare the different models is to extrapolate velocity profiles at various positions on each grid. Position one is directly in front (windward) of the plant, position two is directly behind (leeward) the plant, position three is located 400 mm leeward of position two and position four is directly on top of the plant. Figure 3.38 shows that the small model reaches a free stream value of approximately 8 m/s much quicker than the other model. This is due to the height of the model being much smaller than the other models. It is further apparent that the models will reach free stream at position one, two and three in order of lowest height to greatest. The height is an obstruction to the flow, therefore the greater the height leads to a greater obstruction and the longer it will take the profile to reach free stream. Position four in Figure 3.39 visualizes the acceleration of airflow over the plant as discussed previously in this chapter. It is interesting that the medium model has a greater over shoot of the free stream velocity than any of the other models. This can be explained by examining the dimensions of the model. The diameter of the plant is originally proportional to the height. Due to the strong winds of Marion Island the plant reaches an optimum height, at this point its diameter expands horizontally while the height remains fairly constant. The front gradient of the plant decreases, this produces in a lower pressure (Fig. 3.37) and a lower overshoot velocity.

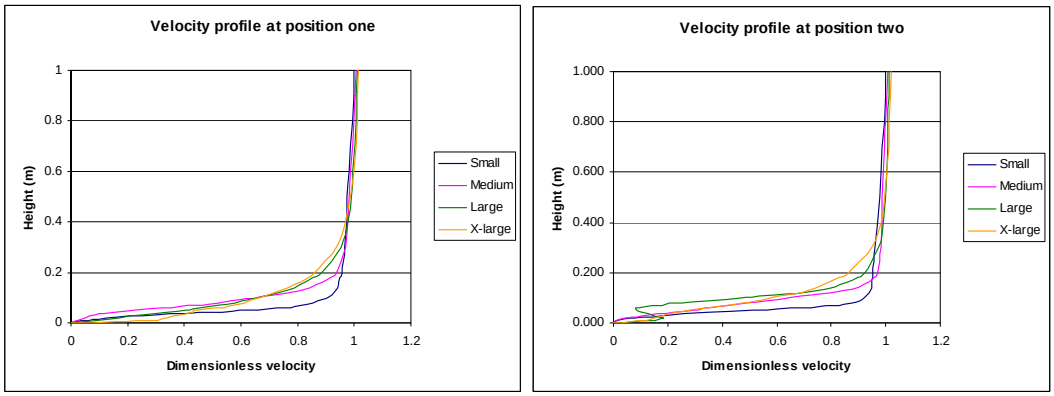

Figure 3.38: Velocity profiles at position one and position two

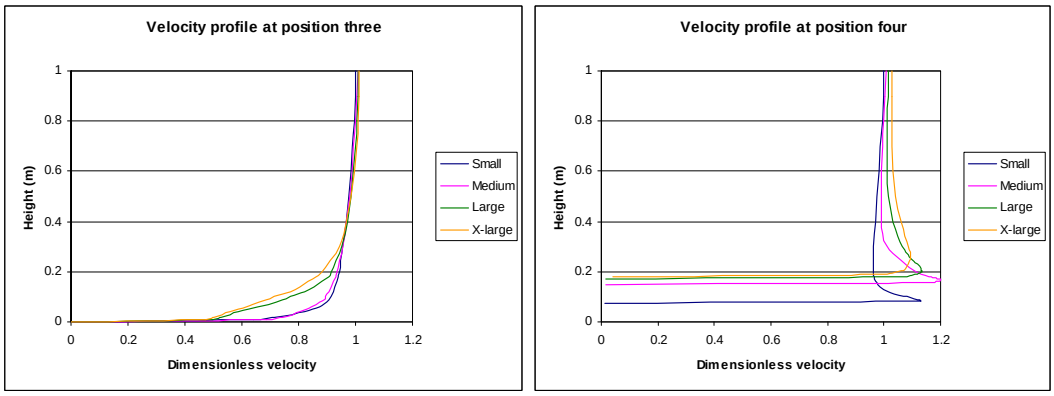

Figure 3.39: Velocity profiles at position three and position four

The lateral force instability manifested in the simulation of the large and the extra large hemispheres (Fig. 3.40). This non-axisymmetric vortex shedding (see section 2.2) is a result of the fully turbulent flow in the wake.

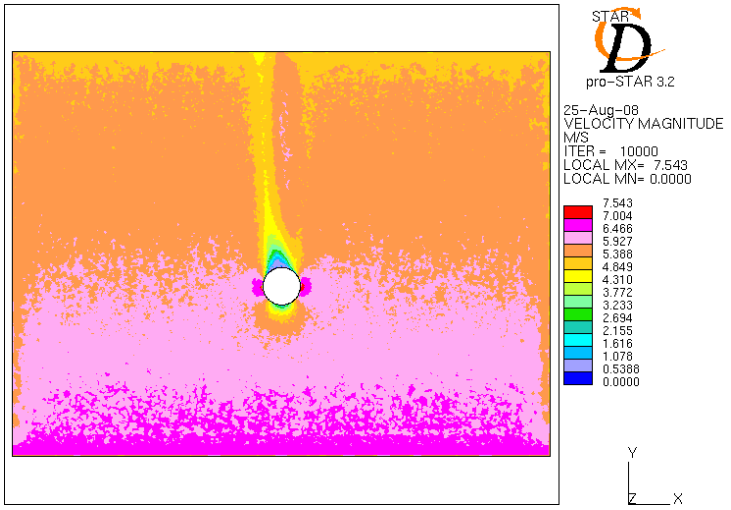

Figure 3.40: Lateral force instability mode of the large hemisphere

3.5.3 Analysis of Ellipsoid Shape Size Effects

Pressure profiles are extrapolated for each of the three models; these profiles are taken over the centre line of the plant. At 0° all profiles indicate a positive pressure gradient with turning points relatively close to one another. Lowest pressure values are observed at 90° and there is no significant difference between the lowest values for each profile (Fig. 3.41). The profiles do not appear to cross each other simultaneously as in the case of the hemisphere. The medium and the large profile intersect at approximately 122° and cross the small profile at 136° and 134° respectively. Velocity profiles at positions one, two, three and four of the ellipse is at the same locations as in the case of the hemisphere (Fig. 3.42 and Fig. 3.43).

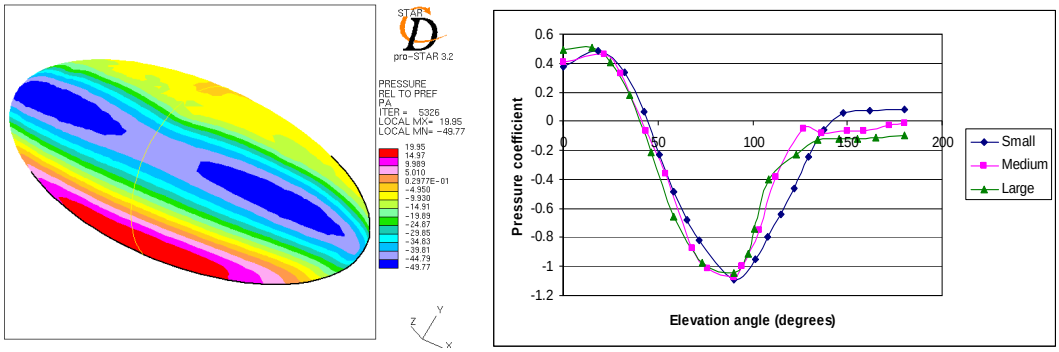

Figure 3.41: Pressure profile over different sizes of the ellipse

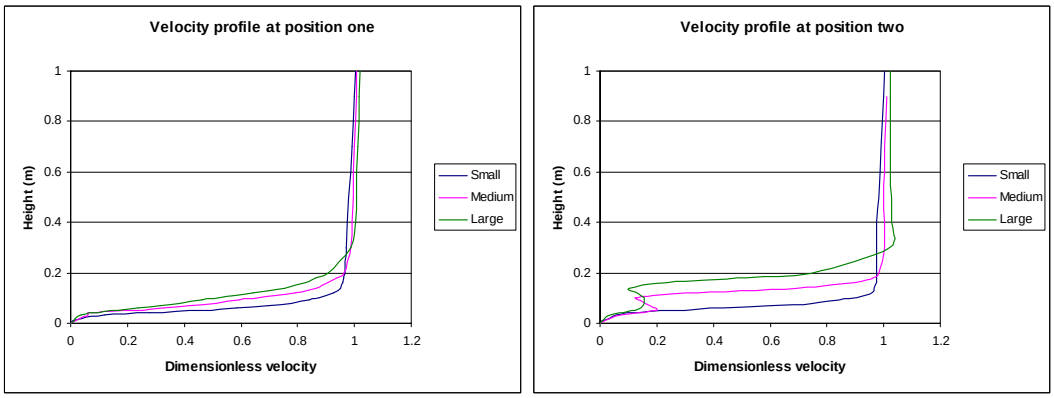

Figure 3.42: Velocity profiles at position one and position two

The distinct differences in height result in the same patterns as previously identified: a smaller height will result in more rapid achievement of free stream velocity with respect to height. It is apparent in al the cases that the small ellipse profile obtains free stream well before the other two profiles. At position two and three the medium and large profiles shows distinct patterns of variation in velocity below 0.2 m. This is a clear indication that the profile is situated in the recirculation zone. However, lack of variation is not necessarily an indication of

the absence of recirculation. It might still be present as in the case of the small ellipse but is not as pronounced as in the other two cases.

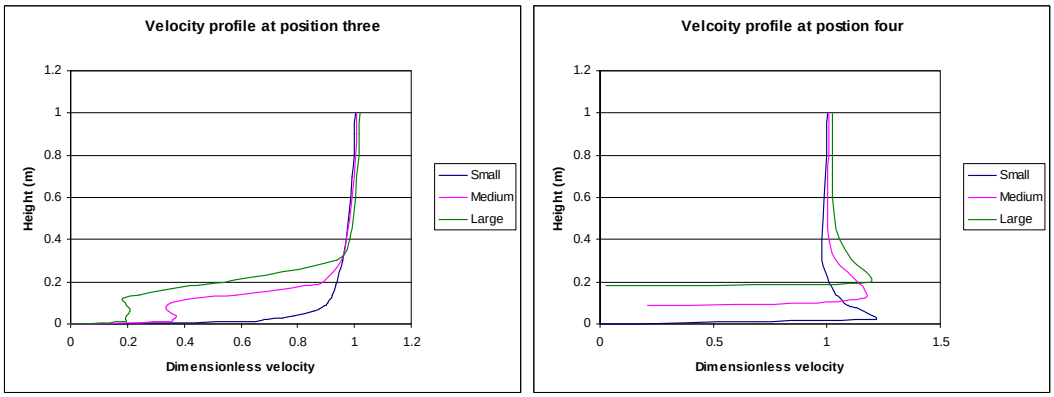

Figure 3.43: Velocity profiles at position three and position four

3.5.4 Analysis of Crescent Shape Size Effects

The extrapolated pressure profiles of the medium and the large crescent shape models indicated that no initial positive pressure gradient exists (Fig. 3.44). The profile has an immediate negative gradient, with the lowest point located at 90°. Intersection of the profiles occurs at approximately 122°. Aft of 150° the profiles maintain almost equal constant values due to the geometric similarity of the models.

Figure 3.45 and Figure 3.46 display the velocity profiles obtained at various locations on the model. Position two alfa is located directly behind the crescent. Position two beta is inline with the edges of the crescent. Position three and four are at the same positions as in the previous section. As seen in the previous cases, the model with the smallest height will attain free stream velocity first. The presence of recirculation is very prominently observed at position two beta due to the variation of lower level flow. Overshoot of the free stream is detected at position four, with the large crescent having the highest velocity.

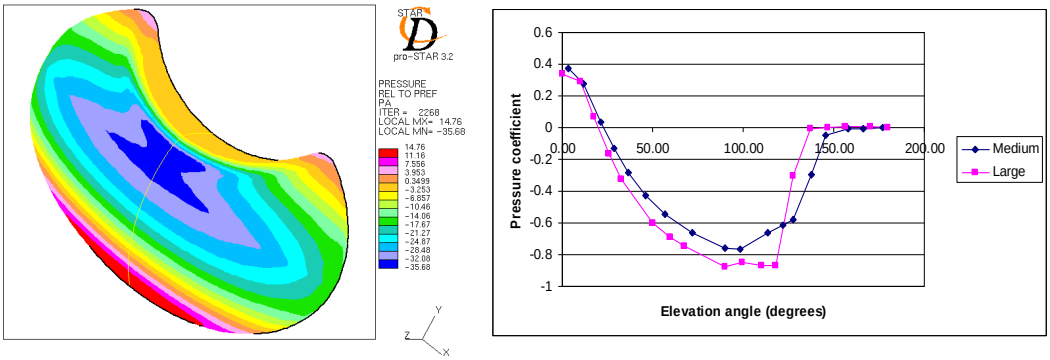

Figure 3.44: Pressure profile over different sizes of the crescent shape

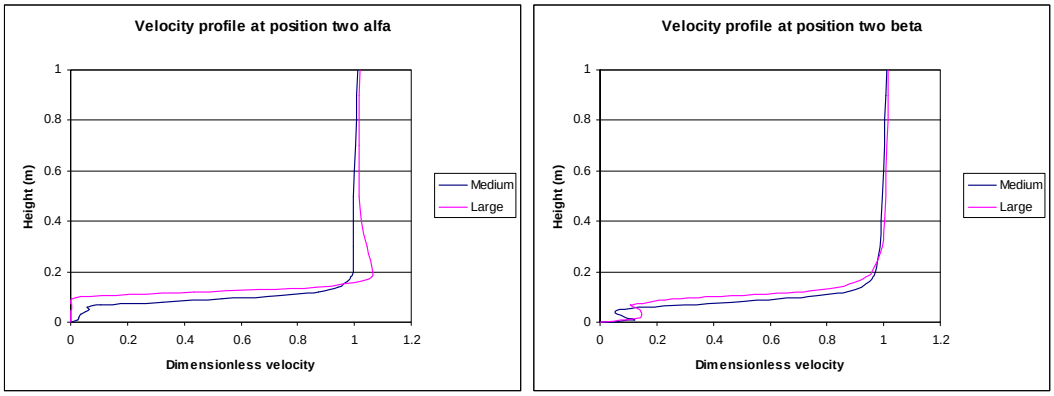

Figure 3.45: Velocity profiles at position two alfa and position two beta

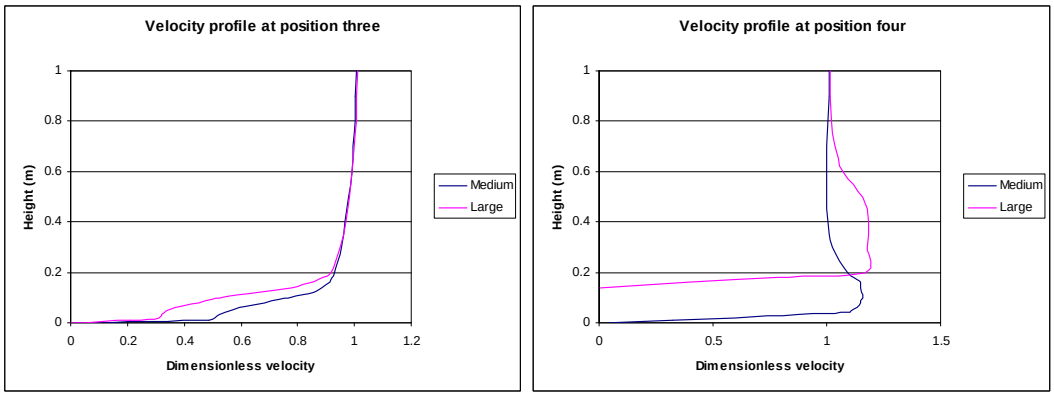

Figure 3.46: Velocity profiles at position three and position four

3.6 Summary

In this chapter the effect of plant shape and size on airflow as investigated. It was established that the plant, *A. selago*, is found in three shapes; hemisphere, ellipse and crescent. Nine different dimensions over the various shapes were indentified.

The appropriateness of utilizing a logarithmic velocity inlet profile was examined. Velocity profiles were measured on Marion Island during an expedition and the data fitted on a linearised form of Equation 4.2. The regression coefficients indicated that utilizing such a profile is suitable in this problem. The roughness height of the plant and the surroundings was identified to account for surface roughness in the simulations. Equation 4.6 was subsequently used as the velocity inlet profile in all simulations.

Each shape was analysed and the patterns that emerged discussed. The windward pattern for all shapes displayed similar qualities. In front of the object the flow slows down because the plant is an obstruction to the airflow. The velocity increases as the flow is forced over the top and along the sides of the objects. On the leeward side the shapes displayed distinctly different airflow patterns. The hemisphere showed two trailing lines typically associated with the horseshoe vortex phenomenon. There was almost no recirculation at the midplane with the flow reattachment point very close to the hemisphere. A distance from the midplane the recirculation became more distinct and reattachment occurred further away from the object. The ellipse displayed one distinctive trailing line. The recirculation patterns were opposite to the patterns of the hemisphere. Most prominent recirculation occurred at the midplane with a reattachment further away from the object. The most interesting flow patterns were found when analysing the crescent shape. Three trailing lines were observed, the side lines quickly dissipates with increasing height while the middle line remains distinctive. Complex recirculation patterns emerged and were further visualized by means of air particle tracks.

The difference in airflow when considering size variations were investigated by obtaining static pressure profiles over the objects and velocity profiles at different locations. All the analyses indicated that achievement of free stream velocity is strongly associated with the vertical height of the object, i.e. smaller heights will result in faster attainment of free stream velocity. The increase in velocity over the top of the plant was investigated. It was determined that variation of velocity in the lower regions is an indication that recirculation occurs in that area. However a lack of variation does not indicate the absence thereof, in such a case recirculation might occur but to a minimal extent.

Chapter 4 – The Light Particle Deposition of *Agrostis magellanica* Seeds on Cushion Plants

4.1 Introduction

The grass species *Agrostis magellanica* is the second most common vascular plant species on Marion Island (Huntley, 1971). It is dominant in the low altitude mire habitats (Fig. 4.1). It is also found at higher elevations as an epiphyte; rooted within another plant rather than in the soil. *A. magellanica* is the most common vascular epiphyte on the cushion plant, *A. selago* (Huntley, 1972).

Figure 4.1: *Agrostis magellanica* in a low altitude mire habitat (Le Roux, 2007)

The adverse effect of climate destabilization on *A. selago* was discussed in Chapter 1. As the second most common vascular plant species, *A. magellanica* may very well out-compete *A. selago* for space, light, water and nutrients in warmer conditions. It is therefore imperative that the various interactions between these two species be fully comprehended.

In the harsh environments associated with the higher altitudes on the island, intensified interaction between *A. selago* and *A. magellanica* is observed (Le Roux and McGeoch, 2008). It is apparent that the altitudinal limit where *A. magellanica* grows naturally is extended in the presence of *A. selago*. At higher elevations the abundance and biomass of *A. magellanica* on the soil is low while the majority of the population grows epiphytical on *A. selago* (Fig. 4.2). Studies have indicated that *A. magellanica* grows primarily on the leeward side of *A. selago* (McGeoch *et al*, 2008). The reason for this phenomenon is not clear and warrants investigation.

The aim of Chapter 4 is to obtain insight into the reason why *A. magellanica* grows on the leeward side of *A. selago.* This will be accomplished by investigating the deposition of *A. magellanica* seeds on *A. selago*, atmospheric airflow being the mode of transportation.

Figure 4.2: *A. selago* with *A. magellanica* on the leeward side (Le Roux, 2007)

4.2 Particle Drag Coefficient

This section describes the process followed to determine the approximate value of the particle drag coefficient of an *A. magellanica* seed. The drag coefficient at terminal velocity is an independent variable required to quantify the drag interaction between the airflow and the seed. The seeds are assumed to be spherical particles with a diameter of 3 mm. A gravitational drop test is utilized to determine the terminal velocity experimentally. Furthermore, the Matlab program (version R2007b) is employed to determine the terminal velocity analytically. Four correlations were identified as suitable for the range of Reynolds numbers associated with the terminal velocities. The Flemmer and Banks (1986) correlation is found to have the least difference between the numerical and experimental drag coefficient, and is therefore most suitable for this application.

4.2.1 Experimental Terminal Velocity

A freefalling particle reaches terminal velocity when the weight of the particles is balanced by the sum of the buoyancy experienced by the particle and the resisting viscous force caused by the flow of the fluid around the particle (Flemmer and Banks, 1986). In the current study the terminal velocity is determined by designing an experiment where the seeds are released at a position 4.15 m above an electronic precision balance. The seeds are discharged at the top end of a vertical round tube. The purpose of this tube is two-fold; it guides the seeds to the balance and prevents side drafts from influencing the rate at which the seeds fall

to the balance. Ideally the diameter of the tube must be as large as possible to prevent seeds from colliding against the sides of the tube. The electronic balance was interfaced with the Balint program via the RS232 serial port, from where the data could be exported to a spreadsheet program for further analysis. Figure 4.3 displays the results of the experiment. Experimental equipment is detailed in Appendix G:

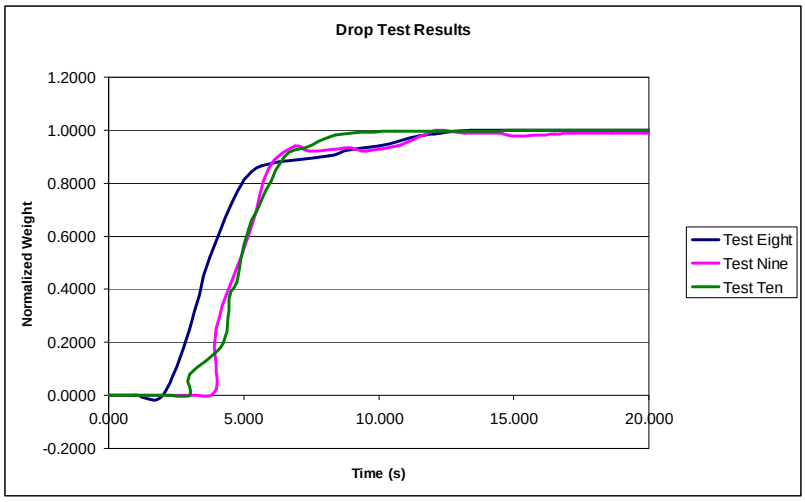

Figure 4.3: Results from drop tests conducted on *Agrostis magellanica* seeds

The shape of the graphs indicates a late discharge of the seeds from the top end. In an ideal situation a vertical line will be visible at the first instance of seed arrival. Instead, the first arrival is followed by a line with an approximate gradient of 70°. After the arrival of approximately 85% of the seeds, the remainder arrives. These seeds are delayed by the loss of momentum due to collision with the wall of the tube. Hence the average moment of first arrival (3.33s) will be taken as the time it takes a seed to fall 4.15 m. Based on the density of the seed the assumption is made that terminal velocity is reached instantly as the seed is released in the tube. The terminal velocity is then determined in the following manner:

$$u = \frac{s}{t}$$

$$u = \frac{4.15m}{3.33s} \qquad (4.1)$$

$$u = 1.25m/s$$

4.2.2 Drag Coefficient Equations

There are various equations available in the literature that offers a mathematical approximation to the drag coefficient. Most of these equations are based on the particular Re associated with the free stream velocity, while others bring the terminal velocity into consideration. Four approximations based on the Re are identified as suitable for this application:

Schiller and Naumann, (1933)

$$C_D = \frac{24}{\mathrm{Re}} + \frac{3.6}{\mathrm{Re}^{0.313}} \tag{4.2}$$

Cliff and Gauvin, (1970)

$$C_D = \frac{24}{\mathrm{Re}}(1 + 0.15\,\mathrm{Re}^{0.687}) + \frac{0.42}{1 + 4.25 * 10^4\,\mathrm{Re}^{-1.16}} \tag{4.3}$$

Perry and Chilton, (1973)

$$C_D = \frac{18.5}{\mathrm{Re}^{0.6}} \tag{4.4}$$

Flemmer and Banks, (1986)

$$C_D = \frac{24}{\mathrm{Re}} 10^E$$

where (4.5)

$$E = 0.261\mathrm{Re}^{0.369} - 0.105\,\mathrm{Re}^{0.431} - \frac{0.124}{1 + (\log_{10}\mathrm{Re})^2}$$

4.2.3 Calculated and Experimental Drag Coefficients

The drag coefficient and terminal velocity was analytically determined utilising the Matlab R2007b program. An example of this program, employing the Cliff and Gauvin correlation, is presented in Appendix F. The terminal velocity determined experimentally in section 4.2.1 is used to determine the experimental drag coefficients. Table 4.1 presents the different drag coefficient values obtained. The correlation with the smallest difference between the calculated and experimental data is selected as the most appropriate value for this application. Incidentally, the Flemmer and Banks correlation was previously proven to be

superior to other equations (Flemmer and Banks, 1986). In this case it will suffice to effectively quantify the drag interaction between the air and the seed particle.

Table 4.1: Calculated and experimental drag coefficient data

Correlation	Calculated Data			Experimental Data			Cde-Cdc
	Re	Ut	Cd	Re	U	Cd	
Schiller & Naumann (1933)	735.402	3.697	0.489	247.860	1.246	0.738	0.249
Cliff & Gauvin (1970)	718.306	3.612	0.512	247.860	1.246	0.744	0.231
Perry & Chilton (1973)	928.613	4.669	0.307	247.860	1.246	0.677	0.371
Flemmer & Banks (1986)	748.520	3.763	0.472	247.860	1.246	**0.681**	**0.209**

4.3 Pre-processing

The physics involved in Chapter 4 must not be confused with the physics that result in sand accumulation behind a solid object in the desert. In the latter case the flow of particles is very close to the ground and will accumulated in areas of low shear stress and decreased velocity. In this case the seed particles should be viewed in the same light as contaminants in the air further removed from the ground level. It must further be established that the seed particles will not readily roll along the surface of the plant, but will attach to the location of impact without further transportation. This is due to the surface texture (Fig. 4.2) of the plant and the morphology of the seed particle.

Two models are analysed to determine the deposition of the seed particles. Flow simulation models with the designations X3S_0803034_m and X3B_080310_l have already proven to be grid independent in Chapter 3. These models were utilised with exactly the same conditions as previously, except that Eulerian multi-phase flow is enabled. The continuous phase is defined as air and the dispersed phase as the seed particles with a volume fraction of 0.01%. The drag coefficient was defined as 0.681 which is the value from the Flemmer and Banks correlation in Table 4.1. The virtual mass was left per default value of 0.5. The virtual mass is the summation of the actual mass and the added mass. The added mass accounts for the force exerted by fluid particles around an accelerating or decelerating body. The body experiences a force as if its mass is increased by the added mass. Appendix G displays the data pertaining to the weight, size and density of the seed particles.

4.4 Solving

The simulations are solved in the steady state domain with double precision for incompressible flow. The AMG solution method is employed in conjunction with the SIMPLE solution algorithm.

Satisfactory convergence was reached for all simulations. The number of iterations performed for the hemisphere and the crescent were 4460 and 1565 respectively. The y^+ values for the hemisphere was within acceptable parameters; a minimum of 29.59 and ‘n maximum of 146.8. The crescent shape displayed y^+ patterns similar to previous simulations in Chapter 3, Figure 3.9. The values in this case vary between 5.358 and 305.5, the areas on the crescent that are below the value of 30 is insignificantly small and will not have considerable influences on the results of the simulation.

The method of discretisation is specified in the source code of the Eulerian multiphase model, therefore it can not be controlled by the user. Upward differencing is utilised to determine the values of the momentum, turbulent kinetic energy and phase variables. Central differencing is employed to govern the solutions of the mass conservation equation from one iteration to the next. The use of upward differencing could lead to numeric diffusion and inaccuracies of data, in particular when comparing the results of the continuous phase to results obtained from previous simulations utilizing central differencing. The use of upward differencing is justified by the presence of the dispersed particles; however the degree of numeric diffusion of the continuous phase must be investigated.

4.5 Post processing

The models used for this analysis have previously been proven to be grid independent when utilising single phase flow. The addition of the seed particles should not influence the airflow significantly because the volume fraction was specified to be merely 0.01%. However, the use of the upward differencing scheme in the Eulerian multi phase flow could result in numeric dispersion and numerical inaccuracies. In the light of this a pressure profile was extracted from the multi phase simulations and compared with profiles from the previous chapter (Fig. 4.4). This comparison showed minor numeric differences between profiles.

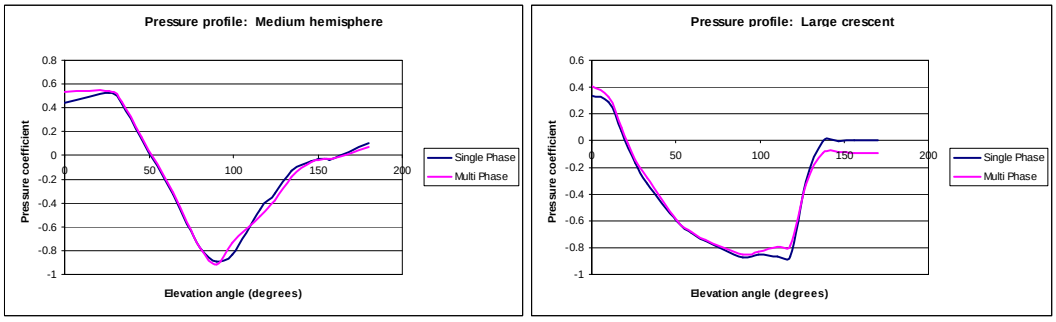

Figure 4.4: Comparison between single and multi phases simulations

Upwind differencing will cause a certain degree of numeric diffusion and inaccuracy. Figure 4.5 and Figure 4.6 compare the velocity magnitude of the air using the single phase model and the multi phase model. Additional comparative figures are displayed in Appendix H. These figures indicated that the velocity magnitude pattern is more pronounced in the single phase model than in the multi phase model. In the case of the hemisphere the horse shoe vortex diminishes more rapid in the multi phase model. Swift resolution of the vortex patterns of the crescent shape is also observed.

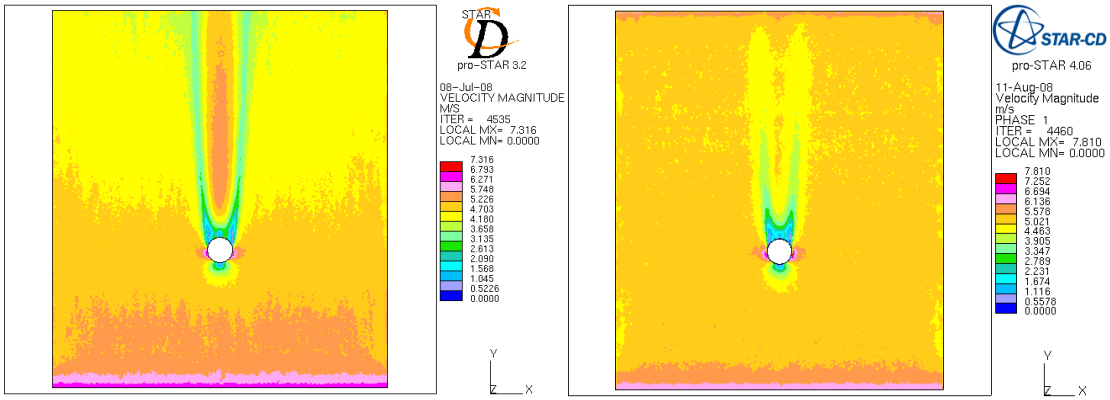

Figure 4.5: Velocity magnitude dispersion at a plane 7.5 mm from ground level

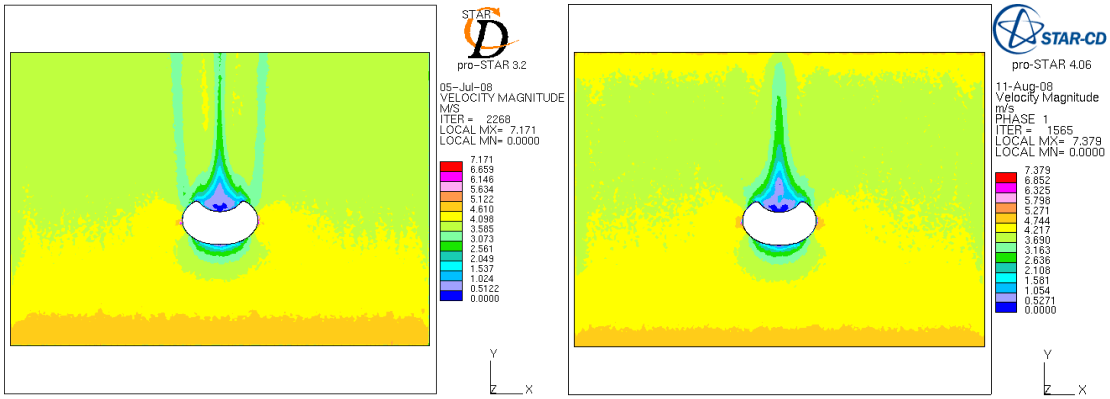

Figure 4.6: Velocity magnitude dispersion at a plane 11 mm from ground level

In this analysis Phase 1 is defined as the continuous fluid and Phase 2 as the dispersed particles. Thus Phase 1 represents the airflow and Phase 2 the seed particles. The various phases behave differently in the proximity of the plant; this is illustrated in Figure 4.7 and Figure 4.8. The key to the understanding this dissimilarity of behaviour lies in the disparity in the nature of the phases. Phase 1 is air in a continuous, natural, gas state while phase two consists of dispersed, solid particles. In locations other than the stagnation point, the path of an air particle does not discontinue when in close proximity with the surface of the plant. It is deflected away from the plant or is guided around the curvatures. The path of a solid particle, on the other hand, would be terminated and the particle

lodged on to the plant as they are unable to follow the airflow stream. The results show that interphase particle-air drag forces are insufficient to lift a significant portion of the seeds over the plant. The solid particles are approximately twenty times denser than the air; subsequently a solid particle will be twenty times heavier than an air particle of the same size. The first and second laws of Newton apply; the greater mass of the seed particle results in a higher momentum and a higher state of kinetic energy requiring great forces to change direction from the viscous interaction with the air stream. The difference in mass (as a direct result of the difference in density) makes it impossible for the air and seed particles to behave alike.

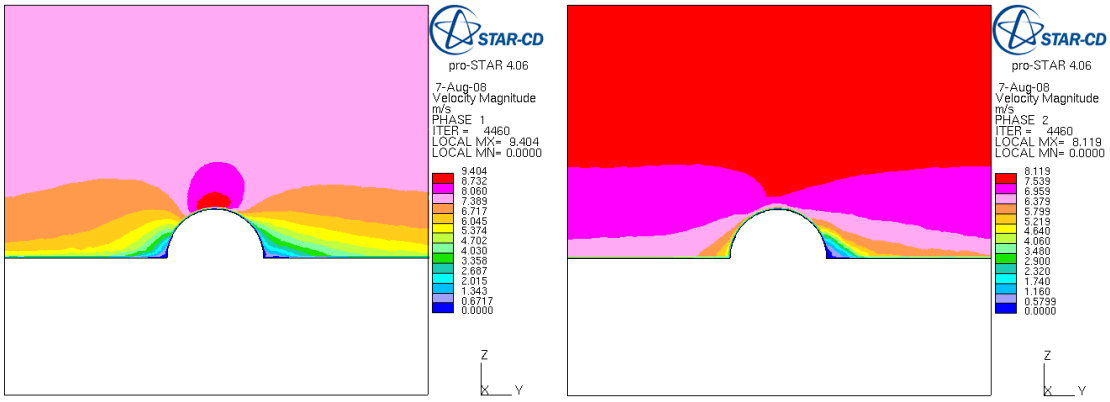

Figure 4.7: Velocity magnitudes of phases one and two at midplane of sphere

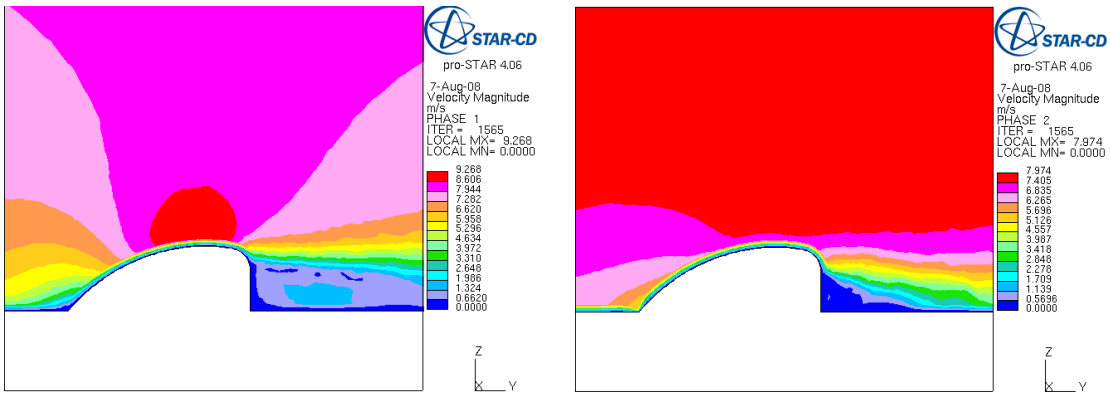

Figure 4.8: Velocity magnitude of phases one and two at midplane of crescent

The greatest deposition of *A. magellanica* seeds on *A. selago* is found on the windward side of the plant. This can clearly be seen in Figure 4.9 and Figure 4.10 where the air is flowing in the positive y-direction.

In light of the above mentioned explanation regarding density difference, the results obtained concerning the volume fraction is to be expected. The majority of the particles arrive on the windward side of the plant. They do not flow around the plant as in the case of the air particles, but are trapped by the rough surface of

the plant. It was discussed in Chapter 3 that on the sides and at the top of the plant the airflow velocity increases which causes an increase in the momentum and kinetic energy of the seed particles. In this heightened state the particles will deflect away from the plant in the direction of the residual forces. Few particles are deposited on the leeward side of the plant as a result of the recirculation in the flow field. The recirculation is shown in Figure 4.11 and Figure 4.12.

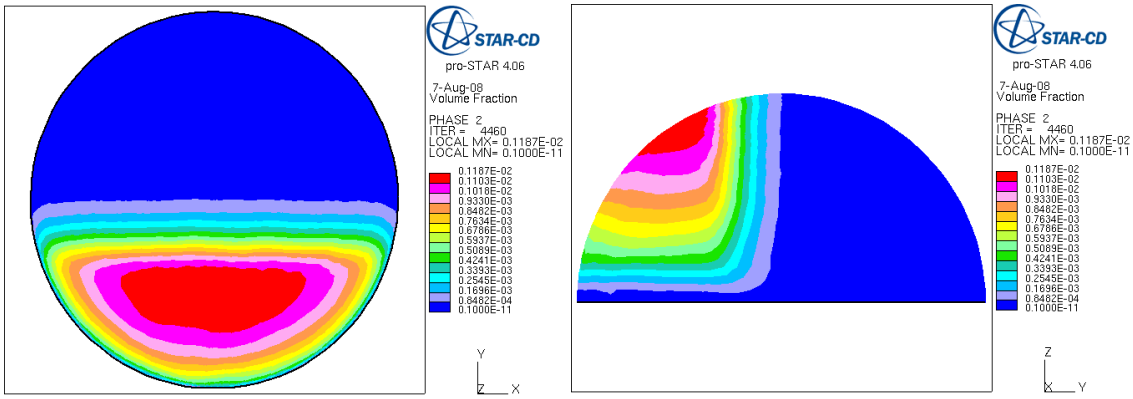

Figure 4.9: Volume fraction of seed particles on medium hemisphere shape

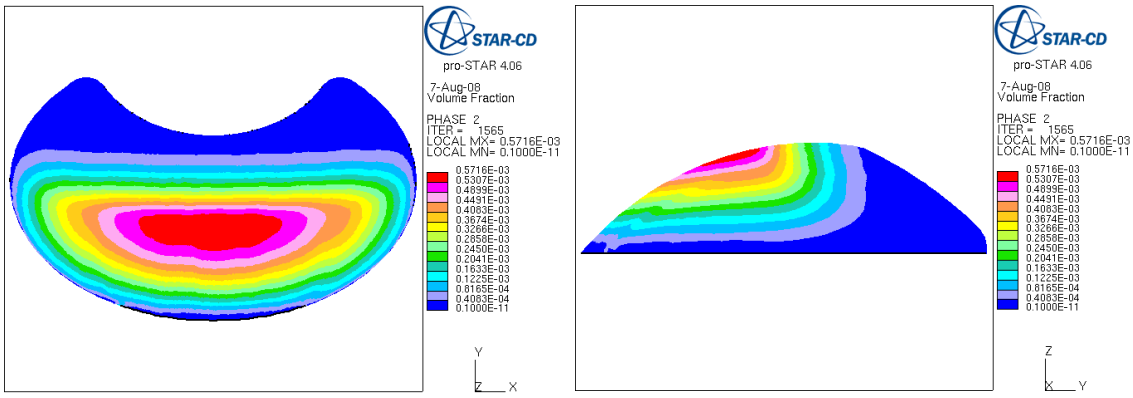

Figure 4.10: Volume fraction of seed particles on large crescent shape

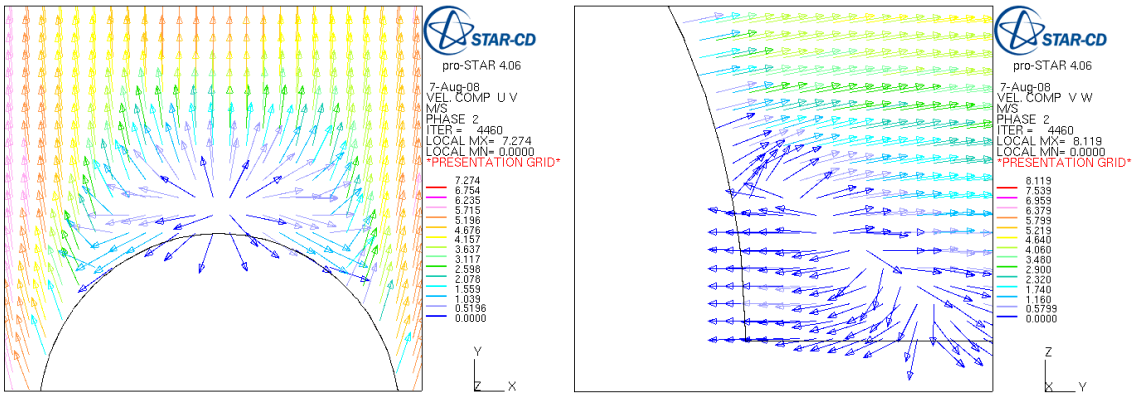

Figure 4.11: Velocity vectors of seed deposition through recirculation on sphere

Investigation into the extent of the recirculation patterns have shown that the medium hemisphere recirculation extends to a height of 39 mm and the large crescent to 81 mm. The respective heights of these models are 150 mm for the hemisphere and 140 mm for the crescent. It can be deducted that percentage of particles at the leeward side of the crescent will significantly more than for the hemisphere. The shape of the plant thus plays a definite role in the intensified interaction between *A. selago* and *Agrostis magellanica*.

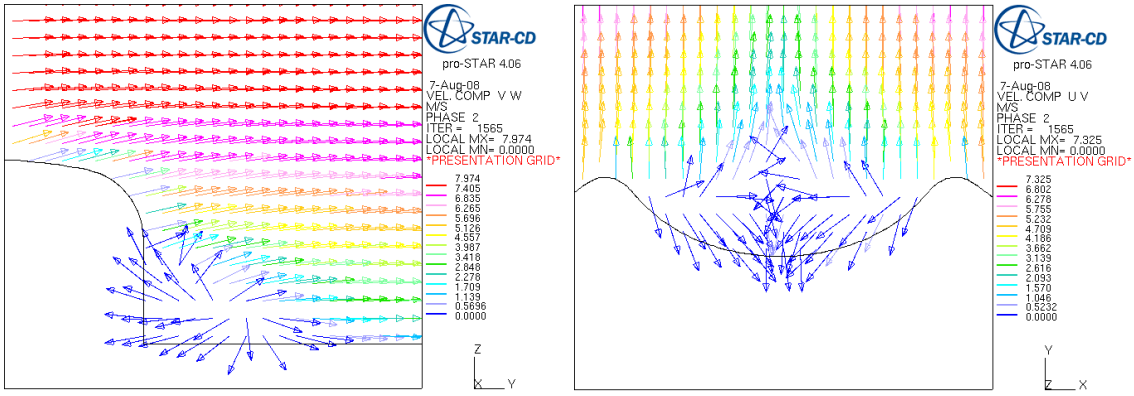

Figure 4.12: Velocity vectors of seed deposition through recirculation on crescent

4.6 Summary

The results that were obtained in this chapter pose an apparent paradox: the greatest number of light particles (*A. magellanica* seeds) is found at the windward location of *A. selago*, while physical evidence clearly indicates growth primarily on the leeward position. This apparent contradiction can, however, be explained when the environmental conditions of the natural habitat are considered.

The environment on Marion Island is known for its harsh and unforgiving conditions. It is notorious for the elevated wind speeds and low temperatures: wind speeds above 50 knots are not uncommon to the island and temperatures well below zero degrees Celsius have been recorded. The analyses conducted in the previous chapters indicate that the leeward location on *A. selago* is protected from the harsh environmental conditions. Wind speeds are minimal and it is reasonable to hypothesize that the wind chill factor are nominal at this position. It will therefore be a more suitable site for the fostering of a vulnerable seedling that on the exposed windward side. Although more seeds are deposited on the windward surface, it is unlikely that any seedlings will endure the callous conditions of the micro climate. The apparent paradox is a good attribute of a system that can only be understood once all the relevant factors are considered. The importance of this concept should never be underestimated as it can lead to incorrect conclusions.

Chapter 5 – The Exertion of Physical Force on the Cushion Structure

5.1 Introduction

Chapter 3 revealed the dissimilarities in the airflow patterns around different shapes and sizes of the *A. selago* plant. The various velocity patterns were discussed in detail. A discussion of the static pressure was accompanied by static pressure profiles over the centre line of the different plants. The subsequent force that is exerted on the plant was not discussed. This chapter reports on the physical forces that are associated with airflow over the cushion structure. The results shown were extracted from the analyses conducted in Chapter 3, therefore the pre-processing and solving methodology is not included in this discussion.

The aim of Chapter 5 is threefold:

- to visualise the physical forces that act on the cushion plant
- to reveal the dissimilarity in the forces for the different sizes of each shape
- to identify the critical zones on the plant

Static pressure, shear force and total force profiles are extracted for all the sizes of a particular shape. Figures are added to aid in the visualization of these forces. In all figures the direction of flow is in the positive y-direction. All contour plots refer to the medium hemisphere, large ellipse and large crescent.

5.2 Static Pressure

The forces that act upon a body can not be discussed before the pressure is understood. Pressure and force are interlinked; the larger the area of high pressure indicated, the higher the exerted force will be. In Chapter 3 the pressures were examined without bringing the forces into context. This section revisits the previous findings concerning pressure. In this context the static pressure is due to the pressure the atmosphere exerts on the plant resulting in a changing velocity field superimposed on the local atmospheric pressure.

5.2.1 Hemisphere Shape

Figure 5.1 illustrates the static pressure profiles of all the hemispherical plants analysed. The profile is taken along the midline of the sphere as indicated in the figure. At an elevation angle of 0° all the profiles showed a positive pressure

gradient, which basically reflect the increase of the upstream boundary layer velocity. The first turning points for individual graphs vary as indicated in Figure 5.1; this location is the onset of the negative pressure gradient associated with an increase in velocity. The lowest static pressures are recorded at 90°, as expected the velocity in the boundary layer is at a maximum at this location. A comparison indicated that the medium profile displays the lowest pressure and the extra large profile the highest pressure at this point. In the light of Figure 5.2 this is to be expected; a much higher velocity is observed at the apex of the medium sized plant than for the extra large plant. An unusual observation is made between the first turning point and the point of lowest pressure on the large and extra large plant profiles; the pressure does not maintain a negative gradient between afore mentioned point. It briefly obtains a positive pressure gradient resulting in two turning points not present in the small and medium plant profiles. This is due to the geometrical differences of the models; the height of the plants varies minimally while the diameter of the plants increases significantly. The graphs appear to intersect at approximately 122°.

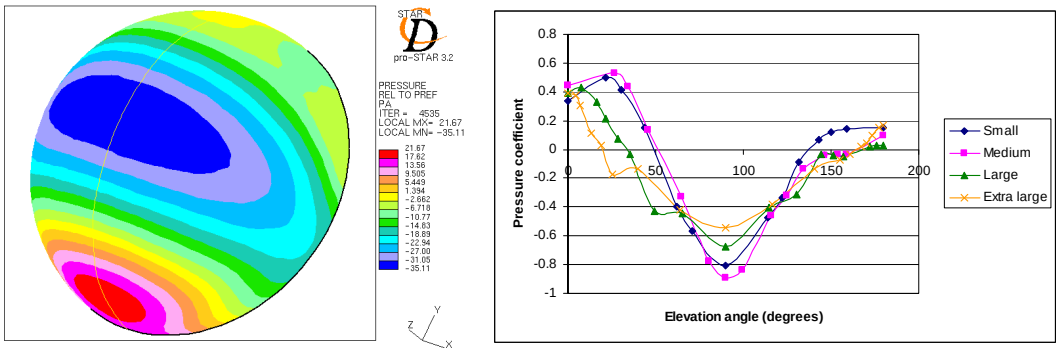

Figure 5.1: Pressure on hemisphere shapes

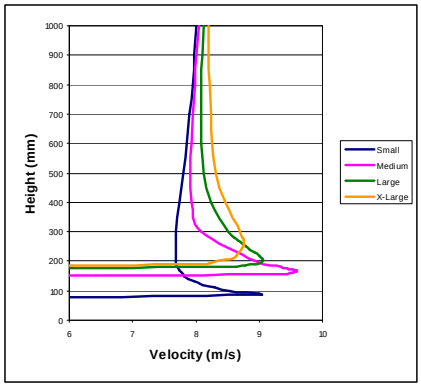

Figure 5.2: Velocity profile at the apex of the hemispherical shapes

5.2.2 Ellipse Shape

The static pressure profiles for the ellipsoidal plants were extracted in a manner similar to the hemispherical model profiles. Profiles were taken along the centreline of the ellipsoidal plants as shown in Figure 5.3. At an elevation angle of 0° all profiles indicates a positive pressure gradient, again this relates to the decrease in velocity. The turning points are relatively close to one another; this indicates the increase in velocity. The lowest pressure values, subsequently reflecting the highest velocity, were observed at 90°. There are no noteworthy differences between the lowest values for each profiles; the velocities at this point varies very little (Fig. 5.4). The profiles do not appear to cross each other simultaneously as in the case of the hemisphere. The medium and the large profile intersect at approximately 122° and cross the small profile at 136° and 134° respectively. It is apparent that the ellipsoidal shaped plants experience the least variance in pressure profiles of all the shape differentials.

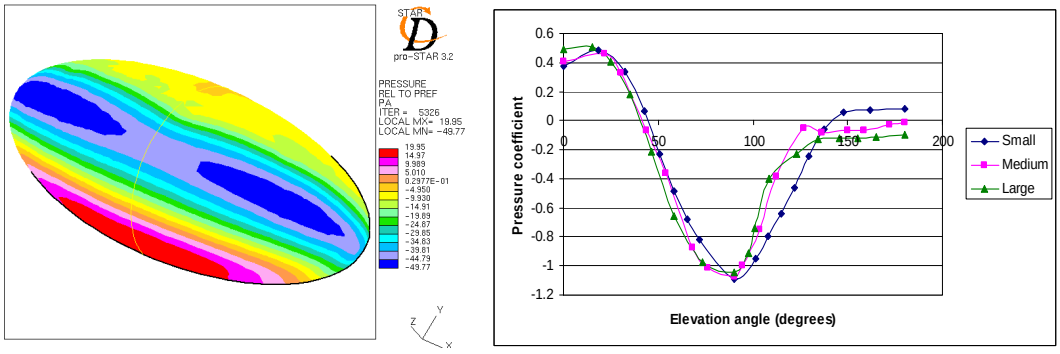

Figure 5.3: Pressure on elliptical shapes

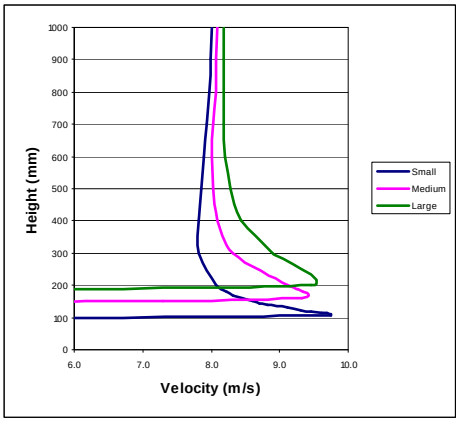

Figure 5.4: Velocity profile at the apex of the elliptical shapes

5.2.3 Crescent Shape

The static pressure profile of the centreline of the plant indicated an immediate negative gradient (Fig. 5.5). Unlike the flow over the hemispheroidal and the ellipsoidal shapes, flow over the crescent shaped plant experiences an immediate increase in velocity. The point of lowest pressure and highest velocity is located at 90°. Figure 5.6 displays the differences in velocity for both the medium and the large shaped plant. The large plant displays a lower pressure due to the higher velocity it experiences Intersection of the profiles occurs at approximately 122°. Aft of 150° the profiles maintain almost equal constant values due to the geometric similarity of the models on the leeward side.

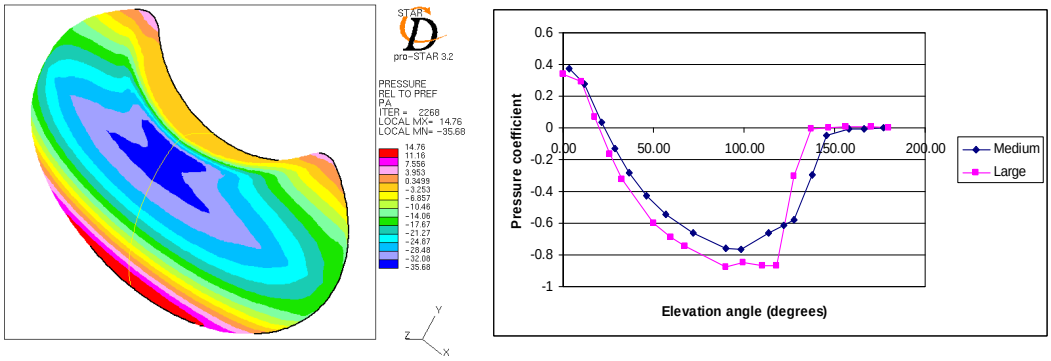

Figure 5.5: Pressure on crescent shapes

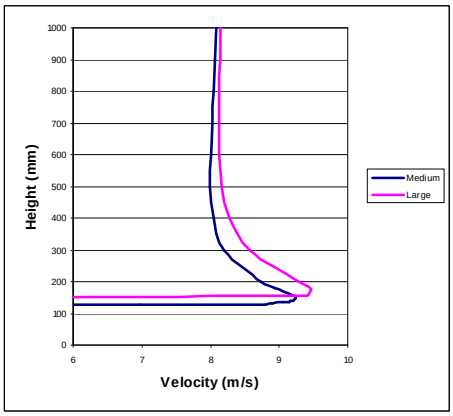

Figure 5.6: Velocity profile at the apex of the crescent shapes

5.3 Shear Force

A body that is immersed in a moving fluid is acted upon by pressure and viscous forces. The viscous force is a function of the interaction between the fluid and the

surface of the body and is caused by the viscous drag in the boundary layer. This relationship is shown in Equation 5.1.

$$\tau_{wall} = \mu\left(\frac{\partial u}{\partial y}\right)_{y=0} \tag{5.1}$$

This shear force must not be confused with the drag force. The drag force exerted on the body is a function of both the static pressure and the viscous forces. Furthermore, the drag force acts in a direction parallel to the direction of the free stream velocity, while shear force vectors are parallel to the surface of the object in question. Equation 5.2 indicates how the shear force is derived from the post-processing data in the CFD code. In this equation the boundary area is specified as the wall cell face area and the parallel velocity is the velocity vector component parallel to the wall at the centre of a near-wall cell.

$$F_{shear} = \tau_{wall} A_{boundary} \frac{v_{parallel}}{|v_{parallel}|} \tag{5.2}$$

Similar patterns are observed when comparing the results of the shear force of the different sizes of each of the plant shapes. These forces are shown in Figure 5.8 to Figure 5.10. Minimal shear force is exerted at the lower areas of the plant, while the maximum force is found in the area of the apex. This can be explained with reference to Equation 5.1 together with the velocity magnitude results of Chapter 3. The velocity of the air is the highest at the apex of the object and it decreases significantly towards the ground level (Fig. 5.7). Shear force is a function of shear stress which in turn is a function of the velocity (Eq. 5.1). A higher velocity gradient therefore directly results in a higher shear force. Consequently, a decrease in velocity, hence the gradient near the surface, will result in a decrease in shear force. The apparent numerical dispersion observed in the figures is a result of the boundary layer treatment and the surface roughness of the plant.

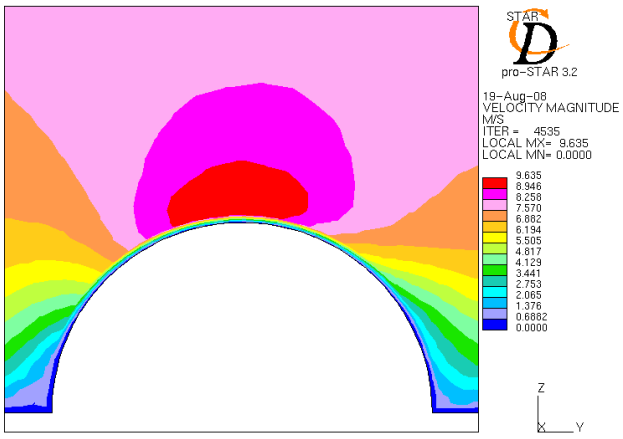

Figure 5.7: Velocity magnitude at the midplane of medium hemisphere

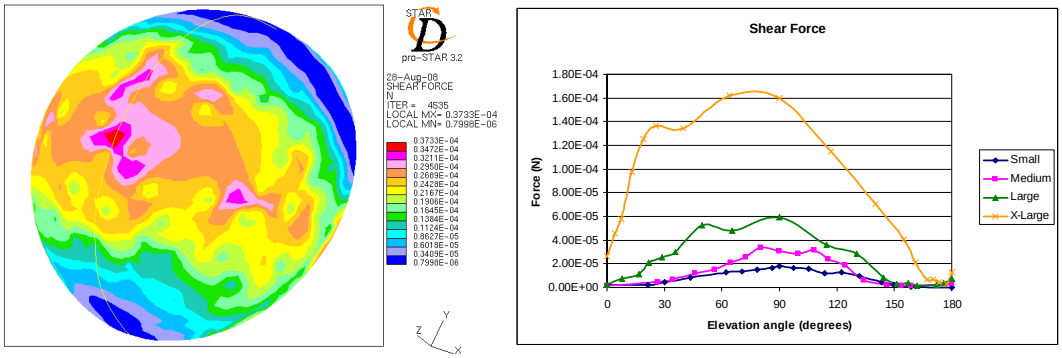

Figure 5.8: Shear force for the hemisphere shapes

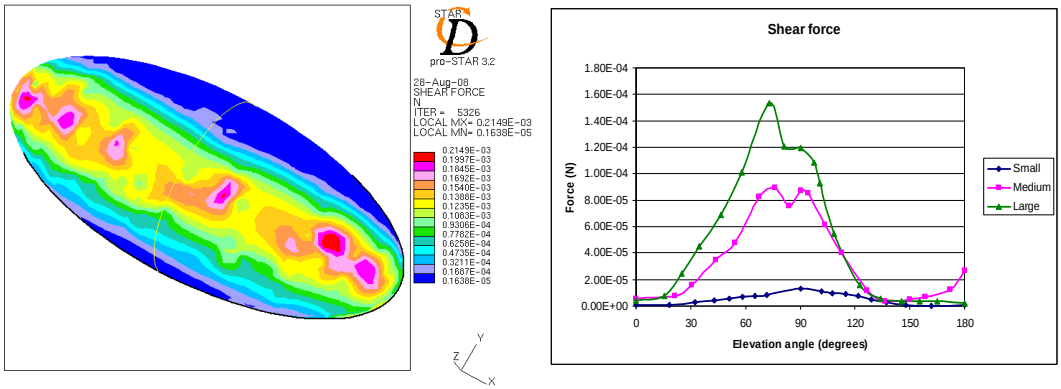

Figure 5.9: Shear force of the elliptical shapes

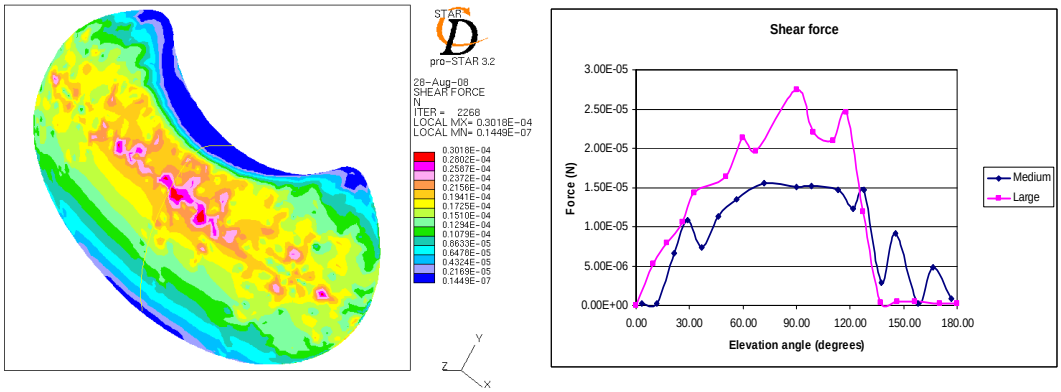

Figure 5.10: Shear force of the crescent shapes

5.4 Total Force

The previous section stated that pressure and shear forces are exerted on any object that is immerged in a non-stationary fluid. The sum of these two forces is

the total force that is applied to the surface area of the object (Eq. 5.3). Shear force stems is the result of the interaction between the moving fluid and the surface of the object (Eq. 5.2). The pressure force results from the static pressure component (Eq. 5.4). In this equation n_b represents an outward-pointing unit vector normal to the wall.

$$F_{total} = F_{shear} + F_{pressure} \tag{5.3}$$

$$F_{pressure} = P_{static} A_{boundary} n_b \tag{5.4}$$

It is very important to understand that the total force is *not* a result of the total pressure. Total pressure exists by mere definition; it can not be measured directly. It is defined as the summation of the dynamic and static pressure - since there is no dynamic pressure on a non-slip wall total pressure does not exist at that location.

When examining the hemisphere profiles from Figure 5.1 and Figure 5.8 it is clear that it resulted in the profile observed in Figure 5.11. The total force profiles for the ellipse shape (Fig. 5.12) and crescent shaped plants (Fig. 5.13) can similarly be scrutinized.

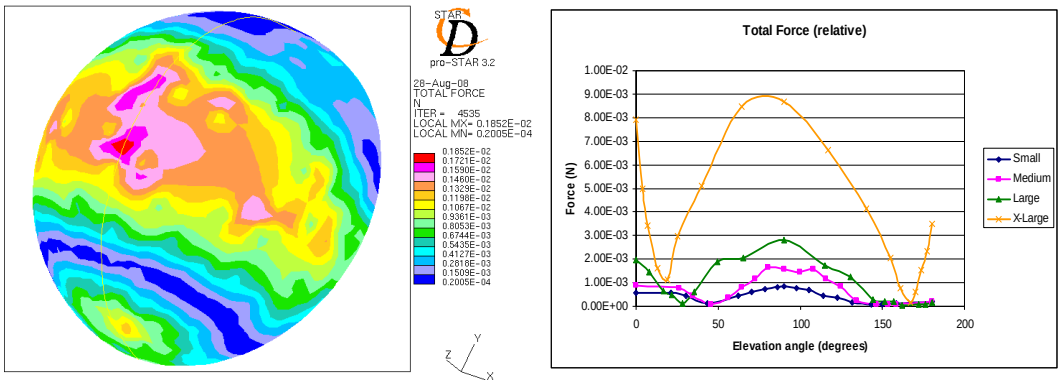

Figure 5.11: Total force of hemisphere shapes

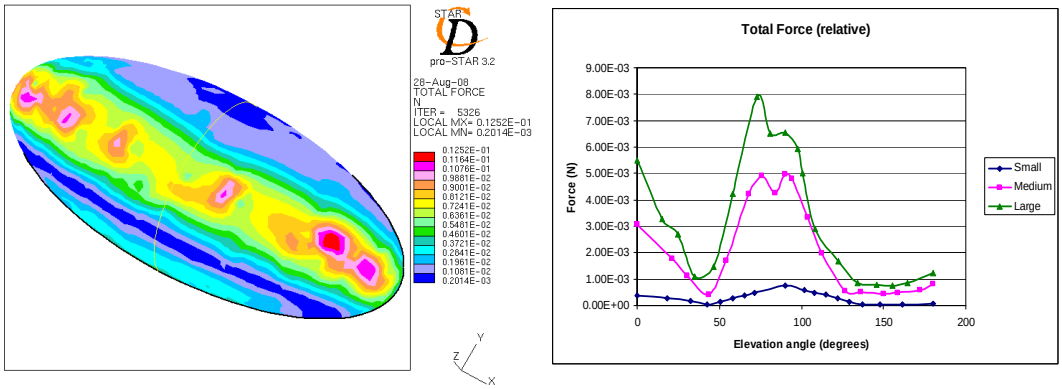

Figure 5.12: Total force of elliptical shapes

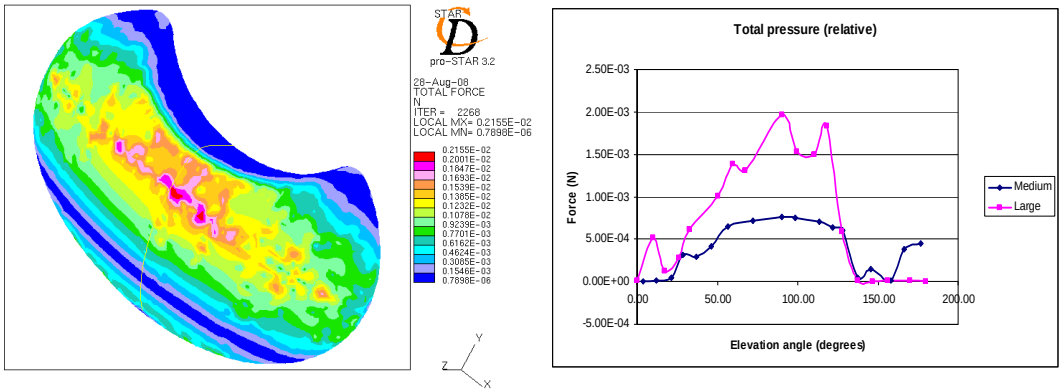

Figure 5.13: Total force of crescent shapes

5.5 Summary

In this chapter the shear force and the total force associated with each plant shape and all plant sizes were analysed. This investigation revealed that the total force is two orders of magnitude higher that the shear force. Furthermore, the magnitude of the total force is directly proportional to the size of the plant.

Three critical areas on the plant are common irrespective of shape or size: the stagnation point, the apex region and the aft section of the plant. The near-stagnation point, where the kinetic energy of the fluid flow is converted into pressure energy, is associated with the highest static pressure resulting in elevated force levels. The highest shear force is exerted in the apex region; this can be attributed to the increase in velocity over the apex of the plant. Low forces are observed at the leeward side of the plant. Shear forces and total forces are near zero in this region, making it the ideal location for the facilitated growth of *A. magellanica*.

Chapter 6 – Conclusion

The objectives of the research conducted in this thesis were four-fold:

- Conduct an airflow analysis on the most basic shape of the cushion plant and quantify the results.
- Investigate the influence of shape and size on the results obtained.
- Conduct a particle tracking analysis to determine the location of seed deposition on *A. selago*.
- Conduct a force analysis to quantify the stress and strain exerted on the plant.

In Chapter 2 experimental and numerical studies were conducted to analyse the flow over the basic shape of *A. selago*, namely a small hemisphere. The results from the wind tunnel experiments compared well with the case studies in the literature. Additional experiments using oil and powder paint was used to determine the separation point and visualize the backwards flow at the leeward section of the hemisphere. The numerical study compared the result from four independent turbulence models: k-ε high Re, k-ε RNG, k-ω SST high Re turbulence models and the k-ω SST low Re turbulence. Negligible differences between the results were indicated through comparison of static pressure and velocity distribution profiles. Is was decided that the k-ε high Re turbulence model will be used because of its good compromise between generality, economy of use and its popularity in the industrial CFD community.

Chapter 3 revealed the effect of plant shape and size on airflow. It was established that the plant, *A. selago*, is found in three shapes; hemisphere, ellipse and crescent. Nine different dimensions over the various shapes were indentified. Each shape was analysed and the patterns that emerged discussed. The windward pattern for all shapes displayed similar qualities. On the leeward side the shapes displayed distinctly different airflow patterns. Complex recirculation patterns emerged and were further visualized by means of air particle tracks.

In Chapter 4 a seed particle tracking analysis was conducted to determine the location of seed deposition on the cushion plant. The foremost number of light particle deposition of *A. magellanica* seeds on *A. selago* are found at the windward location while physical evidence clearly indicates growth primarily on the leeward position. This apparent contradiction can, however, be explained when the environmental conditions of the natural habitat are considered. Although more seeds are deposited on the windward surface, it is unlikely that any seedlings will endure the callous conditions of the micro climate and is therefore more likely to grown on the leeward side.
In Chapter 5 the shear force and the total force associated with each plant shape and all plant sizes were analysed. This investigation revealed that the total force

is two orders of magnitude higher that the shear force. Furthermore, the magnitude of the total force is directly proportional to the size of the plant. Three critical areas on the plant are common irrespective of shape or size: the stagnation point, the apex region and the leeward section of the plant.

It is recommended that an airflow analysis be conducted over the entire island. In conjunction with a spatial analysis of *A. selago* on Marion Island, this proposed study can be used to determine the influence of the wind in the distribution of the plant over the island. An airflow analysis could be of significant value to researchers who study invasion biology. The patterns in which invasive species spread over the island have long been under investigation and strong, prevailing wind should be considered as a mode of transportation. The interaction between the atmospheric airflow and the geomorphological activities on Marion Island would also become apparent in such a study.

Fluctuations in the flow field were observed when tests were conducted at low velocities in the low speed wind tunnel. The current hypothesis is that fluctuations are caused by the vibration of the hydraulic doors in front of the axial fan. It is recommended that a study be conducted to optimize the wind tunnel, not only to assure the stability of the flow field, but also to upgrade the system in general.

Although the commercial program that was applied in this project proved to be adequate, it is recommended that an open source program be used in the future. The user has more control over certain aspects of solving the partial differential equations and can introduce additional code when it is required. In the case of the Eulerian two phase flow the user had limited influence over the method of discretisation that was used. The preferred method could not be employed because the source code of the commercial program could not be altered.

References

Achenbach, E. (1972). *Experiments on the flow past spheres at very high Reynolds numbers.* Journal of Fluid Mechanics 54: 565-575.

Anthony, T.R. and Flynn, M.R. (2005). *CFD model for a 3-D inhaling mannequin: verification and validation.* Annual Occupational Hygiene 50: 157-173.

Bakić, V. (2004). *Experimental investigation of a flow around a sphere.* Thermal Science 8 (1): 63-81.

Bakić, V. and Perić, M. (2005). *Visualization of flow around sphere for Reynolds number between 22 000 and 400 000.* Thermophysics and Aeromechanics 12 (3): 307-314.

Bate, R. and Morris, J. (1995). *Global warming: Apocalypse or Hot Air.* Fuel and Energy Abstracts 36:461-461.

Boelhouwers, J., Holness, S. and Sumner, P. (2000). *Geomorphological characteristics of small debris flows on Junior's Kop, Marion Island, Maritime sub-Antarctic.* Earth Surface Processes and Landforms 25:341-352.

Boelhouwers, J., Holness, S. and Sumner P. (2003). *The maritime sub-Antarctic: a distinct periglacial environment*. Geomorphology 52:39-55.

Broecker, W.S. (2006). *Was the Younger Dryas Triggered by a Flood?*. Science 312 (5777): 1146–1148.

Chang, C.H. and Meroney, R.N. (2001). *Numerical and physical modeling of bluff body flow and dispersion in urban street canyons.* Journal of Wind Engineering and Industrial Aerodynamics 89: 1325-1334.

Chang, C.H. and Meroney, R.N. (2003). *Concentration and flow distributions in urban street canyons: wind tunnel and computational data.* Journal of Wind Engineering and Industrial Aerodynamics 89: 1325-1334.

Chown, S.L. (1997). *Antarctic biology in the mainstream?* Trends in Ecology & Evolution 12: 247.

Chown, S.L., Gaston, K.J. and Hänel, C. (2000). *Gough Island biodiversity study goes ahead.* South African Journal of Science 96, 7-8.

Cliff, R. and Gauvin, W.H. (1970). *The motion of particles in turbulent gas streams.* Proc. Chemeca 70 (1):14-28

Combrinck, M.L. (2008). Photographs were taken by the author during a field trip on Marion Island in the 2007/2008 takeover period.

Constantinescu, G. and Squires, K. (2004). *Numerical investigation of flow over a sphere in the subcritical and supercritical regimes.* Physics of Fluids 16 (5): 1449-1466.

Eskom Annual Report (2008). *Responding to climate change and limiting the impact on the environment.* Business and sustainability performance review. http://financialresults.co.za/eskom_ar2008/ar_2008/impact_environ_04.htm

Flemmer, R.L.C. and Banks C.L. (1986). *On the drag coefficient of a sphere.* Power Technology 48: 217-221.

Holness, S.D. (2003). *Sorted circles in the maritime sub-Antarctic, Marion Island*. Earth Surface Processes and Landforms 28:337-347.

Hugo, A.E., McGeoch, M.A., Marshall, D.J. and Chown, S.L. (2004). *Fine scale variation in microarthropod communities inhabiting the keystone species Azorella selago on Marion Island*. *Polar Biology* 27, 466-473.

Huntley, B.J. (1971). Vegetation. In *Marion and Prince Edward Islands: report on the South African biological and geological expeditions, 1965 - 1966* (eds E.M. van Zinderen Bakker, Sr, J.M. Winterbottom & R.A. Dyer), pp. 98-160. A.A. Balkema, Cape Town.

Huntley, B.J. (1972). Notes on the ecology of *Azorella selago* Hook. f. *Journal of South African Botany*, 38, 103-113.

Gaston, K.J., Jones, A.G., Hanel, C. and Chown, S.L. (2003). *Rates of species introduction to a remote oceanic island.* Proceedings of the Royal Society 270:1091-1098.

Kennedy, A.D. (1995). *Antarctic terrestrial ecosystem response to global environmental change.* Annual Review of Ecology and Systematics 26:683-704.

Kim, J.J. and Baik J.J. (2002). *Effects of inflow turbulence intensity on flow and pollutant dispersion in an urban street canyon.* Journal of Wind Engineering and Industrial Aerodynamics 91: 309-329.

Le Roux, P.C. (2007). Photographs were taken by Le Roux during a field trip on Marion Island in the 2006/2007 takeover period.

Le Roux, P.C. and McGeoch, M.A. (2004). *The use of size as an estimator of age in the sub-Antarctic cushion plant, Azorella selago* (Apiaceae). Arctic, Alpine and Antarctic Research 36, 608-616.

Le Roux, P.C. and McGeoch, M.A. (2007). *Changes in climate extremes, variability and signature on sub-Antarctic Marion Islan*d. Climatic Change, 86: 309-329.

Le Roux, P.C. and McGeoch, M.A. (2008). *Spatial variation in plant interactions across a severity gradient in the sub-Antarctic.* Oecologia 155(4):831-44.

Le Roux, P.C., McGeoch, M.A., Mawethe, J. and Chown, S.L. (2005). *Effects of a short-term climate change experiment on a sub-Antarctic keystone plant species.* Global Change Biology 11:1628-1639.

Lui, R., Ting, D.S.K. and Rankin, G.W. (2003). *On the generation of turbulence with a perforated plate.* Experimental Thermal and Fluid Science 28:307-316.

Marais, D.W. (2008). Figure 1.1 was printed with the permission of Mr Richard Skinner, Deputy Direction SANAP. http://marion.sanap.org.za/maps.html

McGeoch, M.A., Le Roux, P.C., Hugo, A.E. and Nyakatya, M.J. (2008) *Spatial variation in the terrestrial biotic system*. In: The Prince Edward Islands: Land-Sea Interactions in a Changing Ecosystem (eds. Chown SL, Froneman PW). African SunMedia, Stellenbosch.

Neftel, A., Moor, E., Oeschger, H. and Stauffer, B. (1985). *Evidence from polar ice cores for the increase in atmospheric CO2 in the past two centuries.* Nature 315:45-47.

Nordhaus, W.D. and Boyer, J. (2003). *Warming the World.* MIT Press.

Perry, R.H. and Chilton, C.H. (1973). *Chemical Engineer' Handbook, International Student edn.*, McGraw-Hill-Kogakusha, Tokyo, 5th edn.

Petersen, E.L., Mortensen, N.G., Landberg, M., Hojstrup, J. and Frank, H.P. (1998). *Wind Power Meteorology. Part I: Climate and Turbulence.* Wind Energy 1: 25-45.

Phiri, E. (2008). Photograph were taken by Phiri during a field trip on Marion Island in the 2007/2008 takeover period.

Raithby, G.D. and Eckert, E.R.G. (1968). *The effect of support position and turbulence intensity on the flow near the surface of a sphere.* Warme und Stoff 1:87-94.

Rouaud, O. and Havet, . (2002). *Computation of the airflow in a pitot scale clean room using k-ε turbulence models.* International Journal of Refrigeration 25: 351-361.

Schiller, L. and Naumann, Z. (1933). *A drag coefficient correlation*. *VDI-Zeitschrift* 77: 318–320.

Schlichting, H. (1968). *Boundary layer theory.* McGraw-Hill, NewYork.

Shackelton, N.J. (2000). *The 100 000-year ice-age cycle identified and found to lag temperature, carbon dioxide and orbital eccentricity.* Science 289:1897-1902.

Spalart, P.R. (2000). *Strategies for turbulence modelling and simulations.* International Journal of Heat and Fluid Flow 21: 252-263.

Stamou, A. and Katsiris, I. (2005). *Verification of a CFD model forindoor airflow and heat transfer.* Building and Environment 41: 1171-1181.

Stander, J. (2004). *The Evaluation of the flow characteristics of a newly installed test ramp.* Project Cool. CAE Stellenbosch Automotive Engineering and the Mechanical Engineering Department. Stellenbosch University. Stelenbosch.

Taneda, S. (1978). *Visual observations of the flow past a sphere at Reynolds numbers between 104 and 106.* Journal of Fluid Mechanics 85: 187-192.

Weart, S.R. (2004). *The Discovery of Global Warming.* Harvard University Press.

Weber, R. (1999). *Remarks on the definition and estimation of friction velocity.* Boundary-Layer Meteorology 93: 197-209.

White, F.M. (2006). *Viscous Fluid Flow*. McGraw-Hill, New York.

Yang, T. (2004). *CFD and field testing of a naturally ventilated full-scale building.* PhD Dissertation, University of Nottingham, United Kingdom.

Yang, W., Quan, Y., Jin, X., Tamura, Y. and Gu, M. (2008). *Influences of equilibrium atmosphere boundary layer and turbulence parameter on wind loads of low-rise buildings.* Journal of Wind Engineering and Industrial Aerodynamics 96: 2080-2092.

Appendix A: Wind Tunnel Layout

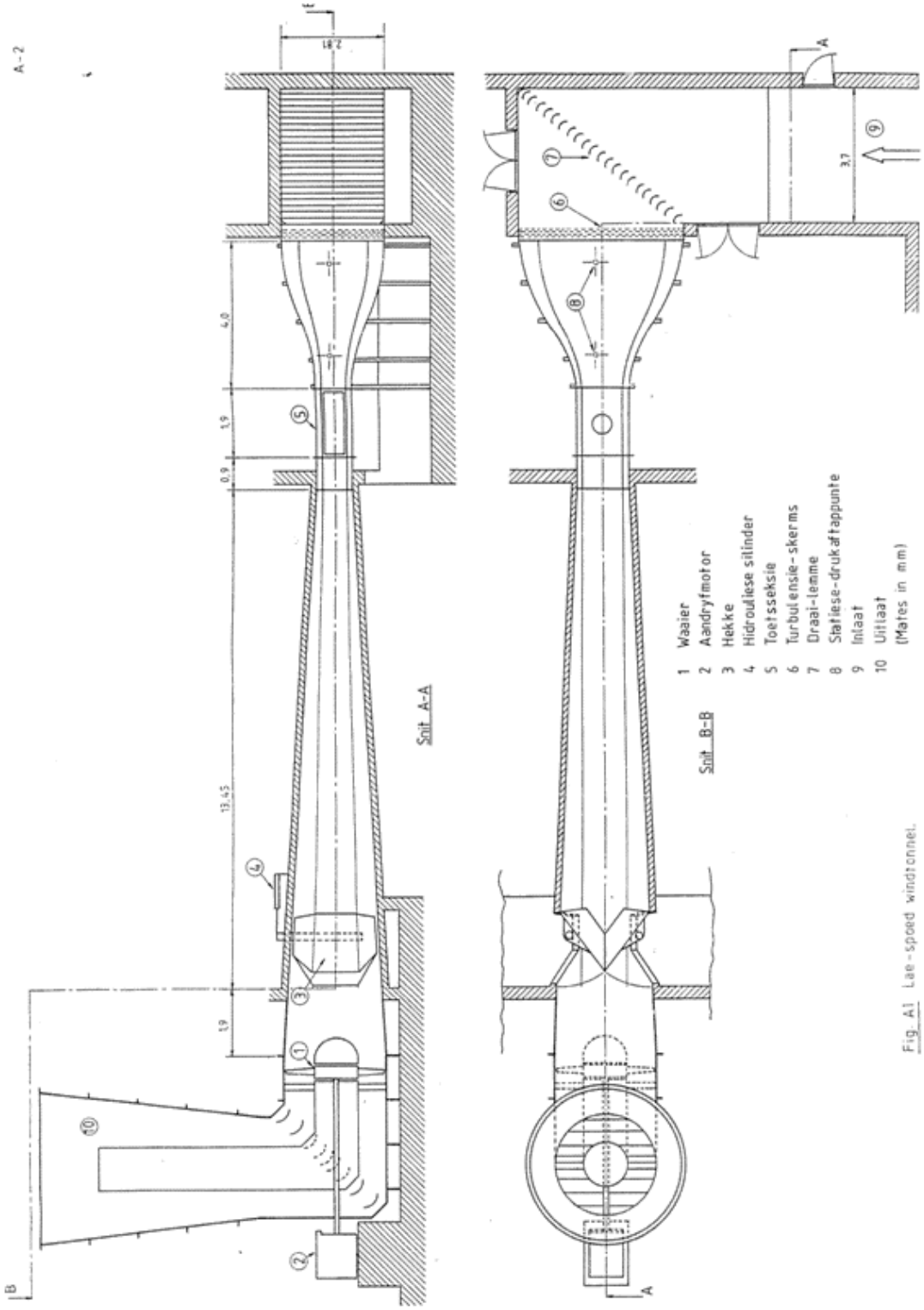

Figure A.1: Low speed wind tunnel

Appendix B: Additional Data (Chapter 2)

Table B.1: Experimental error percentages

Sensor		Occurrence	Voltage		Error %	
Transducer	Serial No.		Standard Deviation	Average	Random	Systematic
	B043316					0.08
		before test	0.0032	1.1022	0.29	
		after test	0.0030	1.1014	0.27	
	B043314					0.12
		before test	0.0033	1.0193	0.33	
		after test	0.0032	1.0181	0.32	
	B043310					0.08
		before test	0.0030	1.0330	0.29	
		after test	0.0029	1.0338	0.28	
	B043308					0.14
		before test	0.0037	0.9703	0.38	
		after test	0.0036	0.9717	0.38	
	B043312					0.03
		before test	0.0028	1.0617	0.26	
		after test	0.0027	1.0620	0.26	
	B043315					0.21
		before test	0.0029	1.0275	0.29	
		after test	0.0027	1.0297	0.26	
	B043313					0.07
		before test	0.0040	1.0612	0.38	
		after test	0.0040	1.0619	0.37	
	1527711					1.86
		before test	0.0006	0.9943	0.06	
		after test	0.0006	1.0128	0.06	
	1527732					0.68
		before test	0.0013	0.9943	0.13	
		after test	0.0006	1.0011	0.06	
Hotwire	Channel					
	one					3.72
		before test	0.0291	1.1985	2.43	
		after test	0.0059	1.2430	0.47	
	two					3.95
		before test	0.0292	1.1339	2.58	
		after test	0.0062	1.1787	0.52	

Table B.2: Pre-processing grid information

10m/s						
Designation	**Parameters and Sublayer Thickness**					
	Global	**Sphere**	**Ground**	**Inlet**	**Layers**	**Cells**
	mm	mm	mm	mm		
X1S_k-ε high-1_10	90/10	15/7	30/7	40/7	1	90708
X1S_k-ε high-2_10	80/10	12/7	20/7	30/7	1	218037
X1S_k-ε high-3_10	60/10	10/7	15/7	25/7	1	480165
X1S_RNG_10	60/10	10/7	15/7	25/7	1	480165
X1S_SST high_10	60/10	10/7	15/7	25/7	1	480165
X1S_SST low_10	80/10	15/7	20/7	30/7	15	479163
20m/s						
Designation	**Parameters and Sublayer Thickness**					
	Global	**Sphere**	**Ground**	**Inlet**	**Layers**	**Cells**
	mm	mm	mm	mm		
X1S_k-ε high-1_20	90/10	15/5	30/5	40/5	1	92866
X1S_k-ε high-2_20	80/10	12/5	20/5	30/5	1	219560
X1S_k-ε high-3_20	60/10	10/5	15/5	25/5	1	483417
X1S_RNG_20	60/10	10/5	15/5	25/5	1	483417
X1S_SST high_20	60/10	10/5	15/5	25/5	1	483417
X1S_SST low_20	60/10	15/3	20/3	30/3	15	463256
30m/s						
Designation	**Parameters and Sublayer Thickness**					
	Global	**Sphere**	**Ground**	**Inlet**	**Layers**	**Cells**
	mm	mm	mm	mm		
X1S_k-ε high-1_30	90/10	15/2	30/2	40/2	1	93408
X1S_k-ε high-2_30	80/10	12/2	20/2	30/2	1	220889
X1S_k-ε high-3_30	60/10	10/2	15/2	25/2	1	484438
X1S_RNG_30	60/11	10/3	15/3	25/3	1	484439
X1S_SST high_30	60/12	10/4	15/4	25/4	1	484440
X1S_SST low_30	80/10	15/2	20/2	30/2	15	481119

Table B.3: Solved grid information

10m/s							
Designation	**y+**			**Relaxation Factors**			
	min	**max**	**Iteration**	**Momentum**	**Pressure**	**Turb. Vis**	**Viscosity**
X1S_k-ε high-1_10	78.55	282.1	8254	0.5	0.1	0.5	0.7
X1S_k-ε high-2_10	65	257	3155	0.5	0.1	0.5	0.7
X1S_k-ε high-3_10	61	217	3841	0.5	0.1	0.5	0.7
X1S_RNG_10	61	208	3828	0.5	0.1	0.5	0.7
X1S_SST high_10	60	215	2391	0.5	0.1	0.5	0.7
X1S_SST low_10	0.9	4.2	3292	0.5	0.1	0.5	0.7
20m/s							
Designation	**y+**			**Relaxation Factors**			
	min	**max**	**Iteration**	**Momentum**	**Pressure**	**Turb. Vis**	**Viscosity**
X1S_k-ε high-1_20	95	298	2251	0.5	0.1	0.5	0.7
X1S_k-ε high-2_20	106	378	1696	0.5	0.1	0.5	0.7
X1S_k-ε high-3_20	87	357	2605	0.5	0.1	0.5	0.7
X1S_RNG_20	71	321	2759	0.5	0.1	0.5	0.7
X1S_SST high_20	60	342	2657	0.5	0.1	0.5	0.7
X1S_SST low_20	0.6	3.2	4238	0.5	0.1	0.5	0.7
30m/s							
Designation	**y+**			**Relaxation Factors**			
	min	**max**	**Iteration**	**Momentum**	**Pressure**	**Turb. Vis**	**Viscosity**
X1S_k-ε high-1_30	71	178	11624	0.5	0.1	0.5	0.7
X1S_k-ε high-2_30	86	261	4557	0.5	0.1	0.5	0.7
X1S_k-ε high-3_30	74	235	2063	0.5	0.1	0.5	0.7
X1S_RNG_30	68	243	2373	0.5	0.1	0.5	0.7
X1S_SST high_30	55	243	3893	0.5	0.1	0.5	0.7
X1S_SST low_30	0.7	2.9	4672	0.5	0.1	0.5	0.7

Sample Calculation B.1: Static Pressure Profiles and Pressure Coefficients

	Punt 1	Punt 2	Punt 3	Punt 4	Punt 5	Punt 6	Punt 7	Punt 8	Punt 9
10 m/s									
dataset 1	1.316825	1.352346	1.562049	1.716124	1.971624	1.565468	1.557646	1.568278	1.581157
dataset 2	1.31553	1.353077	1.564196	1.718798	1.973446	1.57338	1.558043	1.568039	1.581454
dataset 3	1.317798	1.35595	1.564162	1.719245	1.977761	1.576257	1.558466	1.566863	1.582325
average	1.316718	1.353791	1.563469	1.718056	1.974277	1.571702	1.558052	1.567727	1.581645
M	277.625	280.393	278.54	278.076	221.3	221.31	279.456	280.426	279.029
C	-305.115	-301.919	-300.03	-249.807	-221.62	-221.09	-294.309	-303.979	-294.771
p	60.43877	77.67454	135.4587	227.9431	215.2875	126.7433	141.0979	135.6523	146.5539
P	100298.4	100281.1	100223.3	100130.9	100143.5	100232.1	100217.7	100223.1	100212.2
Cp	0.788729	0.595452	-0.052521	-1.089612	-0.947696	0.045211	-0.115757	-0.054692	-0.176939

	Gauge	Absolute
Patmosphere	0	100358.8
Pstatic	130.775	100228
Pstagnation	41.59829	100317.2
Pdynamic1	89.17674	100269.6

$$p = Mv + C$$
$$p = 277.625 * 1.316718 - 305.115$$
$$p = 60.43877\ Pa$$

$$P_{atmosphere} = \rho_{mercury} g h_{mercury}$$
$$P_{atmosphere} = 13550 * 9.81 * 0.755$$
$$P_{atmosphere} = 100358.8\ Pa$$

$$P = P_{atmosphere} - p$$
$$P = 100358.8 - 60.43877$$
$$P = 100298.4\ Pa$$

$$C_p = \frac{P_\infty - P}{\frac{1}{2}\rho U_\infty}$$
$$C_p = \frac{130.775 - 60.43877}{89.17674}$$
$$C_p = 0.788729$$

FORTRAN userfile B.1: Velocity Inlet for 10m/s Free Stream

```
C************************************************************************
      SUBROUTINE BCDEFI(SCALAR,U,V,W,TE,ED,T,DEN,TURINT,RSU,V2P,F2P)
C     Boundary conditions at inlets
C************************************************************************
C-----------------------------------------------------------------------*
C     STAR VERSION 3.24.000                                             *
C-----------------------------------------------------------------------*
      INCLUDE 'comdb.inc'

      COMMON/USR001/INTFLG(100)

      DIMENSION SCALAR(50),RSU(6)
      LOGICAL TURINT
      INCLUDE 'usrdat.inc'
      DIMENSION SCALC(50)
      EQUIVALENCE( UDAT12(001), ICTID )
      EQUIVALENCE( UDAT04(002), DENC )
      EQUIVALENCE( UDAT04(003), EDC )
      EQUIVALENCE( UDAT02(005), PR )
      EQUIVALENCE( UDAT04(005), PRC )
      EQUIVALENCE( UDAT04(009), SCALC(01) )
      EQUIVALENCE( UDAT04(007), TC )
      EQUIVALENCE( UDAT04(008), TEC )
      EQUIVALENCE( UDAT04(059), UC )
      EQUIVALENCE( UDAT04(060), VC )
      EQUIVALENCE( UDAT04(061), WC )
      EQUIVALENCE( UDAT04(064), UCL )
      EQUIVALENCE( UDAT04(065), VCL )
      EQUIVALENCE( UDAT04(066), WCL )
      EQUIVALENCE( UDAT02(070), X )
      EQUIVALENCE( UDAT02(071), Y )
      EQUIVALENCE( UDAT02(072), Z )
C-----------------------------------------------------------------------
C
C    This subroutine enables the user to specify INLET boundary
C    conditions for U,V,W,TE,ED,T and SCALAR.
C
C     Set TURINT=.TRUE.   if turbulence intensity and length scale are
C                         specified as TE and ED respectively
C     Set TURINT=.FALSE.  if k and epsilon are specified as TE and
C                         ED respectively
C
C    ** Parameters to be returned to STAR: U,V,W,TE,ED,T,
C                                       SCALAR, DEN, TURINT
C
C    NB U,V and W are in the local coordinate-system of the
C    inlet boundary.
C
C-----------------------------------------------------------------------
C
C     Sample coding: To specify inlet values for region 1
C
      IF(IREG.EQ.1) THEN
        TURINT=.FALSE.

        if (Z.gt.0.654601) then

           U=0.45*0.45*(0.655-Z)/0.0000151
```

```
      else if (Z.gt.0.644) then

         U=0.45*((5.75*log(0.45*(0.655-Z)/0.0000151))+5.56)

      else if (Z.gt.0.011) then

         U=10

      else if (Z.gt.0.000399) then

         U=0.45*((5.75*log(0.45*Z/0.0000151))+5.56)

      else

         U=0.45*0.45*Z/0.0000151

          endif


      V=0
      W=0

      if (Z.gt.0.627) then

         TE=3/2*((((-2.95)*(0.655-Z)+0.1796)*U)**2)

      else if (Z.gt.0.607) then

         TE=3/2*((((-1.445*(0.655-Z)+0.1375)*U)**2)

      else if (Z.gt.0.048) then

         TE=3/2*((0.068*U)**2)

      else if (Z.gt.0.028) then

         TE=3/2*((((-1.445*Z)+0.1375)*U)**2)

      else
         TE=3/2*((((-2.95)*Z+0.1796)*U)**2)

      endif



      ED=(0.09**0.75)*(TE**1.5)/0.005

      T=295.65
      SCALAR(1)=SCALC(01)
      DEN=1.2
     ENDIF
C-----------------------------------------------------------------------

     RETURN
     END
C
```

FORTRAN userfile B.2: Velocity Inlet for 20m/s Free Stream

```
C**************************************************************************
      SUBROUTINE BCDEFI(SCALAR,U,V,W,TE,ED,T,DEN,TURINT,RSU,V2P,F2P)
C     Boundary conditions at inlets
C**************************************************************************
C-------------------------------------------------------------------------*
C     STAR VERSION 3.24.000                                               *
C-------------------------------------------------------------------------*
      INCLUDE 'comdb.inc'

      COMMON/USR001/INTFLG(100)

      DIMENSION SCALAR(50),RSU(6)
      LOGICAL TURINT
      INCLUDE 'usrdat.inc'
      DIMENSION SCALC(50)
      EQUIVALENCE( UDAT12(001), ICTID )
      EQUIVALENCE( UDAT04(002), DENC )
      EQUIVALENCE( UDAT04(003), EDC )
      EQUIVALENCE( UDAT02(005), PR )
      EQUIVALENCE( UDAT04(005), PRC )
      EQUIVALENCE( UDAT04(009), SCALC(01) )
      EQUIVALENCE( UDAT04(007), TC )
      EQUIVALENCE( UDAT04(008), TEC )
      EQUIVALENCE( UDAT04(059), UC )
      EQUIVALENCE( UDAT04(060), VC )
      EQUIVALENCE( UDAT04(061), WC )
      EQUIVALENCE( UDAT04(064), UCL )
      EQUIVALENCE( UDAT04(065), VCL )
      EQUIVALENCE( UDAT04(066), WCL )
      EQUIVALENCE( UDAT02(070), X )
      EQUIVALENCE( UDAT02(071), Y )
      EQUIVALENCE( UDAT02(072), Z )
C-------------------------------------------------------------------------
C
C    This subroutine enables the user to specify INLET boundary
C    conditions for U,V,W,TE,ED,T and SCALAR.
C
C     Set TURINT=.TRUE.   if turbulence intensity and length scale are
C                         specified as TE and ED respectively
C     Set TURINT=.FALSE.  if k and epsilon are specified as TE and
C                         ED respectively
C
C    ** Parameters to be returned to STAR: U,V,W,TE,ED,T,
C                                       SCALAR, DEN, TURINT
C
C    NB U,V and W are in the local coordinate-system of the
C    inlet boundary.
C
C-------------------------------------------------------------------------
C
C     Sample coding: To specify inlet values for region 1
C
      IF(IREG.EQ.1) THEN
        TURINT=.FALSE.

        if (Z.gt.0.65478) then

           U=0.81*0.81*(0.655-Z)/0.0000151
```

```
      else if (Z.gt.0.64544) then

         U=0.81*((5.75*log(0.81*(0.655-Z)/0.0000151))+5.56)

      else if (Z.gt.0.00956) then

         U=20

      else if (Z.gt.0.00022) then

         U=0.81*((5.75*log(0.81*Z/0.0000151))+5.56)

      else

         U=0.81*0.81*Z/0.0000151

          endif


      V=0
      W=0

      if (Z.gt.0.627) then

         TE=3/2*((((-4.025*(0.655-Z))+0.2352)*U)**2)

      else if (Z.gt.0.607) then

         TE=3/2*((((-2.125*(0.655-Z)+0.182))*U)**2)

      else if (Z.gt.0.048) then

         TE=3/2*((0.08*U)**2)

      else if (Z.gt.0.028) then

         TE=3/2*((((-2.125*Z)+0.182)*U)**2)

      else
         TE=3/2*((((-4.025*Z)+0.2352)*U)**2)

      endif



      ED=(0.09**0.75)*(TE**1.5)/0.005

      T=295.65
      SCALAR(1)=SCALC(01)
      DEN=1.2
     ENDIF
C-----------------------------------------------------------------------

     RETURN
     END
C
```

FORTRAN userfile B.3: Velocity Inlet for 30m/s Free Stream

```
C************************************************************************
      SUBROUTINE BCDEFI(SCALAR,U,V,W,TE,ED,T,DEN,TURINT,RSU,V2P,F2P)
C     Boundary conditions at inlets
C************************************************************************
C-----------------------------------------------------------------------*
C     STAR VERSION 3.24.000                                             *
C-----------------------------------------------------------------------*
      INCLUDE 'comdb.inc'

      COMMON/USR001/INTFLG(100)

      DIMENSION SCALAR(50),RSU(6)
      LOGICAL TURINT
      INCLUDE 'usrdat.inc'
      DIMENSION SCALC(50)
      EQUIVALENCE( UDAT12(001), ICTID )
      EQUIVALENCE( UDAT04(002), DENC )
      EQUIVALENCE( UDAT04(003), EDC )
      EQUIVALENCE( UDAT02(005), PR )
      EQUIVALENCE( UDAT04(005), PRC )
      EQUIVALENCE( UDAT04(009), SCALC(01) )
      EQUIVALENCE( UDAT04(007), TC )
      EQUIVALENCE( UDAT04(008), TEC )
      EQUIVALENCE( UDAT04(059), UC )
      EQUIVALENCE( UDAT04(060), VC )
      EQUIVALENCE( UDAT04(061), WC )
      EQUIVALENCE( UDAT04(064), UCL )
      EQUIVALENCE( UDAT04(065), VCL )
      EQUIVALENCE( UDAT04(066), WCL )
      EQUIVALENCE( UDAT02(070), X )
      EQUIVALENCE( UDAT02(071), Y )
      EQUIVALENCE( UDAT02(072), Z )
C-----------------------------------------------------------------------
C
C    This subroutine enables the user to specify INLET boundary
C    conditions for U,V,W,TE,ED,T and SCALAR.
C
C     Set TURINT=.TRUE.   if turbulence intensity and length scale are
C                         specified as TE and ED respectively
C     Set TURINT=.FALSE.  if k and epsilon are specified as TE and
C                         ED respectively
C
C    ** Parameters to be returned to STAR: U,V,W,TE,ED,T,
C                                       SCALAR, DEN, TURINT
C
C    NB U,V and W are in the local coordinate-system of the
C    inlet boundary.
C
C-----------------------------------------------------------------------
C
C     Sample coding: To specify inlet values for region 1
C
      IF(IREG.EQ.1) THEN
        TURINT=.FALSE.

        if (Z.gt.0.654859) then

           U=1.27*1.27*(0.655-Z)/0.0000151
```

```
      else if (Z.gt.0.64618) then

         U=1.27*((5.75*log(1.27*(0.655-Z)/0.0000151))+5.56)

      else if (Z.gt.0.00882) then

         U=30

      else if (Z.gt.0.000141) then

         U=1.27*((5.75*log(1.27*Z/0.0000151))+5.56)

      else

         U=1.27*1.27*Z/0.0000151

          endif


      V=0
      W=0

      if (Z.gt.0.627) then

         TE=3/2*(((-5.75*(Z-0.655)+0.2907)*U)**2)

      else if (Z.gt.0.607) then

         TE=3/2*(((-1.44*(Z-0.655)+0.17)*U)**2)

      else if (Z.gt.0.048) then

         TE=3/2*((0.1009*U)**2)

      else if (Z.gt.0.028) then

         TE=3/2*(((-1.44*(Z)+0.17)*U)**2)

      else
         TE=3/2*(((-5.75*(Z)+0.2907)*U)**2)

      endif



      ED=(0.09**0.75)*(TE**1.5)/0.005

      T=295.65
      SCALAR(1)=SCALC(01)
      DEN=1.2
     ENDIF
C-----------------------------------------------------------------------

     RETURN
     END
C
```

Appendix C: Additional Figures (Chapter 2)

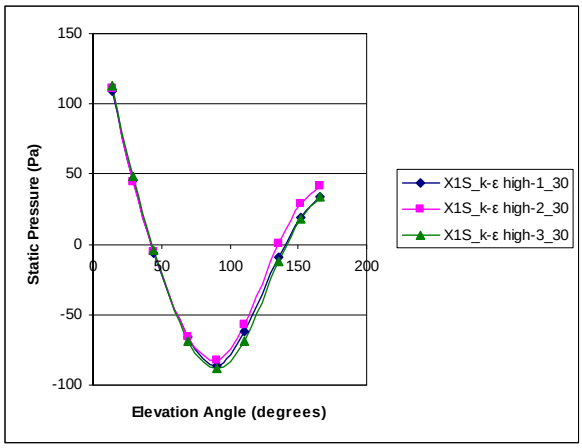

Figure C.1: Grid independence through static pressure: 10 m/s

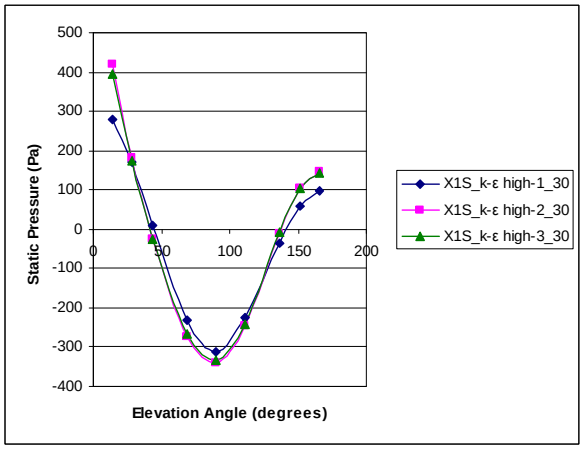

Figure C.2: Grid independence through static pressure: 20 m/s

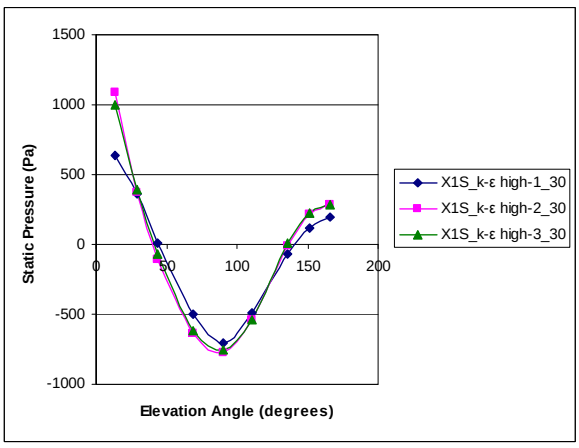

Figure C.3: Grid independence through static pressure: 30 m/s

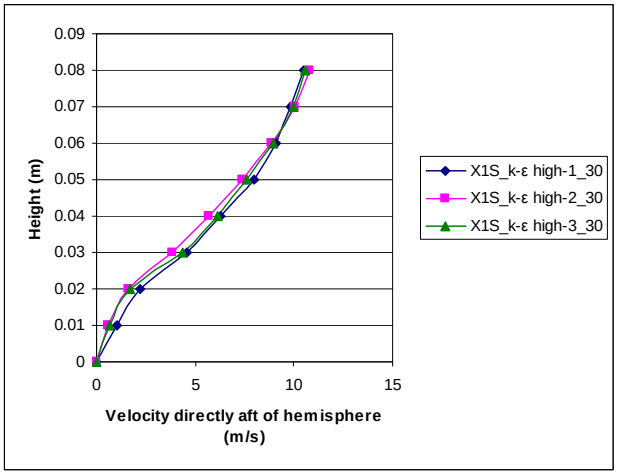

Figure C.4: Grid independence through velocity profile directly aft: 10 m/s

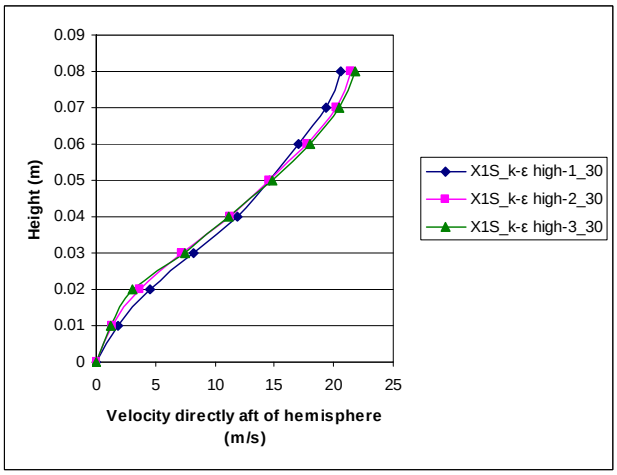

Figure C.5: Grid independence through velocity profile directly aft: 20 m/s

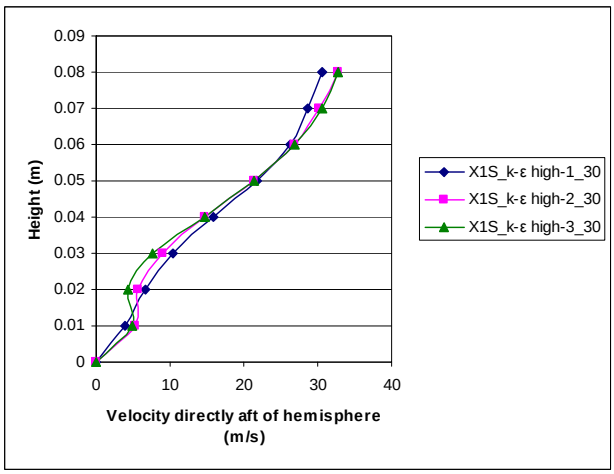

Figure C.6: Grid independence through velocity profile directly aft: 30 m/s

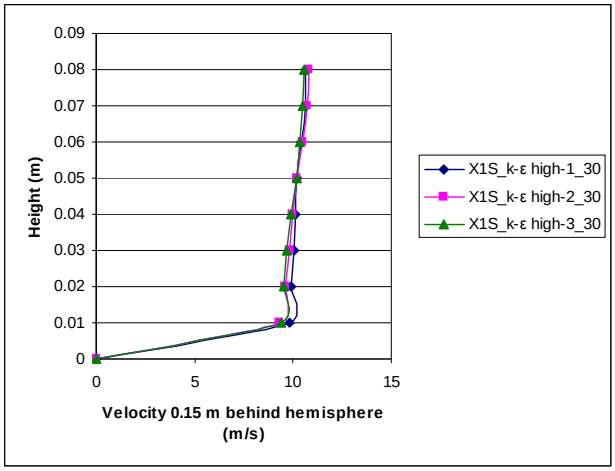

Figure C.7: Grid independence through velocity profile in the wake: 10 m/s

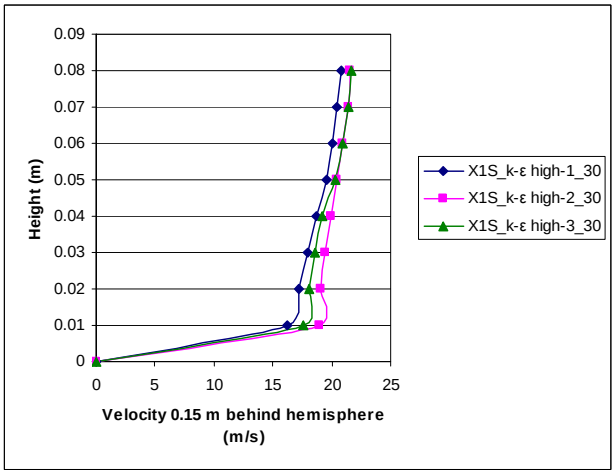

Figure C.8: Grid independence through velocity profile in the wake: 20 m/s

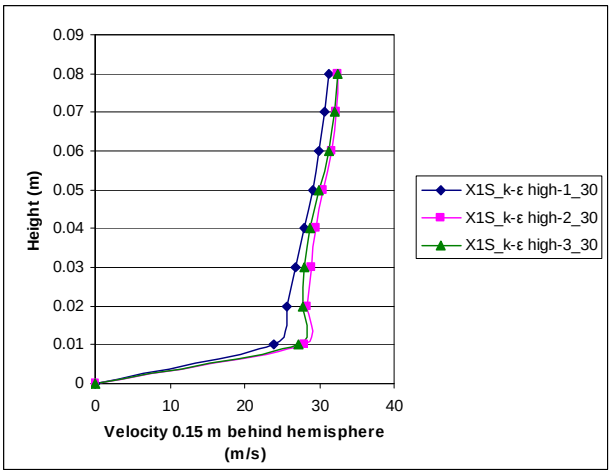

Figure C.9: Grid independence through velocity profile in the wake: 30 m/s

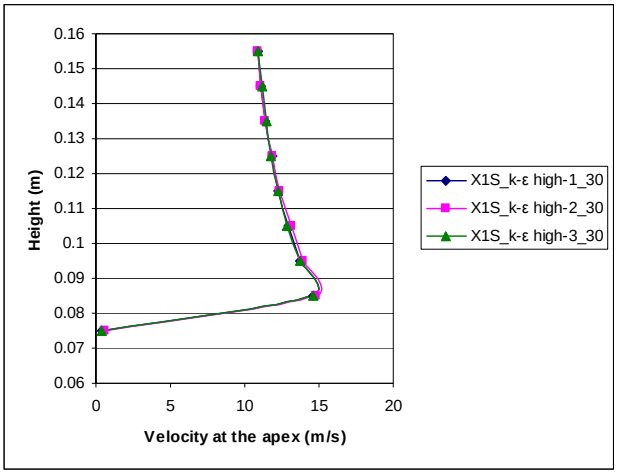

Figure C.10: Grid independence through velocity profile at the apex: 10 m/s

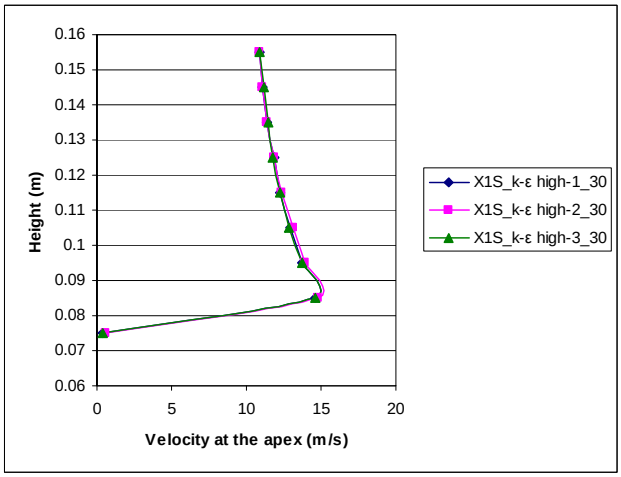

Figure C.11: Grid independence through velocity profile at the apex: 20 m/s

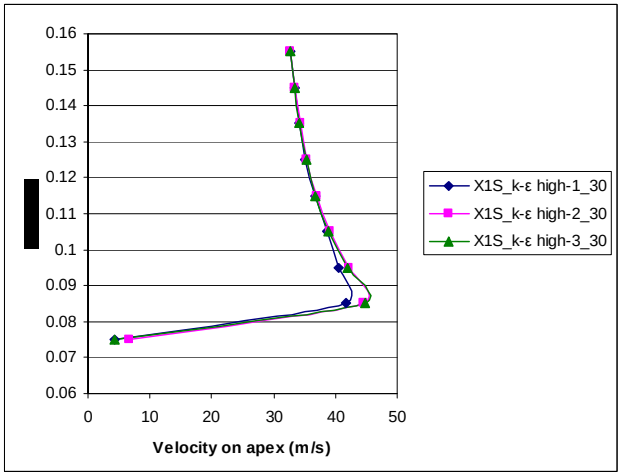

Figure C.12: Grid independence through velocity profile at the apex: 30 m/s

Appendix D: Additional Data (Chapter 3)

Table D.1: Velocity measurement on Marion Island

Average Velocity Measurements						
	Skua-Ridge			Tafelberg		
z (m)	Dataset 1 u1 (m/s)	Dataset 2 u2 (m/s)	Dataset 3 u3 (m/s)	Dataset 1 u1 (m/s)	Dataset 2 u2 (m/s)	Dataset 3 u3 (m/s)
0.2	3.855	8.362	6.863	4.357	7.918	7.327
0.47	4.949	10.256	7.773	5.058	9.278	8.940
1.4	6.55	12.863	10.095	6.635	11.533	11.367

Table D.2: Linearization data for velocity measurements on Marion Island

Skua-Ridge Data						
	ln(m)	**u*** (m/s)	**ln(b)**	**zo** (m)	**R*R**	**δ'** (m)
Dataset 1	0.719	0.57	-4.356	0.012827	0.9986	1.32E-04
Dataset 2	0.432	0.95	-5.204	0.005494	0.9996	7.95E-05
Dataset 3	0.576	0.712	-5.425	0.0044	0.969	1.06E-04
Tafelberg Data						
	ln(m)	**u*** (m/s)	**ln(b)**	**zo** (m)	**R*R**	**δ'**
Dataset 1	0.827	0.496	-5.099	0.0061	0.9782	1.52E-04
Dataset 2	0.533	0.77	-5.778	0.003094	0.9949	9.81E-05
Dataset 3	0.479	0.856	-5.089	0.006162	0.9979	8.82E-05

Table D.3: Plant and control volume dimensions

	Dimensions			Control Volume (CV)			Position in CV	
	Φo mm	Φi mm	Height mm	Length mm	Width mm	Height mm	X mm	Y mm
SPHERE								
Small	150	150	75	2250	2250	1500	1125	825
Medium	300	300	150	4000	4500	1500	2000	1645
Large	600	600	170	8000	6000	1000	4000	2525
Extra Large	900	900	180	10000	10000	1000	5000	3990
ELLIPSE								
Small	300	190	95	4000	2850	1000	1998	1045
Medium	600	290	145	6000	4350	1000	3000	1755
Large	900	380	190	6000	5700	1000	3000	2000
CRESCENT								
Medium	600	400	120	5000	3000	1000	2500	1343
Large	900	400	140	5000	3500	1000	2500	1500

Table D.4: Grid generation data for hemisphere shape

SMALL SPHERE

Designation	Global	Sublayers		Parameters		Fluid Cells
		Ground mm	Sphere mm	Ground mm	Sphere mm	
X3S_080111_s	4.0%	4	5	10	25	412114
X3S_080126_s	3.0%	4	5	8	20	899910
X3S_080128_s	3.0%	8	8	6	18	1089767

MEDIUM SPHERE

Designation	Global	Sublayers		Parameters		Fluid Cells
		Ground mm	Sphere mm	Ground mm	Sphere mm	
X3S_080203_m	5.0%	15	15	15	30	667401
X3S_080204_m	4.5%	10	10	10	25	923110
X3S_080304_m	4.5%	8	8	7	20	923181

LARGE SPHERE

Designation	Global	Sublayers		Parameters		Fluid Cells
		Ground mm	Sphere mm	Ground mm	Sphere mm	
X3S_080117_l	3.5%	8	8	30	60	336735
X3S_080118_l	3.5%	8	8	20	50	515967
X3S_080125_l	3.0%	8	8	15	40	976936

X-LARGE SPHERE

Designation	Global	Sublayers		Parameters		Fluid Cells
		Ground mm	Sphere mm	Ground mm	Sphere mm	
X3S_080204_x	3.0%	10	10	50	100	247623
X3S_080205_x	2.5%	8	8	40	80	473120
X3S_080310_x	2.5%	7	7	30	70	609181

Table D.5: Grid generation data for elliptical shape

SMALL ELLIPSE

Designation	Global	Sublayers		Parameters		Fluid Cells
		Ground mm	Sphere mm	Ground mm	Sphere mm	
X3S_071126_s	4.0%	4	5	10	25	705463
X3S_080125_s	3.5%	8	9	8	20	1074389
X3S_080128_s	3.0%	9	9	6	18	1130265

MEDIUM ELLIPSE

Designation	Global	Sublayers		Parameters		Fluid Cells
		Ground mm	Sphere mm	Ground mm	Sphere mm	
X3S_080111_m	4.0%	10	10	25	45	378603
X3S_080118_m	3.5%	8	8	20	35	711999
X3S_080128_m	3.0%	8	9	15	30	1157652

LARGE ELLIPSE

Designation	Global	Sublayers		Parameters		Fluid Cells
		Ground mm	Sphere mm	Ground mm	Sphere mm	
X3S_080129_l	3.5%	8	8	40	60	302285
X3S_080203_l	3.0%	6	8	25	50	499544
X3S_080310_l	3.0%	7	7	20	45	635122

Table D.6: Grid generation for crescent shape

MEDIUM CRESCENT						
Designation	**Global**	**Sublayers**		**Parameters**		**Fluid Cells**
		Ground mm	**Sphere** mm	**Ground** mm	**Sphere** mm	
X3B_071121_m	3.5%	4	5	10	30	753791
X3B_080125_m	3.5%	8	8	8	20	1169472
X3B_080128_m	3.0%	12	10	8	20	1177293
LARGE CRESCENT						
Designation	**Global**	**Sublayers**		**Parameters**		**Fluid Cells**
		Ground mm	**Sphere** mm	**Ground** mm	**Sphere** mm	
X3B_080130_l	4.0%	8	12	10	30	430619
X3B_080203_l	4.0%	10	12	15	35	528166
X3B_080310_l	4.0%	10	15	15	30	778973

Table D.7: Solving data for crescent shape

MEDIUM CRESCENT							
Designation				**Relaxation Factors**			
	y+ min	**y+ max**	**Itteration**	**Momentum**	**Pressure**	**Turb. Viscosity**	**Viscosity**
X3B_071121_m	2.075	119.1	2232	0.5	0.5	0.3	0.6
X3B_080125_m	3.041	176.7	3836	0.7	0.3	0.3	0.7
X3B_080128_m	3.102	275.5	10000	0.7	0.3	0.4	1.0
LARGE CRESCENT							
Designation				**Relaxation Factors**			
	y+ min	**y+ max**	**Itteration**	**Momentum**	**Pressure**	**Turb. Viscosity**	**Viscosity**
X3B_080130_l	2.575	244.8	10000	0.7	0.3	0.7	1.0
X3B_080203_l	4.721	292.7	10000	0.7	0.3	0.7	1.0
X3B_080310_l	4.012	303.3	2268	0.7	0.3	0.7	1.0

Table D.8: Solving data for elliptical shape

SMALL OVAL

Designation				Relaxation Factors			
	y+ min	y+ max	Itteration	Momentum	Pressure	Turb. Viscosity	Viscosity
X3S_071126_s	12.83	119.90	2167	0.60	0.60	0.30	0.70
X3S_080125_s	31.41	195.30	3455	0.70	0.30	0.30	0.70
X3S_080128_s	27.11	235.80	14507	0.30	0.01	0.70	1.00

MEDIUM OVAL

Designation				Relaxation Factors			
	y+ min	y+ max	Itteration	Momentum	Pressure	Turb. Viscosity	Viscosity
X3S_080111_m	51.94	245.90	3025	0.50	0.50	0.30	0.50
X3S_080118_m	33.04	200.30	3888	0.70	0.30	0.30	0.70
X3S_0080128_m	24.56	201.60	8627	0.30	0.01	0.70	1.00

LARGE OVAL

Designation				Relaxation Factors			
	y+ min	y+ max	Itteration	Momentum	Pressure	Turb. Viscosity	Viscosity
X3S_080129_l	36.34	205.10	3676	0.70	0.30	0.70	1.00
X3S_080203_l	19.35	195.70	3372	0.70	0.30	0.70	1.00
X3S_080310_l	23.70	182.30	5326	0.50	0.01	0.70	1.00

Table D.9: Solving data for hemisphere shape

SMALL SPHERE							
Designation				Relaxation Factors			
	y+ min	y+ max	Itteration	Momentum	Pressure	Turb. Viscosity	Viscosity
X3S_080111_s	29.28	121.7	4129	0.5	0.5	0.4	0.6
X3S_080126_s	25.98	117.8	3417	0.5	0.5	0.3	0.7
X3S_080128_s	29.84	183.7	3179	0.7	0.3	0.7	0.7
MEDIUM SPHERE							
				Relaxation Factors			
Designation	y+ min	y+ max	Itteration	Momentum	Pressure	Turb. Viscosity	Viscosity
X3S_080203_m	46.66	333.6	2058	0.7	0.3	0.7	1.0
X3S_080204_m	39.17	232.1	2243	0.6	0.2	0.7	0.7
X3S_080304_m	30.74	139.3	4535	0.7	0.3	0.3	0.7
LARGE SPHERE							
Designation				Relaxation Factors			
	y+ min	y+ max	Itteration	Momentum	Pressure	Turb. Viscosity	Viscosity
X3S_080117_l	37.67	174.9	1118	0.7	0.3	0.5	0.7
X3S_080118_l	30.39	175.30	3566	0.7	0.3	0.7	0.7
X3S_080125_l	43.14	173.90	1000	0.5	0.0	0.4	1.0
X-LARGE SPHERE							
Designation				Relaxation Factors			
	y+ min	y+ max	Itteration	Momentum	Pressure	Turb. Viscosity	Viscosity
X3S_080204_x	54.56	210.5	6913	0.7	0.3	0.7	1.0
X3S_080205_x	40.48	171.70	10000	0.7	0.3	0.7	1.0
X3S_080310_x	39.71	156.50	2729	0.5	0.01	0.7	1.0

Appendix E: Additional Figures (Chapter 3)

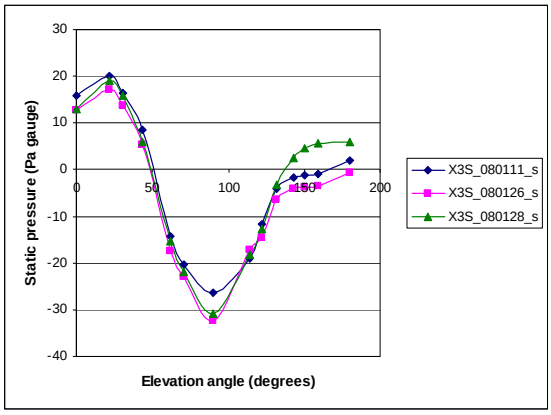

Figure E.1: Small hemisphere grid independence

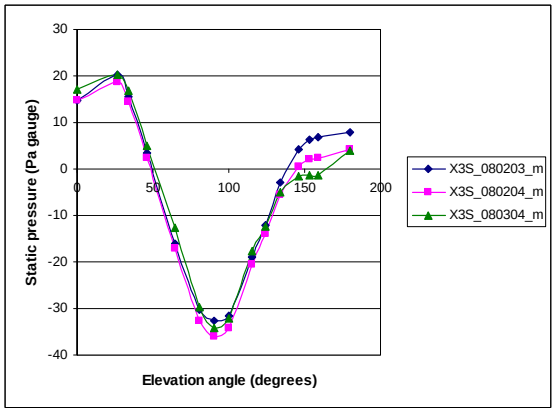

Figure E.2: Medium hemisphere grid independence

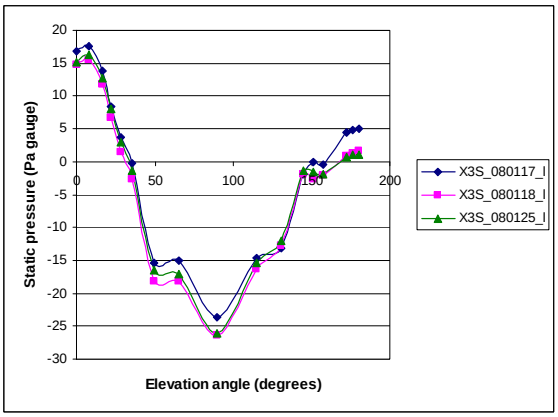

Figure E.3: Large hemisphere grid independence

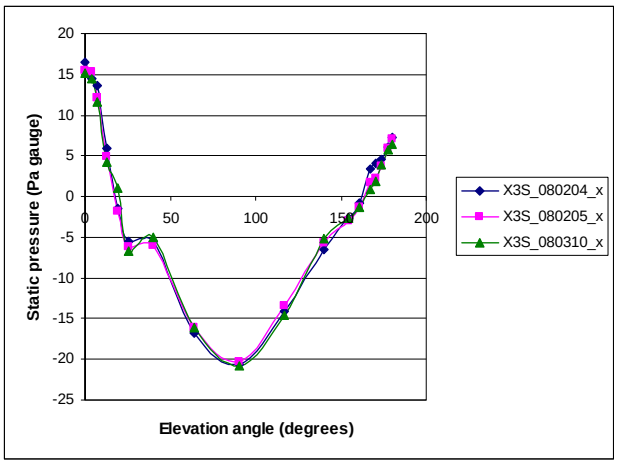

Figure E.4: Extra large hemisphere grid independence

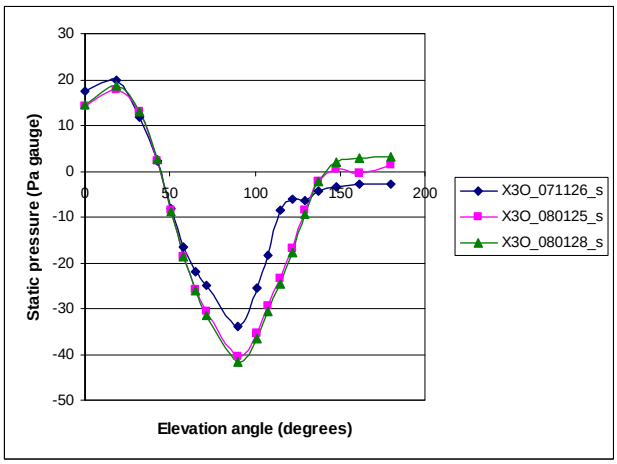

Figure E.5: Small ellipse grid independence

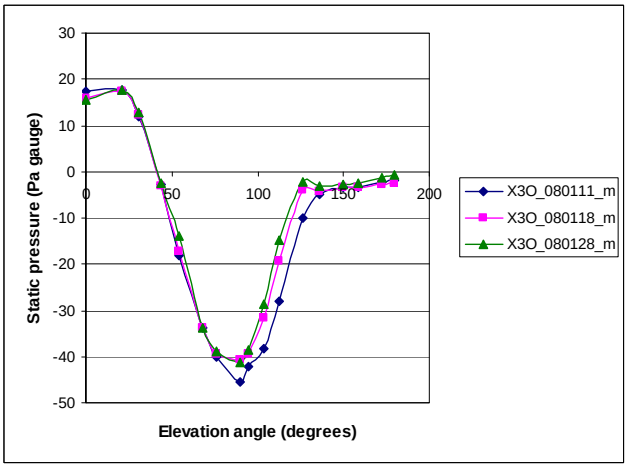

Figure E.6: Medium ellipse grid independence

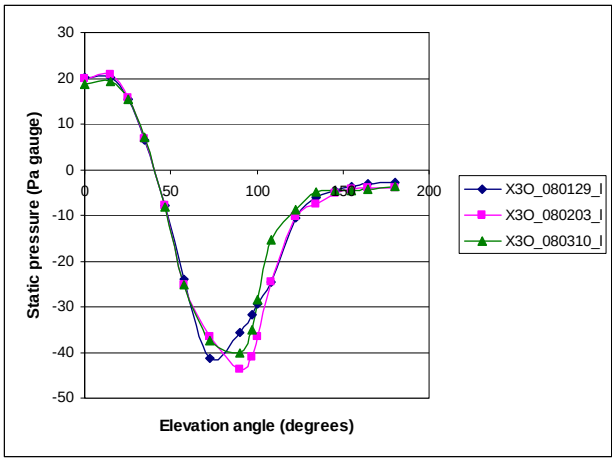

Figure E.7: Large ellipse grid independence

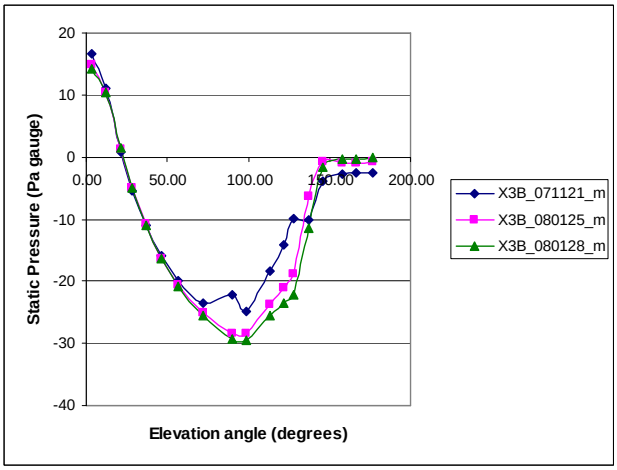

Figure E.8: Medium crescent shape grid independence

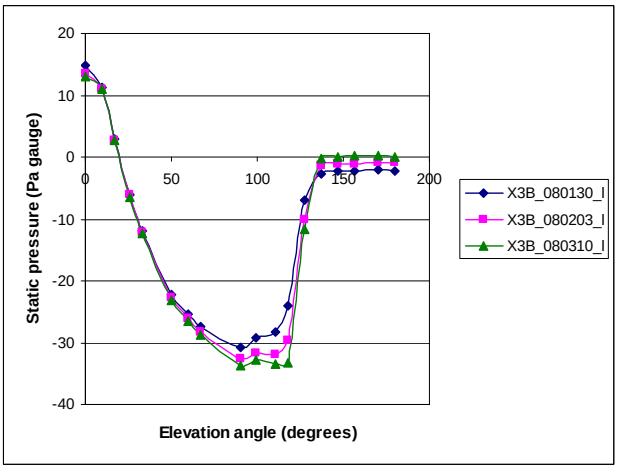

Figure E.9: Large crescent shape grid independence

Appendix F: Calculated Particle Terminal Velocity

```
% This program determines the terminal velocity of a sphere

clc
clear all
close all

% Variables

   pi          = 22/7
   d           = 3/1000;           %m
   rho_air     = 1.2;              %kg/m^3
   mass        = 0.28899;          %mg
   g           = 9.81;             %m/s^2
   mu          = 1.81*10^-5;       %Ns/m^2


% Pre-Calculations

   V           = pi/6*(d^3);
   gamma       = mass*10e-6*g/V;

% Initial values

  Cd           =0.4;

% Calculations

   i=0;
   j=1;
   while i==0;

         a = gamma*(4/3)*d;
         b = rho_air;
         Vo = sqrt(a/(b*Cd));
         Re = rho_air*Vo*d/mu


         % Cliff and Gauvin 1970

            a = (24/Re)*(1+0.15*(Re^0.687));
            b = 0.42/(1+4.25*(10^4)*(Re^-1.16));
            Cd_new = a+b;
```

```
        diff = abs(Cd_new-Cd);

            if diff < 0.00001
               i =1;
            end

            Cd = Cd_new;
            j=j+1;

               AA(j) = [Vo];
               BB(j) = [Cd];
end

CC(:,1)=AA;
CC(:,2)=BB;

disp('    Vo       Cd');
disp(CC);
```

Appendix G: *Agrostis Magellanica* Experiments

The average mass of a seed was determined to be 0.28899 mg. The seed volume is approximated as a sphere with a diameter of 3 mm. The density is the average mass of the seed divided by the sphere volume.

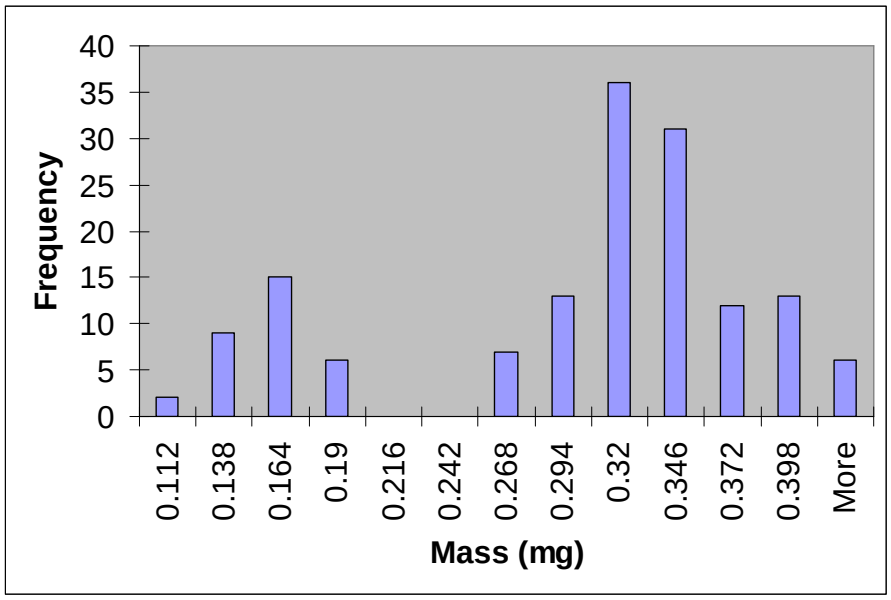

Figure G.1: Seed weight distribution of 150 samples of *Agrostis magellanica* seeds

$$V = \frac{4}{3}\pi r^3$$

$$V = \frac{4}{3}\pi(1.5E-03)^3$$

$$V = 1.414E-08\, m^3$$

$$\rho = \frac{mass}{volume}$$

$$\rho = \frac{0.28899E-06}{1.414E-08}$$

$$\rho = 20.438\, kg/m^3$$

Table G.1: Equipment used in drop test experiment

	Item	Serial number	Manufacturer
1	Precisa Balance 40SM-200A	73464	PAG Oerlikon AG Zurich Switzerland
2	Serial RS232 Connection Cable		
3	Tube Diameter 12 mm Length 3.5 m		

Appendix H: Single Phase and Multi Phase Graphs

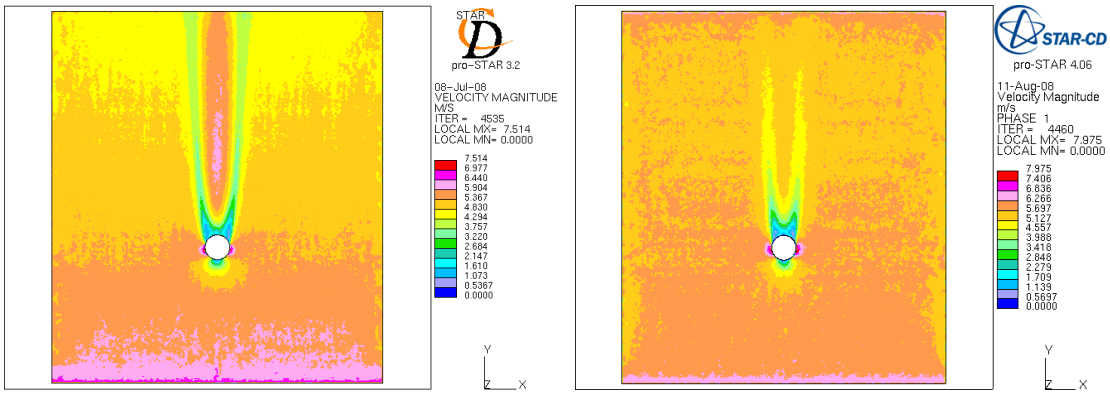

Figure H.1: Velocity magnitude at a horizontal plane 16.5 mm from ground level

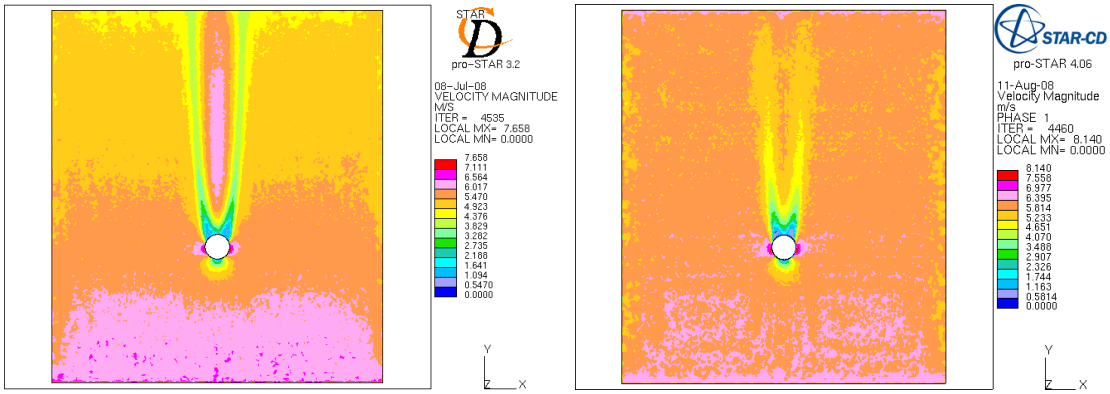

Figure H.2: Velocity magnitude at a horizontal plane 24 mm from ground level

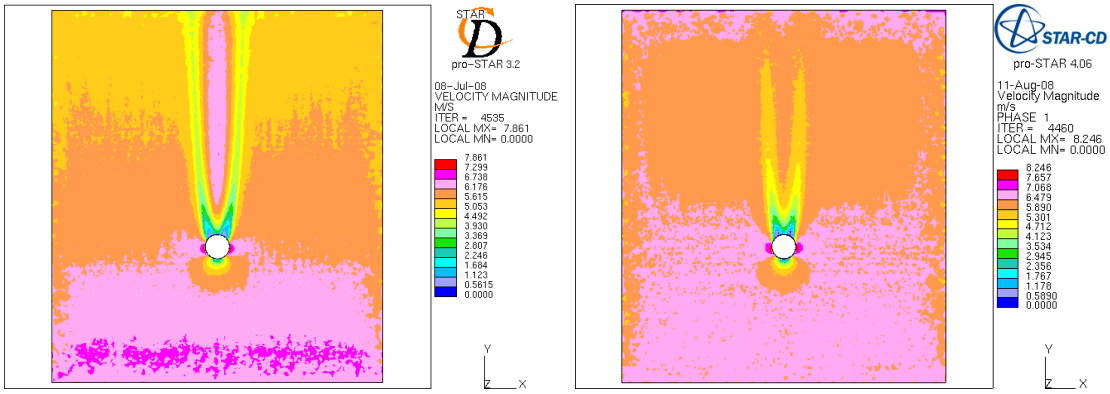

Figure H.3: Velocity magnitude at a horizontal plane 33 mm from ground level

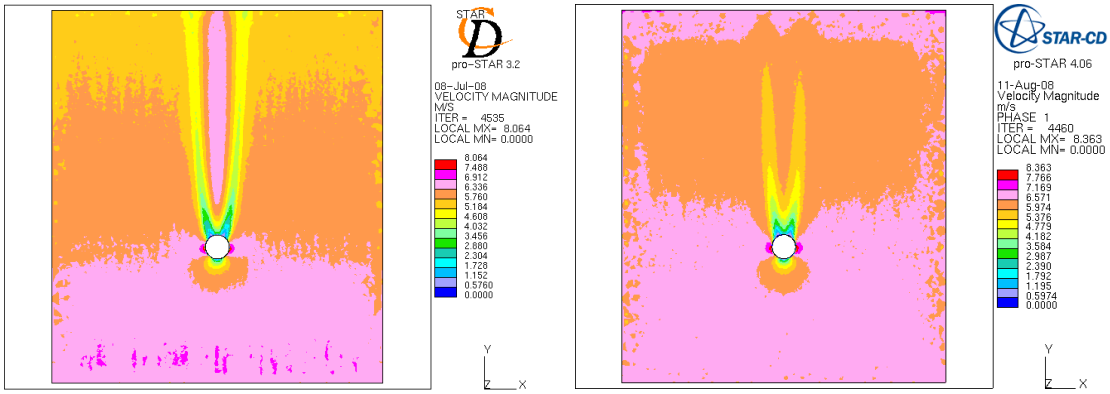

Figure H.4: Velocity magnitude at a horizontal plane 40.5 mm from ground level

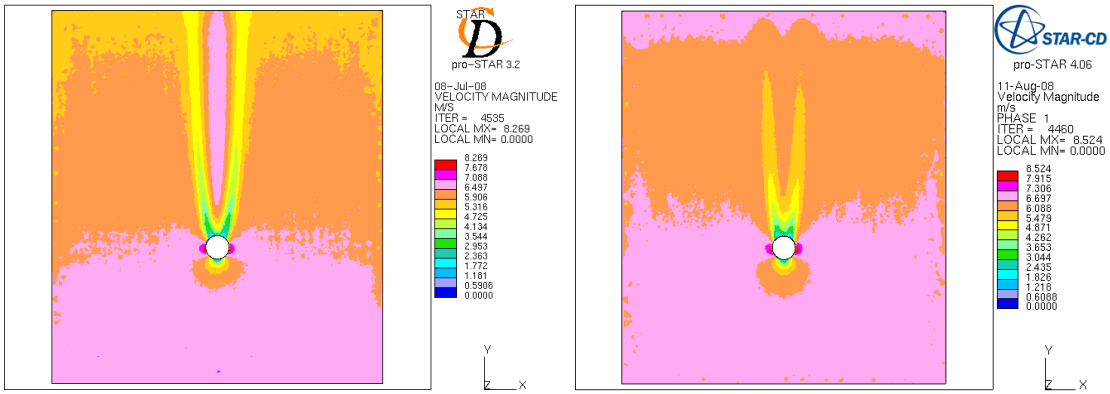

Figure H.5: Velocity magnitude at a horizontal plane 49.5 mm from ground level

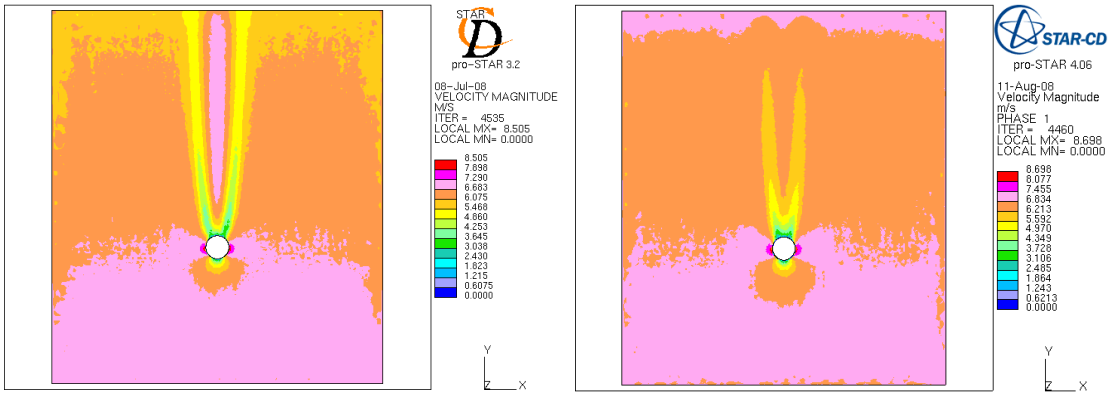

Figure H.6: Velocity magnitude at a horizontal plane 57 mm from ground level

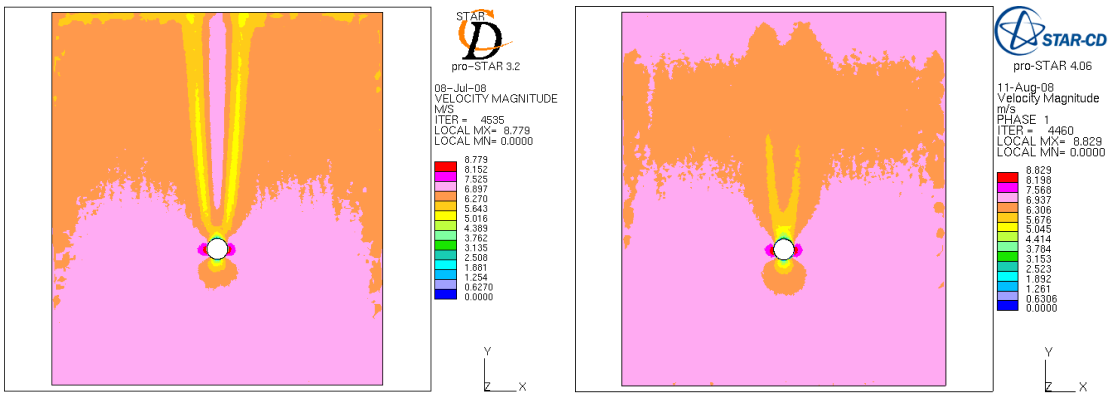

Figure H.7: Velocity magnitude at a horizontal plane 82.5 mm from ground level

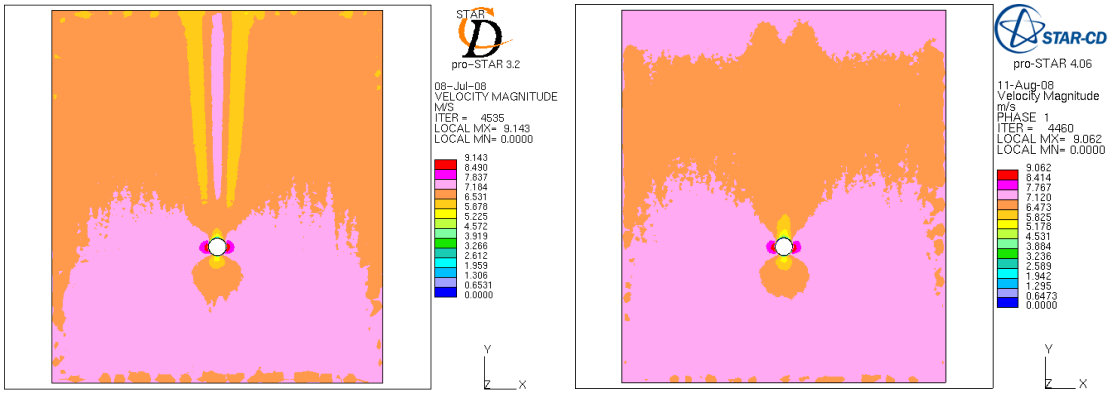

Figure H.8: Velocity magnitude at a horizontal plane 106.5 mm from ground level

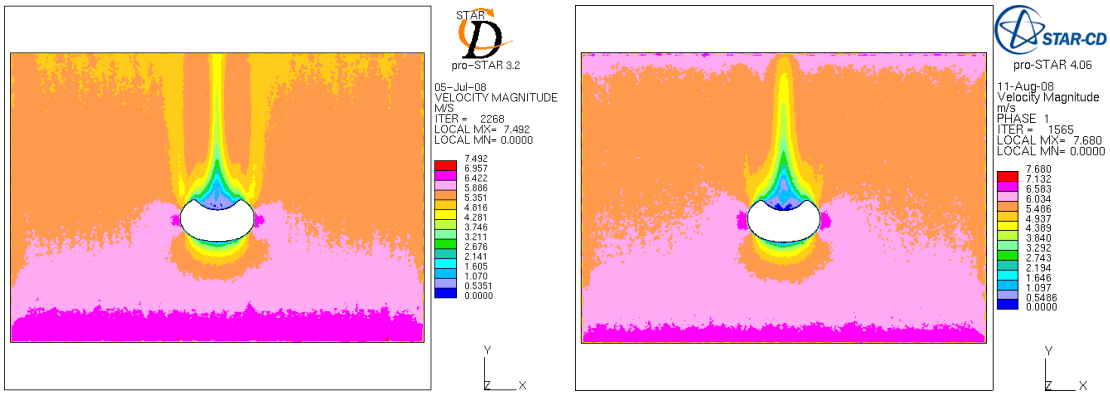

Figure H.9: Velocity magnitude at a horizontal plane 16 mm from ground level

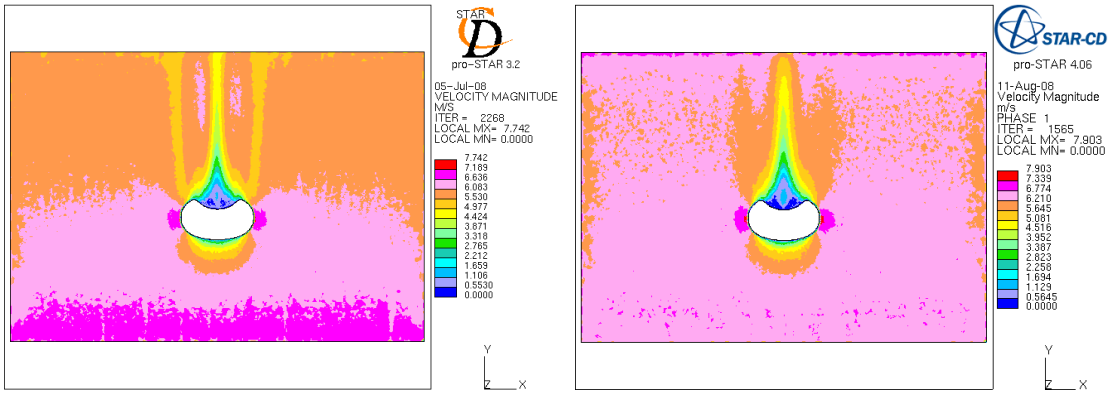

Figure H.10: Velocity magnitude at a horizontal plane 22 mm from ground level

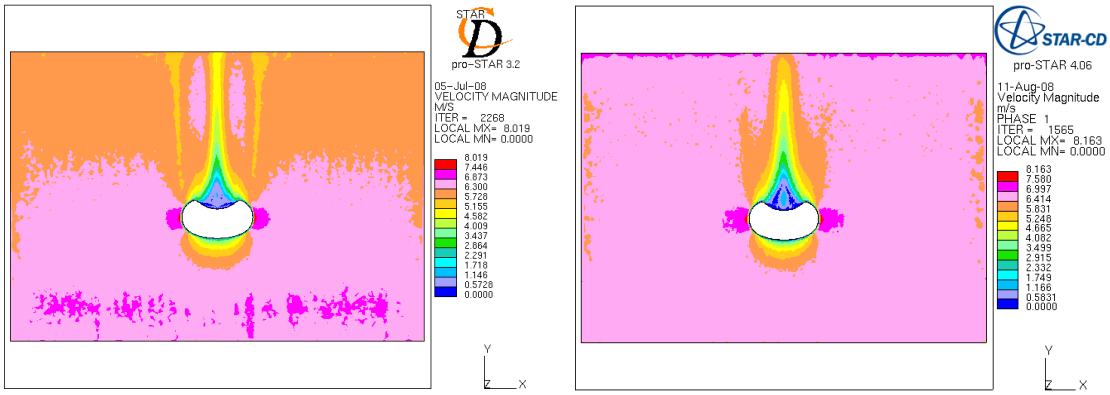

Figure H.11: Velocity magnitude at a horizontal plane 33 mm from ground level

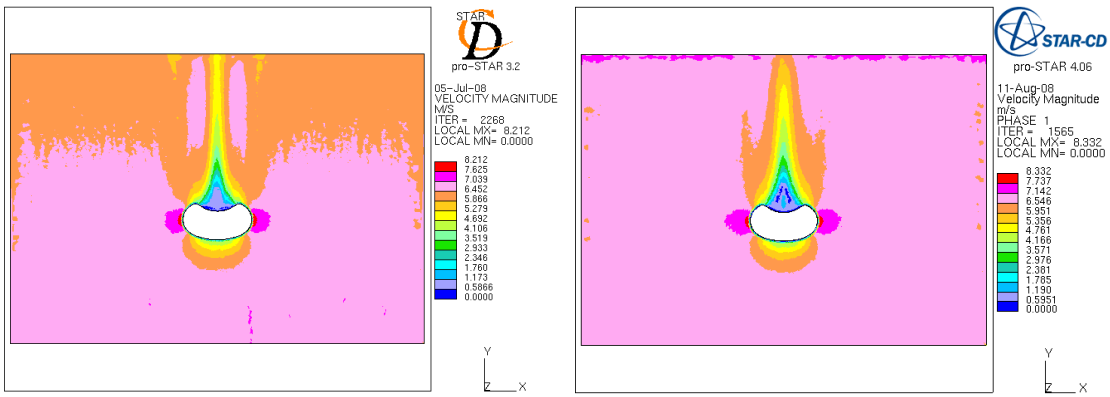

Figure H.12: Velocity magnitude at a horizontal plane 44 mm from ground level

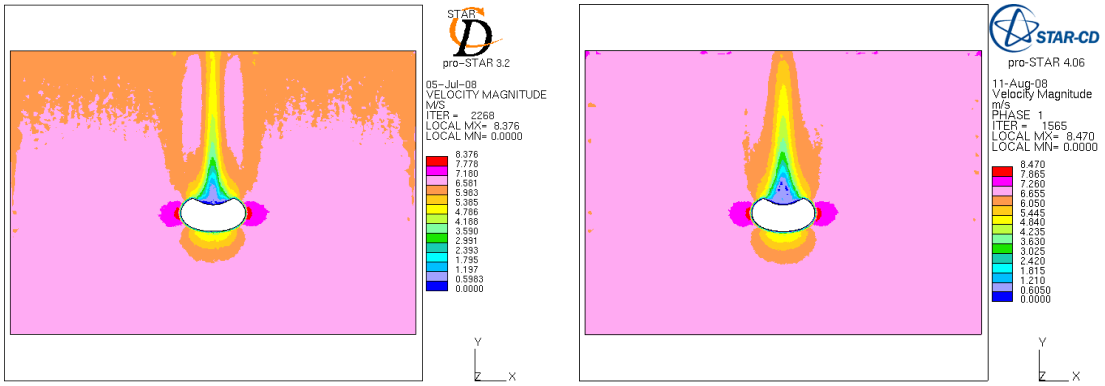

Figure H.13: Velocity magnitude at a horizontal plane 55 mm from ground level

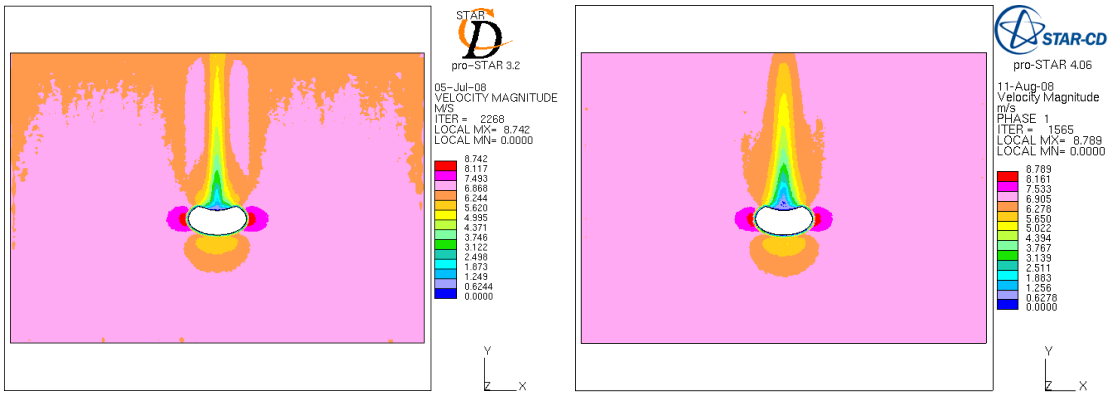

Figure H.14: Velocity magnitude at a horizontal plane 77 mm from ground level

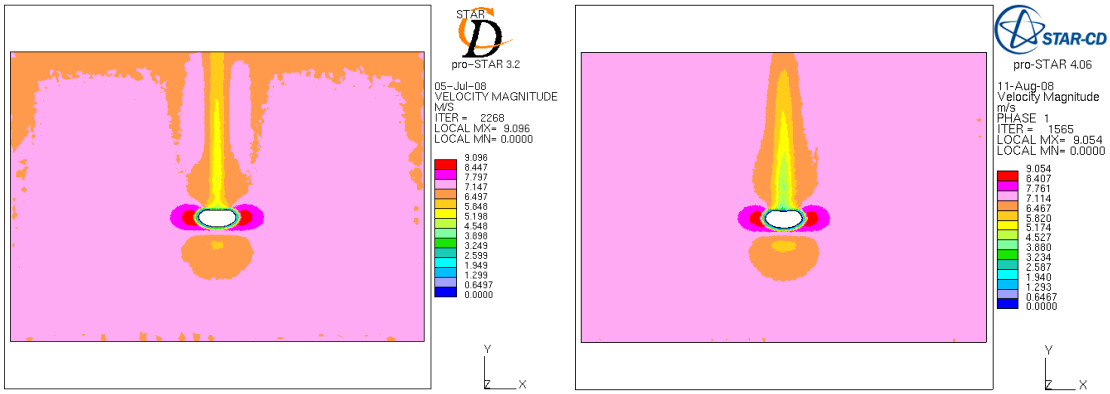

Figure H.15: Velocity magnitude at a horizontal plane 110 mm from ground level

Appendix I: Additional Figures (Chapter 4)

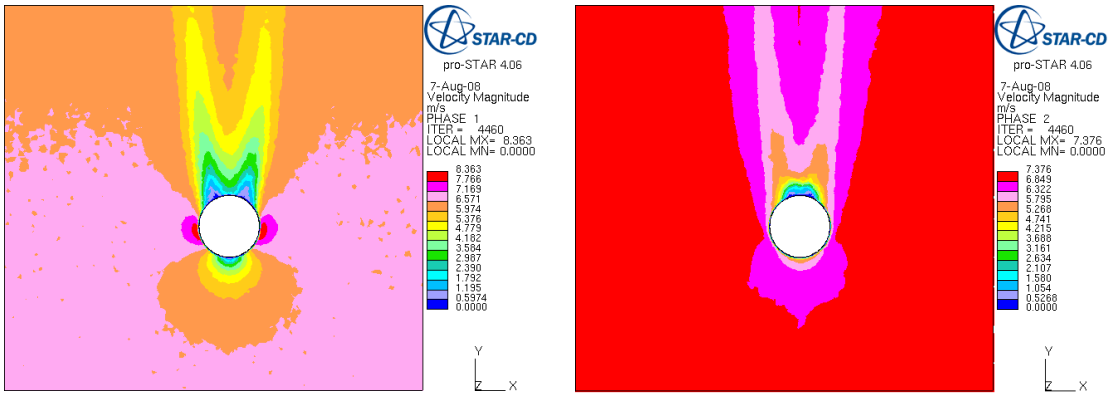

Figure I.1: Velocity magnitude at a horizontal plane 39 mm from ground level

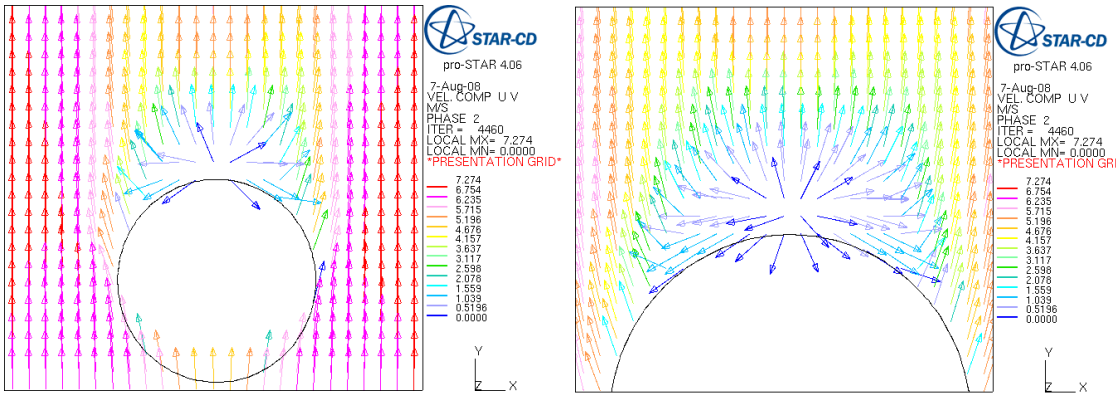

Figure I.2: Velocity vectors at a horizontal plane 6 mm from ground level

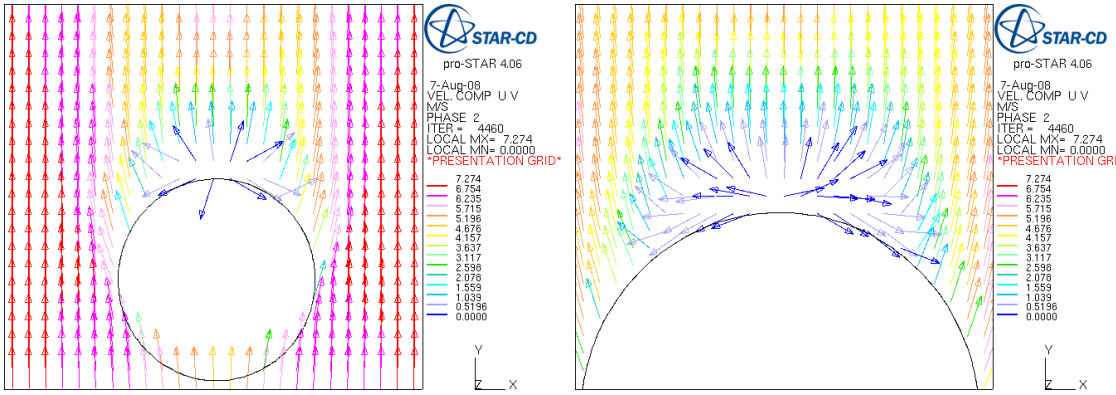

Figure I.3: Velocity vectors at a horizontal plane 16.5 mm from ground level

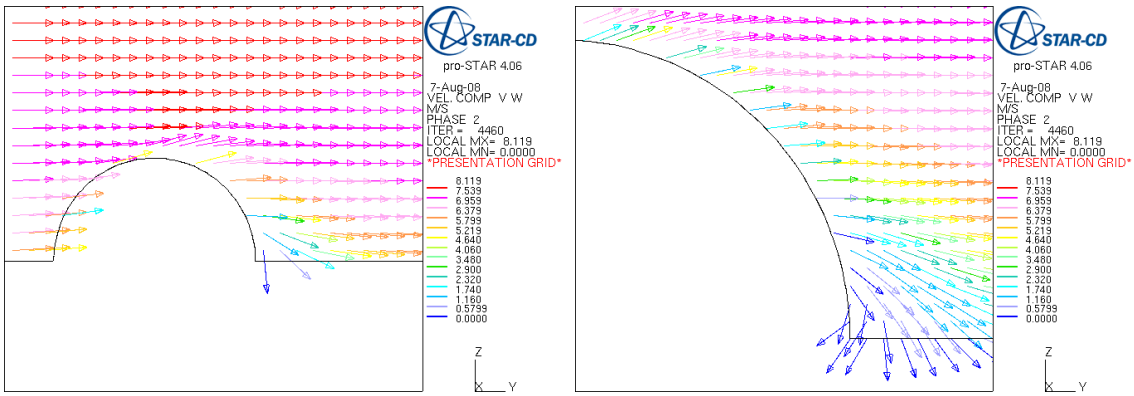

Figure I.4: Velocity vectors at the midplane of the hemisphere

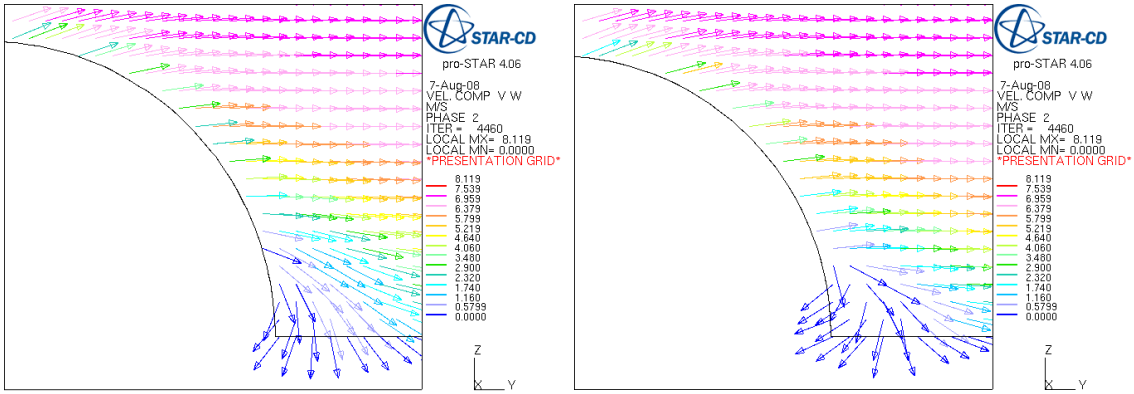

Figure I.5: Velocity vectors at vertical planes 24 mm and 52 mm from midplane

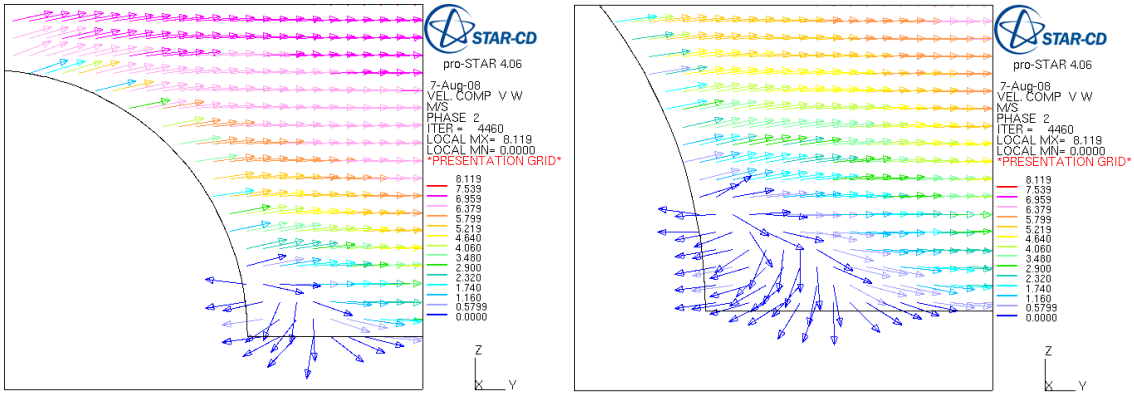

Figure I.6: Velocity vectors at a vertical plane 68 mm from midplane

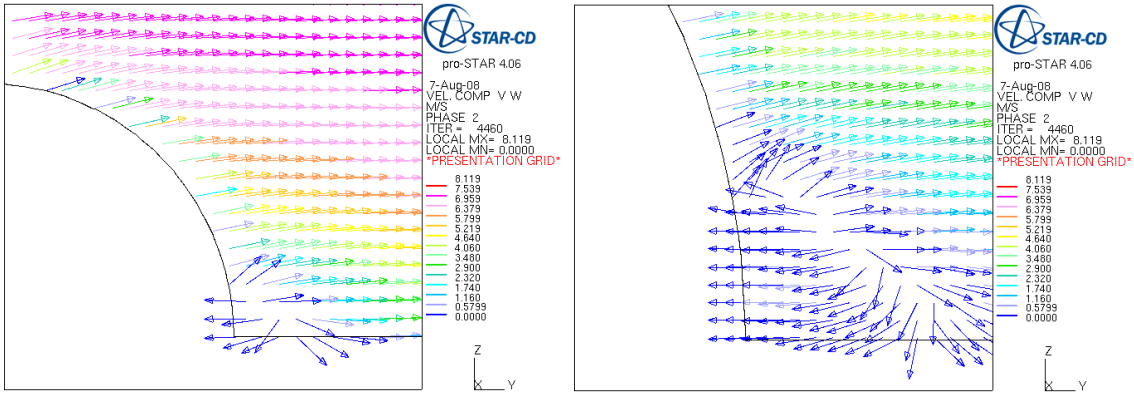

Figure I.7: Velocity vectors at a vertical plane 80 mm from midplane

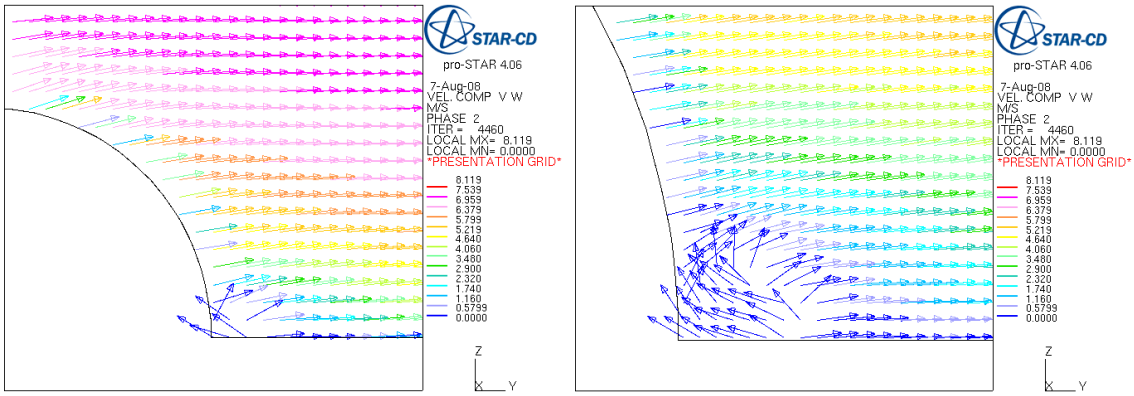

Figure I.8: Velocity vectors at a vertical plane 96 mm from midplane

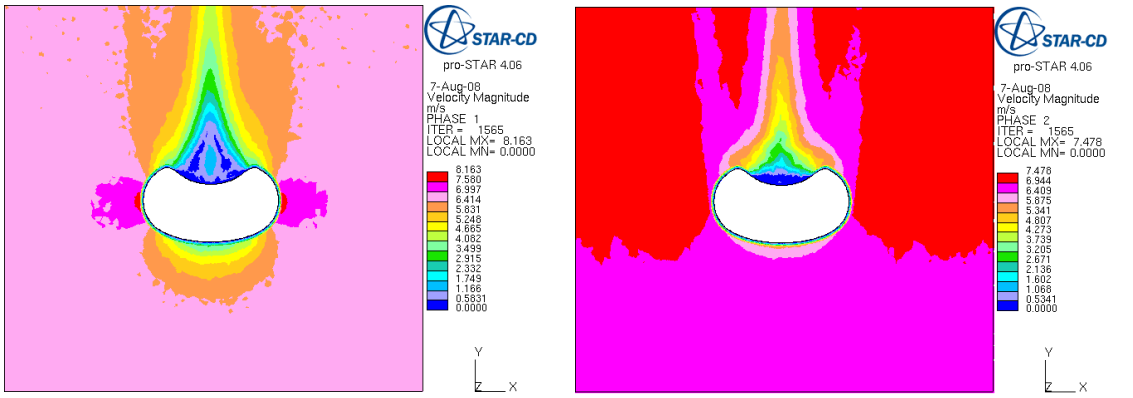

Figure I.9: Velocity magnitude at a horizontal plane 4.4 mm from ground level

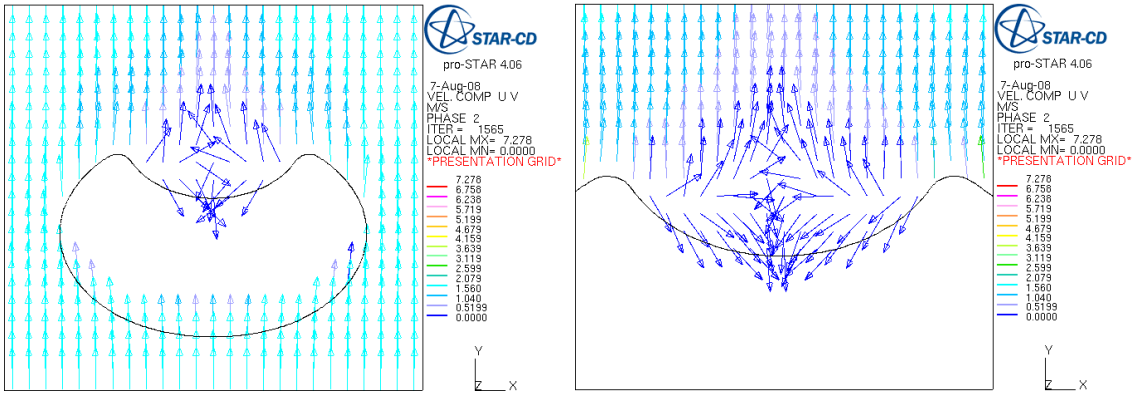

Figure I.10: Velocity vectors at a horizontal plane 4 mm from ground level

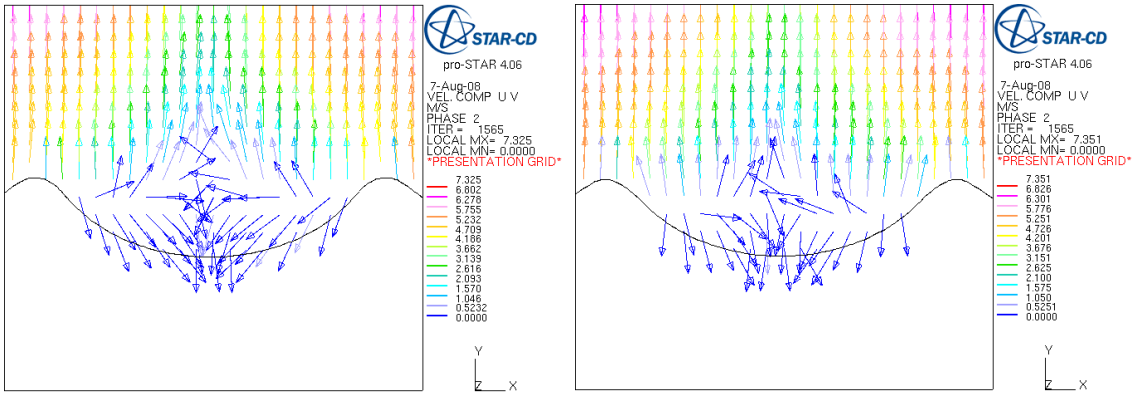

Figure I.11: Velocity vectors at planes 15 mm and 26 mm from ground level

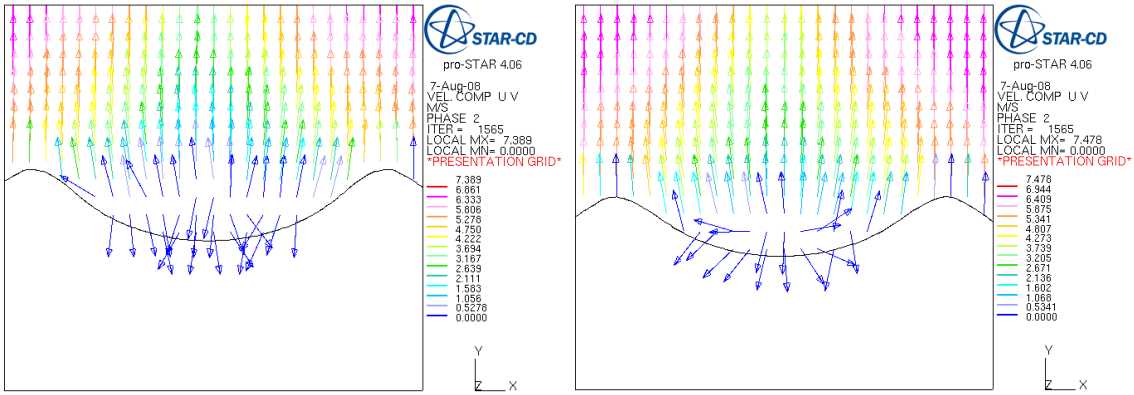

Figure I.12: Velocity vectors at planes 37 mm and 52 mm from ground level

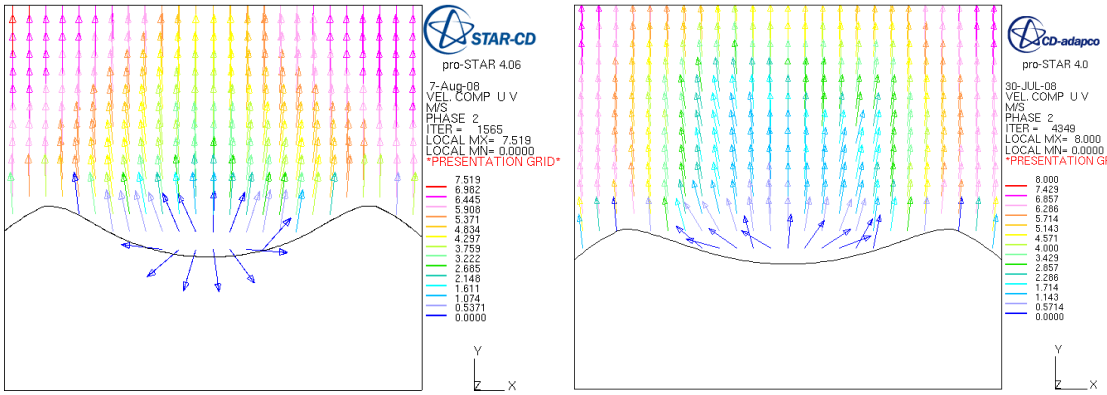

Figure I.13: Velocity vectors at planes 63 mm and 81 mm from ground level

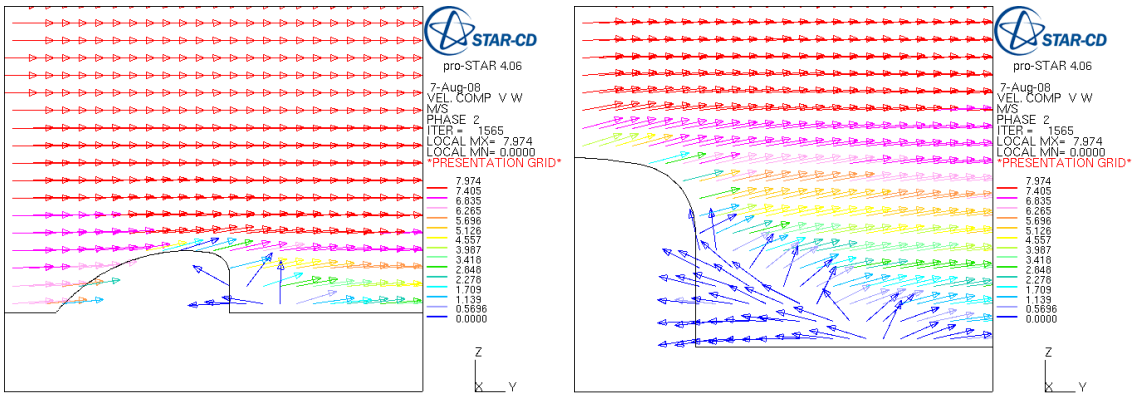

Figure I.14: Velocity vectors at the midplane of the crescent

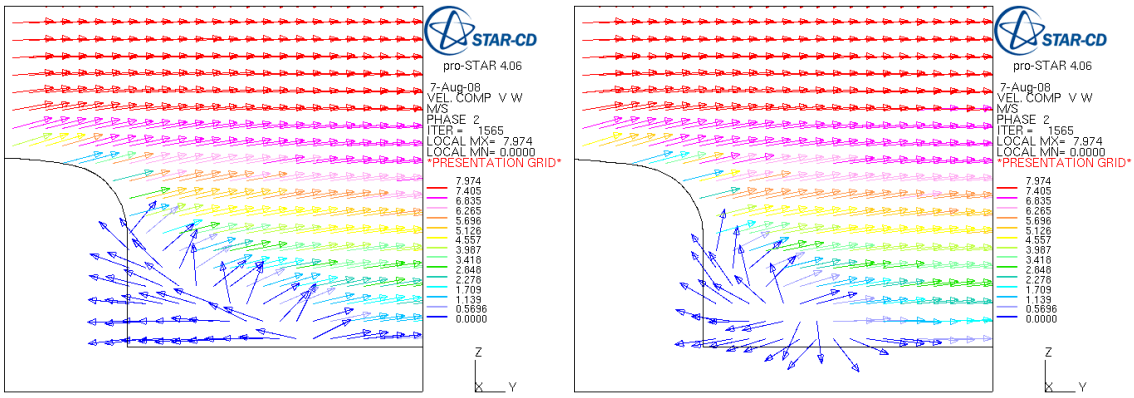

Figure I.15: Velocity vectors at vertical planes 30 mm and 65 mm from midplane

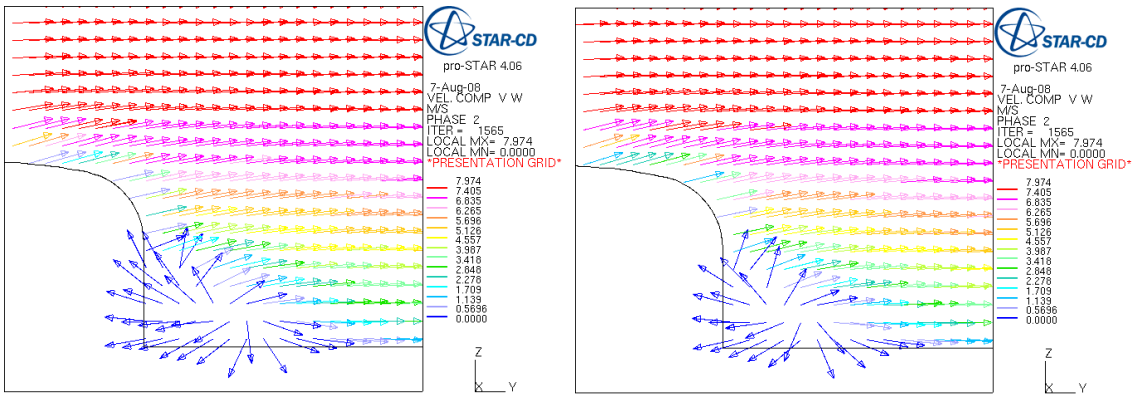

Figure I.16: Velocity vectors at vertical planes 100 mm and 120 mm from midplane

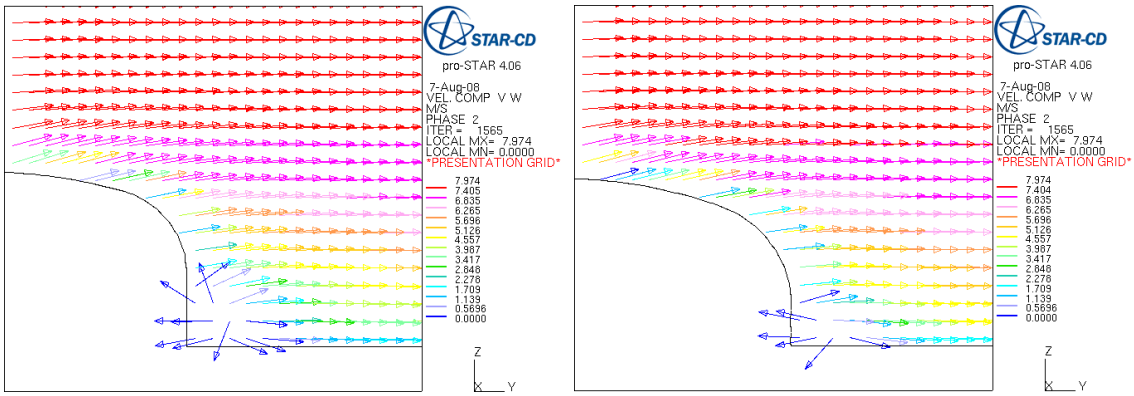

Figure I.17: Velocity vectors at vertical planes 175 mm and 210 mm from midplane